

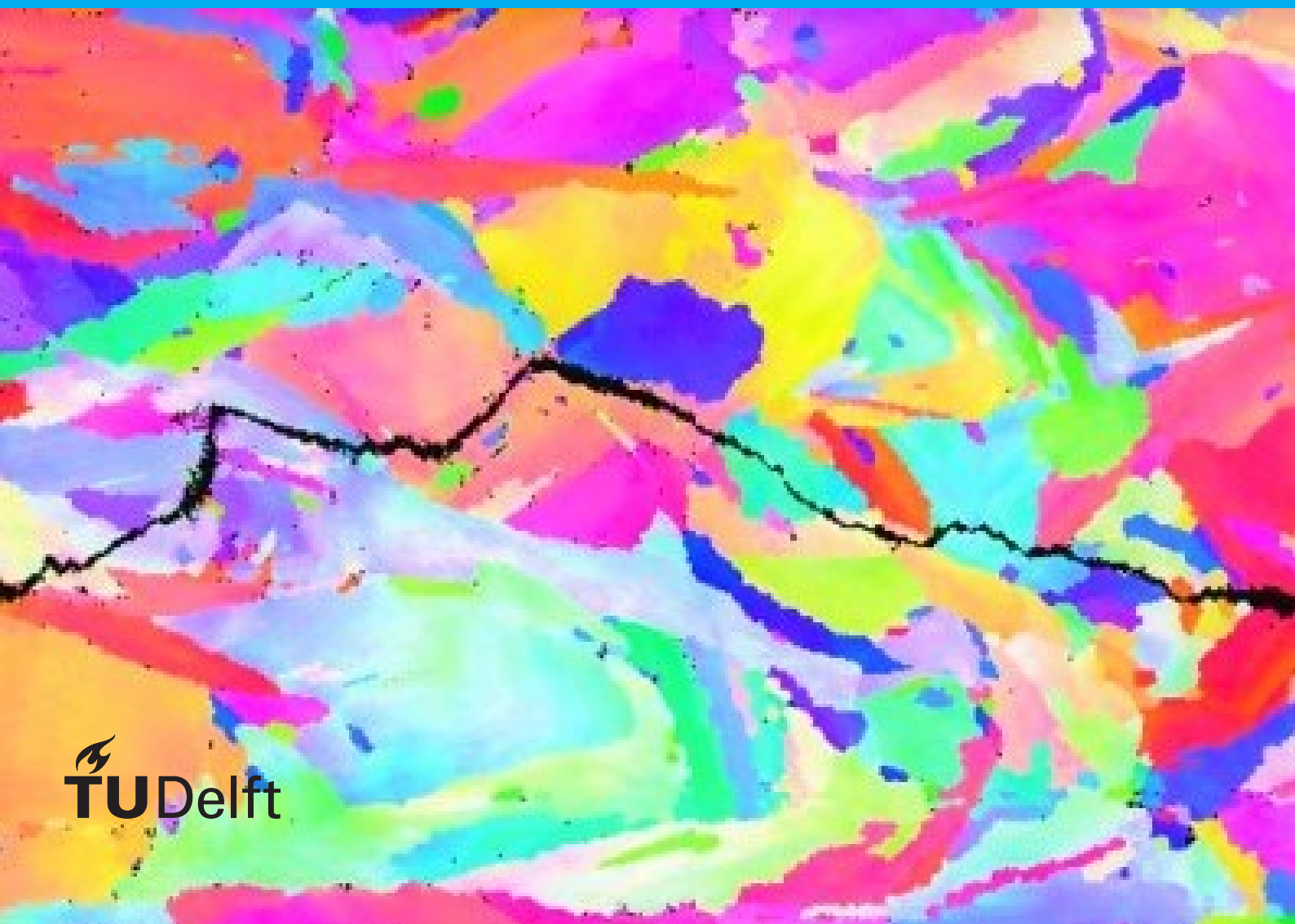
Fatigue Crack Propagation in Additively Manufactured and Functionally Graded Inconel 718

Master of Science Thesis

Kaustubh V. Deshmukh

Materials Science and Engineering

Faculty of Mechanical, Maritime and
Materials Engineering (3mE)



Fatigue Crack Propagation in Additively Manufactured and Functionally Graded Inconel 718

Master of Science Thesis

by

Kaustubh V. Deshmukh

to obtain the degree of Master of Science
at the Delft University of Technology,
to be defended publicly on Friday October 30, 2020 at 15:30.

Student number: 4809475
Project duration: November, 2019 – October, 2020
Thesis committee: Dr. V. A. Popovich, TU Delft, Supervisor
Dr. ir. A. C. Riemsdag, TU Delft
Dr. ir. M. J. M. Hermans, TU Delft
V. M. Bertolo, TU Delft, PhD candidate

An electronic version of this thesis is available at
<http://repository.tudelft.nl/>.

Abstract

Additive Manufacturing (AM), commonly known as 3-D printing, exemplifies the recently emerging processing methodologies that aim to substitute the conventional routes, such as to produce parts with complex geometries and eliminate expensive tooling. AM also allows high degree of freedom and rapid prototyping for functional part optimization. This has led to a renewed interest in the Functionally Graded Materials (FGMs). FGMs are a class of novel materials designed to have graded compositions or microstructures with tailored properties. Selective Laser Melting (SLM) is one of the most widely used AM method showing great potential to produce parts made from Inconel 718, a Nickel-based superalloy.

This study aims to investigate the microstructural gradients in Inconel 718 produced with SLM by manipulating the thermal fields acting during the production and their subsequent effect on fatigue behavior. Two different laser powers, 950 W and 250 W were used to develop coarse grained and fine grained microstructures respectively. Ungraded and graded specimens were produced to study the fatigue crack growth in individual as well as graded microstructures under cycling loading. The effect of standard post-process heat treatments on the microstructure and fatigue properties of as-printed (AP) AM Inconel 718 was also studied. The two heat treatments under discussion here are homogenisation + solution + aging (HT) and hot isostatic pressing + HT (HIPHT). Direct Current Potential Drop (DCPD) method was used to measure the fatigue crack growth rate in standard tests to identify the fatigue properties of ungraded microstructures. A new approach of using a constant ΔK procedure was employed for graded specimens to investigate the crack growth rate as a function of the crack interaction with local microstructure.

The coarse columnar grains with preferred $\langle 001 \rangle$ texture were elongated along the building direction (BD) and their axis of elongation in the specimens changed as a function of BD. Fine grains were relatively equiaxed and randomly oriented. HT had no significant effect on this observed trend while HIPHT entirely alters the printed microstructure. The grain sizes, orientation as well as heat treatments affected the fatigue behavior of individual microstructures. Fine grained microstructures showed a slower fatigue crack propagation (by $\approx 70\%$ in AP, $\approx 40\%$ in HT and $\approx 45\%$ in HIPHT) than coarse grained. Fatigue cracks propagated slower in coarse grains oriented perpendicular to the crack path in AP ($\approx 80\%$) while they were slower when oriented parallel to the crack path in HT ($\approx 75\%$) and HIPHT ($\approx 9\%$). The interfaces produced in AP and HT graded specimens were seen to introduce barriers for crack propagation and reduce local crack growth rate. The same was not observed in HIPHT due to diminished gradients, resulting from grain coarsening.

Thus, this study has successfully demonstrated the feasibility of using AM to fabricate future FGMs featuring altered fatigue response of the local microstructures.

Acknowledgements

This Masters project has been a great learning curve with tremendous experiences filled with their fair share of ups and downs. It has helped me evolve my understanding of the material science and develop an ever increasing pull towards it.

I would like to thank Dr. Vera Popovich for supervising this project and providing me the opportunity to work on such an interesting topic. Vera, I am truly humbled by the level of patience and support provided by you throughout. Your ability to maintain the intellectual and emotional acumen, the extra efforts that you put into staying connected with me while giving enough freedom, and realising the need to provide routine words of encouragement were a real source of inspiration for me. I aspire to retain and emulate your managerial skills in my professional life. It has been a great experience working with you.

A huge credit for this project also goes to Dr. Ton Riemsdag and Elise Reinton, for helping me with the equipment and sharing their vast amounts of knowledge about material testing. I thank you for providing guidance with the tests, always staying available even through your busy schedules and solving the large number of nuisances that frequently affected the tests as well as me. Your enthusiasm and happy nature always helped me keep a right mindset during these trying times. The time spent in Mechanical Behavior Lab will always be a part of the cherished memories' catalogue.

A special thanks to Saswat Sahu for laying the prerequisite foundations and helping me during the initial stages of the project. Your previous work has helped me develop a coherent story here. I would also like to thank Virginia Bertolo for freeing up her schedules several times to assist me with the EBSD. Your kind, cheerful and selfless nature will always be a fond remembrance whenever I look back at the colourful scans that you helped create. Huge thanks to Saeede Ghorbanpour for helping me with the discussion in EBSD section. All the conversations about work and life with the three of you kept me on the up at crucial stages of this project.

Thanks to Dr. Marcel Hermans for guiding me during my internship as well as showing the willingness to evaluate this work. Thanks to Sander van Asperen for helping me with the microscopy and Ruud Hendriks for doing the XRD measurements. I also thank Kees Kwakernaak for providing access to the EBSD setup.

I also appreciate the constant support and entertainment provided by all the friends back in India as well as all my fellow friends in Delft, with whom I shared this sumptuous and exhilarating two year Masters journey. The lockdown period was easier only because of these people.

Lastly, thanks to my parents and my sister for showering me with love and care through thick and thin. You are the biggest role models for me to whom I owe each and every fabric of my existence.

*Kaustubh V. Deshmukh
Delft, October 30, 2020*

Contents

List of Figures	vi
List of Tables	x
1 Introduction	1
2 Literature Review	3
2.1 Inconel 718	3
2.1.1 Microstructure	3
2.1.2 Conventional processing routes of IN718	5
2.1.3 Commercially used post-process heat treatments for IN718	6
2.2 Additive manufacturing of IN718	7
2.2.1 Introduction to additive manufacturing methodology.	7
2.2.2 Selective laser melting: an additive manufacturing method	8
2.2.3 Microstructure of IN718 processed by additive manufacturing	10
2.2.4 Effect of post-processing heat treatment on the microstructure.	11
2.2.5 Mechanical properties	12
2.3 Functionally graded materials (FGMs).	14
2.3.1 Types of FGMs	14
2.3.2 A combination of SLM and FGMs	15
2.4 Fatigue: Basics and Mechanisms.	17
2.5 Conclusions	20
2.6 Research objectives	21
3 Materials and Methods	22
3.1 Materials	22
3.1.1 SLM fabrication and post processing	22
3.1.2 Specimen geometries and categorization	23
3.1.3 Graphical summary.	25
3.2 Microstructure characterization	26
3.2.1 Microscopy	26
3.2.2 XRD analysis.	26
3.2.3 Hardness measurement.	27
3.2.4 EBSD analysis.	27
3.2.5 Fracture surface analysis	27
3.3 Fatigue testing	28
3.3.1 Test set-up	28
3.3.2 Fatigue characterization of ungraded specimens.	28
3.3.3 Fatigue characterization of graded specimens	30
3.3.4 Graphical summary.	33

4	Results and Discussion	34
4.1	Microstructural characterization	34
4.1.1	Effect of laser power and build direction on the grain structure in as-printed condition	34
4.1.2	Effect of post-process heat treatments	36
4.1.3	Micro-hardness measurements	43
4.1.4	Interfaces in graded microstructure	44
4.1.5	Summary	46
4.2	Fatigue Crack Propagation Behavior	48
4.2.1	Fatigue characterization of ungraded specimens.	48
4.2.2	Fatigue characterization of graded specimens	53
4.2.3	Summary	59
4.3	EBSD analysis of crack paths in graded specimens	60
4.3.1	As printed specimen	60
4.3.2	Heat treated specimen	64
4.3.3	Hot isostatic pressed and heat treated specimen	66
4.3.4	Summary	68
4.4	Fracture Surface Analysis	69
4.4.1	Fractured surfaces in fine grained (250 W) microstructure.	69
4.4.2	Fractured surfaces in coarse grained (950 W) microstructure	71
4.4.3	Interfaces in graded specimens.	72
4.4.4	Summary	73
5	Conclusions and Future Recommendations	74
5.1	Conclusions	74
5.2	Future Recommendations	77
6	Appendix	78
6.1	Fixture drawing and test setup	78
6.2	Matlab algorithm for processing raw MTS data	80
6.3	Residual stress measurements (x-ray diffraction)	86

List of Figures

2.1	Time-temperature-transformation diagram for IN718 alloy welds [5].	4
2.2	SEM image showing the γ' , γ'' and δ phases. (Note the depleted zones around the δ needles) [8].	5
2.3	BSE SEM images of (a) Laves phase, MC carbides and higher magnification γ' precipitate, (b) δ needles, blocky MC carbides and Laves phases [11].	6
2.4	Schematic showing SLM setup [18].	8
2.5	Schematic showing SLM setup [21].	9
2.6	(a) Optical micrograph showing the build layers (arrow indicates the building direction), (b) Schematic showing development of microstructure and its correlation with the building direction during SLM scanning [19].	10
2.7	Inverse pole figure maps of Inconel 718 processed by SLM (a) as-printed, (b) solution annealed, (c) HIPed [24].	11
2.8	Inverse pole figure maps of Inconel 718 processed by SLM (a) as-printed, (b) homogenised [5].	12
2.9	Stress-strain behavior of SLM parts under tensile loading. Here S - solution annealing, H - hot isostatic pressing, A - aging and P - arc PVD [24].	13
2.10	Types of FGMs according to (a) Composition gradient, (b) Microstructure gradient, (c) Porosity gradient [41].	15
2.11	(a) SEM micrograph and (b) EBSD map of the melt pool grain structure in CoCrFeMnNi high-entropy alloy fabricated by laser powder bed fusion [42].	16
2.12	EBSD map of IN718 functionally graded sample fabricated by selective laser melting showing the 950 W zone sandwiched between two 250 W zones [30].	16
2.13	Schematic representation of da/dN versus ΔK fatigue crack growth under constant amplitude loading. [48]	18
3.1	Schematic showing dimensions of the IN718 samples fabricated in this research. Notch specifications are seen in the inset.	23
3.2	Ungraded (UG) specimen symbols showing the correlation between the building direction (BD) & grain size/direction, and orientation of BD with respect to the crack direction (CD) per specimen.	24
3.3	Graded (G) specimen symbols showing the combination of individual laser powers used per specimen.	24
3.4	A flow chart showing a distinction between the specimens on the basis of post processing heat treatment, building direction and the different combinations of laser power used in this study.	25

3.5	A flow chart showing a distinction between the specimens on the basis of their dimensions according to the respective fabrication methodology.	25
3.6	Image showing XRD setup with the specimen arranged inside.	26
3.7	Images showing the testing setup (a) front view and (b) top view. (1) MTS machine, (2) main support, (3) specimen fixture, (4) support rollers, (5) cameras, (6) specimen, (7) current supply from DCPD, (8) DCPD probes.	29
3.8	Schematic showing the ramping up phenomenon of K_{min} in constant K_{max} tests.	30
3.9	A flow chart showing the different test methodologies adopted to characterize the fatigue crack propagation in individual microstructures of ungraded specimens and the effect of tailored microstructure of FGM on the crack propagation.	33
4.1	Optical micrographs of AP specimen for the regions produced using (a) 950 W laser power and (b) 250 W laser power.	35
4.2	Optical micrographs showing 950W as-printed (AP) specimens with (a) $BD \parallel CD$ and (b) $BD \perp CD$	35
4.3	SEM micrographs showing as-printed (AP) specimens produced using (a) 250 W laser power, (b) 950 W laser power with $BD \parallel CD$ and (c) 950 W laser power with $BD \perp CD$	36
4.4	Optical micrographs of 950W UG-HT specimens with $BD \perp CD$ at a magnification of (a) 5X and (b) 10X.	37
4.5	SEM micrographs of 950W UG-HT specimens with $BD \perp CD$ at a magnification of (a) 150X and (b) 300X.	37
4.6	Optical micrographs of 950W UG-HT specimens with $BD \parallel CD$ at a magnification of (a) 5X and (b) 10X.	38
4.7	SEM micrographs of 950W UG-HT specimens with $BD \parallel CD$ at a magnification of (a) 150X and (b) 300X.	38
4.8	Optical micrographs of 250W UG-HT specimens at a magnification of (a) 5X and (b) 10X.	39
4.9	SEM micrographs of 250W UG-HT specimens at a magnification of (a) 150X and (b) 300X.	39
4.10	Optical micrographs of (a) 250W HIPHT specimen and (a) 950W HIPHT specimen with $BD \parallel CD$	40
4.11	Optical micrographs of (a) 250W HIPHT specimen and (a) 950W HIPHT specimen with $BD \perp CD$	40
4.12	SEM micrographs showing rod like and globular precipitates in (a) UG-HT 250 W specimen and (b) UG-HT 950 W specimen with $BD \parallel CD$. Insets show respective magnified SEM micrographs, both at 2000X magnification.	40
4.13	SEM micrographs showing a cluster of rod like and globular δ precipitates in heat treated specimen (a) 950W with $BD \parallel CD$ in interdendritic spaces, (b) 250W primarily in grain boundaries but also interdendritic spaces, (c) 9000X magnification.	41

4.14 SEM micrographs showing blocky MC carbides along the grain boundaries in (a) 950W side of G-HT specimen with BD \parallel CD and (b) 950W side of G-HT specimen with BD \perp CD.	41
4.15 XRD plots for UG specimens produced using (a) 250 W laser power, and (b) 950 W laser power.	43
4.16 Interfaces in G-AP specimens with (a) BD \parallel CD and (b) BD \perp CD. . . .	44
4.17 (a), (c) SEM micrographs and (b), (d) Optical micrographs of the interface region in Graded (G) specimens.	45
4.18 Interface region in Graded (G) specimens from HIPHT conditions with (a) BD \perp CD and (b) BD \parallel CD.	46
4.19 (a), (b), (c) - da/dn v/s ΔK plots showing the fatigue curves of ungraded specimens in heat treated (HT) condition.	51
4.20 (d), (e), (f) - Summary of power law fitted curves in the Paris regions for AP, HT and HIPHT specimens respectively, showing the effect of grain size and orientation on crack growth rate in Paris region (also shown here are the HT wrought IN718 specimens for reference).	52
4.21 (a) K solutions obtained by modeling J integral, (b) Fit for the non dimensional $f(a/W)$ part of the K solutions.	54
4.22 Fatigue curve for crack growth rate da/dn under constant ΔK conditions in as-printed (AP) specimens (with the crack progression seen as a function of crack to width ratio a/W).	56
4.23 Fatigue curve for crack growth rate da/dn under constant ΔK conditions in heat treated (HT) specimens (with the crack progression seen as a function of crack to width ratio a/W).	57
4.24 Fatigue curve for crack growth rate da/dn under constant ΔK conditions in hot isostatic pressed and heat treated (HIPHT) specimens (with the crack progression seen as a function of crack to width ratio a/W).	58
4.25 Inverse pole figure applicable to the EBSD scans.	60
4.26 Optical micrograph showing the influence of melt pool boundaries and layer tracks on crack deflection in graded as-printed specimen with BD \parallel CD in the 250W and interface region. Point I is interface, points MP are melt pools.	61
4.27 SEM micrograph showing the influence of melt pool boundaries and layer tracks on crack deflection in graded as-printed specimen with BD \parallel CD in the 250W and interface region.	62
4.28 Optical micrograph showing the crack path in 950W region of as-printed graded specimen.	62
4.29 EBSD inverse pole figure (IPF) map of the interface region in G-AP specimens with (a) BD \perp CD and (b) BD \parallel CD. Points I are interfaces, MP are melt pools, 45° is deflection by $\langle 001 \rangle$ grains and D is a rare deflection described in the text.	63
4.30 Optical micrograph showing the influence of layer tracks and mishmash dendritic pattern at the interface on crack deflection in graded as-printed specimen with BD \perp CD.	64

4.31 EBSD inverse pole figure (IPF) map of the interface region in G-HT specimens with (a) $BD \perp CD$ and (b) $BD \parallel CD$. Points I are interfaces and 2 nd is a secondary crack at surface.	65
4.32 EBSD inverse pole figure (IPF) map of the interface region in G-HIPHT specimens with (a) $BD \perp CD$ and (b) $BD \parallel CD$. Points GB are the grain boundaries and twin are the twin boundaries.	67
4.33 SEM micrographs showing fractured surface in interface regions for specimen conditions (a),(b) - <i>AP</i> ; (c),(d) - <i>HT</i> ; (e),(f) - <i>HIPHT</i>	69
4.34 SEM micrographs showing fractured surface in 250W region of G-AP specimens with (a) stair like features, and (b) facets revealing two different grains with features aligned in two distinct directions.	70
4.35 SEM micrographs showing fractured surface in 250W region of G-HT specimens with (a) secondary micro-cracks, and (b) sharp stair like features - lamellae.	71
4.36 SEM micrographs showing fractured surface in 250W region of G-HIPHT specimens with (a) flat faceted surfaces with other features similar to those in AP and HT, and (b) twin boundaries on the fracture surface.	71
4.37 SEM micrographs showing fractured surface in 950W region of G-HIPHT specimens representative of both BD as well as all the post-processing conditions.	72
4.38 SEM micrographs showing fracture surfaces revealing the particulates in interface regions of AP and HT specimens with $BD \perp CD$	72
6.1 Drawing of the specimen fixture used to clamp the specimen on to the main support.	78
6.2 Flowchart showing the prerequisite steps required to prepare the specimen before testing.	79
6.3 Flowchart showing the different components employed in the test setup.	79

List of Tables

2.1	Chemical composition of commercially produced IN718 [1].	3
2.2	Standard heat treatments applicable to IN718 according to SAE (Society of Automotive Engineers) [1, 12, 13]	7
2.3	Room temperature tensile properties of IN718 processed via SLM [29].	13
2.4	Room temperature directional tensile properties of as-printed and post-processed IN718 processed via SLM [34].	13
2.5	Room temperature tensile properties of HIPed IN718 processed via SLM [34]. (PBF - powder bed fusion and BPD - blown powder deposition)	14
3.1	SLM fabrication process parameters of the specimens	22
3.2	Standard heat treatments applicable to IN718 according to SAE (Society of Automotive Engineers) [1, 12, 13].	23
3.3	Summary of values for Young's Modulus (E) obtained from Displacement Method through the three point bending tests	32
4.1	Summary of micro-hardness measurements of ungraded specimens. . .	44
4.2	Summary of constant K_{max} tests with the corresponding threshold values.	49
4.3	Combined summary of Paris fit data showing the Paris constants and exponents.	53
4.4	Summary of da/dn values at $\Delta K = 16.5 \text{ MPa}\cdot\sqrt{m}$ and $22.5 \text{ MPa}\cdot\sqrt{m}$ obtained from fitting curves in Paris region.	53
6.1	Residual stress measurements at on the XY planes of the ungraded specimens.	86
6.2	Residual stress measurements on the XY planes of graded specimens.	86

Introduction

Nickel has seen a steep increase in its usage as an alloying element in the last century. It has shown commendable capabilities to improve the corrosion resistance and high temperature strength in iron-nickel alloys or the Nickel based superalloys. One of these superalloys - Inconel 718 (IN718) has been principally used in critical high temperature applications such as in aircraft components, jet turbine blades, pressure vessels, etc. With a constant focus on extending the applicability of such novel materials, Inconel 718 and other similar super-alloys have also been formerly used in lesser critical applications, such as in land based steam and gas turbine blades as well as in storage containers in oil and gas industries [1].

With the increase in industrialisation, there has been a need to integrate highly engineered components with the ability to undergo unreal and extremely harsh conditions during service. Researchers have come up with novel methods and materials to satiate this need. A crucial step in achieving an effective applicability of a new methodology or technique involves the study of its effect on the basic material properties through the knowledge of changes in the microstructure. As trivial as it may seem, these steps pave the way for further improvements in a material technology. Additive manufacturing (AM) is one such technological response in a bid to transition from the conventional techniques such as casting and forming, towards newer processing technologies. The need to incorporate this transition stems from the desire to reduce costs of production, introduce design freedom and improve its effectiveness, as also making these technologies suitable under the umbrella of sustainability. In a quest to rope in the materials made from such novel processing methodologies into real world applications, the first and foremost step involved is to test their applicability [2]. With fatigue being one of the principle reason for failure in engineering structures, the primary focus of this thesis is to study the role of microstructure in Inconel 718 processed via AM on its resistance to fatigue.

The AM method used to process Inconel 718 is the Selective Laser Melting (SLM), which is considered as one of the most promising powder bed fusion based AM process. Process induced anomalies such as porosity, residual stresses, micro-segregation and brittle inter-metallic phases are almost always intertwined with SLM. SLM also involves high thermal gradients making the features like texture and the inherent grain structure highly relevant for all discussions involving investigation of the influence of processing on the fatigue properties. Another topic

of interest are the standard post-processing heat treatments applicable to conventionally produced wrought and cast Inconel 718. These heat treatments are already proven to be beneficial, especially in strengthening the components produced from such processing methods. However, there are only a few detailed study previously performed to evaluate their effect on the AM microstructure and subsequently the fatigue properties. Some of these treatments can also help in addressing the anomalies observed in SLM processing.

This thesis will also investigate the tailored microstructures fabricated from the same process of SLM. Such materials with tailored microstructures were labeled as Functionally Graded Materials (FGMs), which are the outcome of previous studies performed at Delft University of Technology. These FGMs can be manufactured by tweaking the SLM process parameters such as the laser power, building directions, etc. Functional grading is a lucrative domain as it produces a smoother transition across the interface unlike the sharp interchanges in a composite layer. This helps in processing a single component with two or more zones that may have an individual preference for a certain mechanical property according to the component design or a variation in the same mechanical property. The latter will then make the concept of interfaces in these FGMs even more important. The two zones under consideration for this study are the fine grain microstructure and the coarse grain microstructure. A sound understanding of fatigue crack propagation behavior in these zones as well as the interfaces is therefore important for future research and applications of such FGMs.

The subsequent contents of this thesis are divided into 6 chapters. Chapter 2 - Literature Review deals with explaining all the theories and details about the topic as well as specifies the research objectives of this study. Chapter 3 - Materials and Methods draws attention towards the specimen processing, testing methodology and experimental techniques used in realising the research objectives. Chapter 4 - Results and Discussion is subdivided into 4 sections - Microstructural characterization, Fatigue Behavior, EBSD analysis and Fracture surface analysis. It showcases all the results obtained from the experimental techniques employed while providing an explanation about the observed results. Through these explanations, it is attempted to correlate the processing - microstructure - properties in their respective summary sections. Chapter 5 - Conclusions tries to answer the outcome of research objectives and provides the future recommendations for further work on the current research. The final chapter contains appendices with all the supplementary information.

Literature Review

2.1. Inconel 718

Inconel 718 (IN718) is a nickel-based super-alloy. The term super-alloy is derived from its exceptional high temperature properties and tolerance to damage by fatigue. Inconel 718 is a precipitation hardened iron-nickel alloy with high strength to weight ratio and superior creep properties. The alloying contents of IN718 are designed so as also to render it with excellent corrosion resistance and good weldability. A typical chemical composition with the important alloying elements for IN718 is given in Table 2.1. All the elements listed have a specific positive role however they are also associated with some detrimental roles on the same page. This will be dealt with in section 2.1.1. This makes it critical to incorporate a processing route which complements the tailoring of these alloying elements to be present in a specific form to bring forth the properties that IN718 has been designed for [1, 3].

Table 2.1: Chemical composition of commercially produced IN718 [1].

Alloying Element	Ni	Cr	Nb	Mo	Ti	Co	Al	Fe
Wt. %	50-55	17-21	4.8-5.5	2.8-3	0.65-1.15	1	0.2-0.8	balance

2.1.1. Microstructure

The microstructure of IN718 constitutes of six main constituents. Their presence and formation is mainly dependant on the processing route and the type of post processing heat treatment given to the IN718 [4]. This will be discussed in detail later. The majority matrix phase formed is the γ phase, a solid solution of Ni, Cr, Fe and Mo. The ageing treatment results in the formation of γ' and γ'' phases. These are the metastable strengthening phases that form the basis of the precipitation hardening in most Ni based super-alloys. Figure 2.1 gives an idea about the phases present in IN718 after rapid solidification and their respective solvus temperatures.

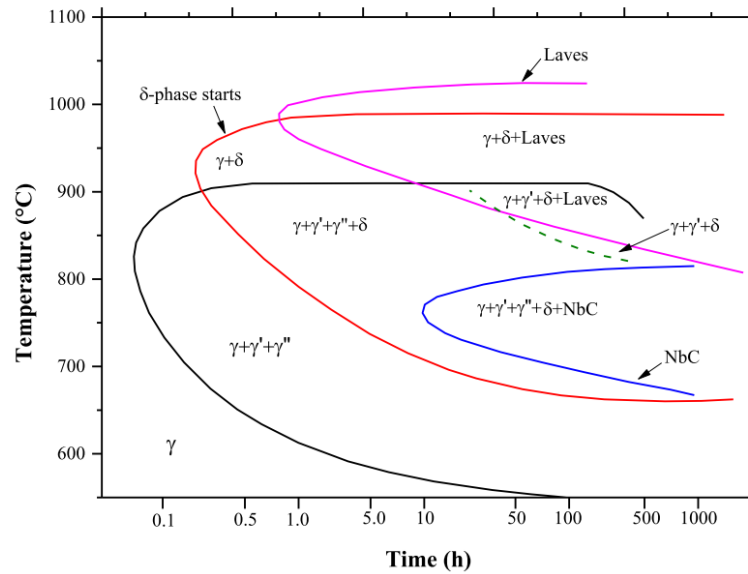


Figure 2.1: Time-temperature-transformation diagram for IN718 alloy welds [5].

γ phase: γ phase forms the matrix in the microstructure of IN718. It has a fcc based A1 lattice structure. γ phase is essentially a solid solution of Ni, Cr and Fe. Minor proportions of Nb, Mo, Ti and Al are also present in the solid solution constituting the matrix phase [3, 6].

γ' phase: γ' phase has an ordered fcc based $L1_2$ lattice structure. The stoichiometric composition of the intermetallic γ' phase is $(Ni_3(Al, Ti, Nb))$. This γ' phase is coherent with the underlying γ matrix and has a globular morphology. This is helpful in improving the strength of the matrix as a result of antiphase boundary hardening [7]. Thus, γ' is a beneficial phase in IN718 and it's presence is to be promoted during the processing as well as post-processing. These phases can be seen in Figure 2.2.

γ'' phase: Similar to the γ' phase, γ'' phase is a metastable phase that enhances the strength in IN718. The main principle behind this is the precipitation hardening as the small size (10-50 nm) of these precipitates warrants the shearing mechanism during dislocation motion. The γ'' phase has a stoichiometric composition as Ni_3Nb with small proportions of Al and Ti, and has a DO_{22} fcc lattice structure. It has disk-shaped/ellipsoidal morphology as seen in Figure 2.2 [7].

δ phase: δ phase is the stable equilibrium phase precipitated from the γ'' phase after prolonged thermal exposure. It has a DO_a orthorhombic lattice structure. This phase is precipitated in needle-like or globular morphology as seen in Figure 2.2. As this phase has a direct correlation with γ'' phase, it is also based on a stoichiometric composition of Ni_3Nb and is also sometimes rich in Ti. The advantages and disadvantages of having δ precipitates are shown to be based on their final composition in the microstructure. Since these are produced at the expense of γ'' , a strengthening phase, their presence beyond 2% may be detrimental and cause embrittlement [8].

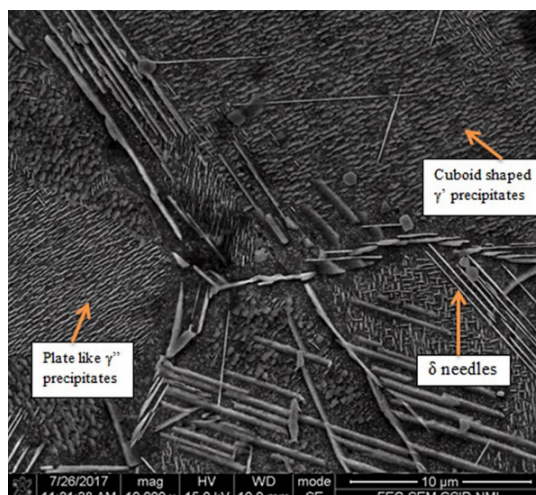


Figure 2.2: SEM image showing the γ' , γ'' and δ phases. (Note the depleted zones around the δ needles) [8].

Laves phase: Laves phases are the coarse inter-metallic precipitates with cubical morphology, a C_{14} hexagonal lattice structure and a chemical formula as $(Fe, Ni, Cr)_2(Nb, Ti)$. These can be seen in Figure 2.3. Presence of Laves phase is detrimental in two main ways. These phases are rich in Nb and Mo leading to a depletion of elements responsible for the formation of γ' and γ'' strengthening phases. Laves phases are also grain boundary precipitates and aid to a crack propagation through the grain boundaries which has been found to be detrimental for mechanical properties of IN718. Laves phases are the earliest to precipitate during the solidification process or after annealing above 1040°C , because of which they are also found in interdendritic spaces [9]. The presence of Laves phase can be overcome with a homogenization heat treatment [10].

MC carbides: Another type of coarse blocky precipitates are the MC type of carbides. Nb and Ti usually produce these carbides. They are formed alongside the Laves phase and are detrimental for the same reasons as the Laves phases [10]. These phases can be seen in Figure 2.3.

2.1.2. Conventional processing routes of IN718

Inconel 718 has been formerly produced in three forms - wrought, cast and powder metallurgy. To fabricate any of the above mentioned IN718, processing usually includes producing large ingots as the preliminary step. These ingots are subsequently remelted by vacuum induction melting and followed by (1) hot working to roll, forge or extrude the final wrought product, (2) investment casting and (3) IN718 powder production to consolidate near-net-shape products [12, 13]. Wrought processing involving hot working induces a homogeneous microstructure with fine grains. Due to the annealing effect, twins and δ phases are also obtained. Wrought forming is always followed by post-process heat treatments. Cast IN718 has its application in conditions demanding coarser grains favouring high temperature strength. Cast products are often accompanied by porosity, interdendritic

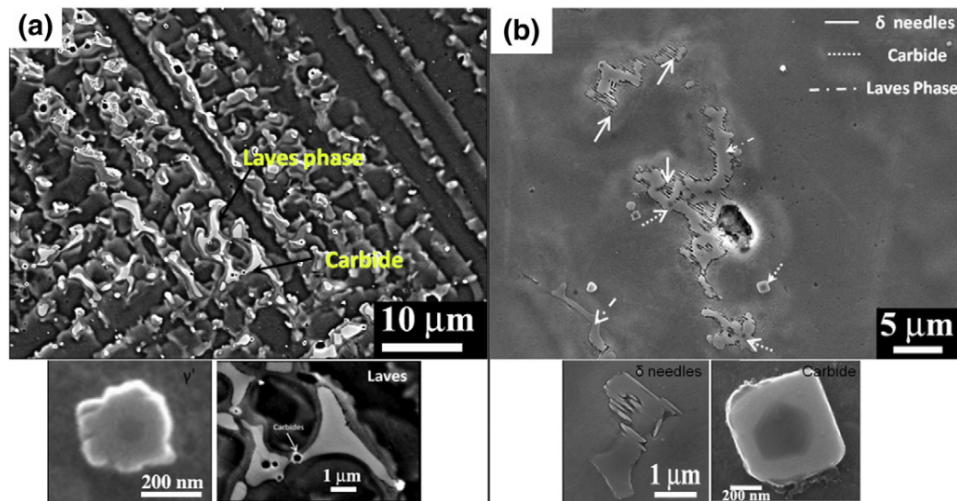


Figure 2.3: BSE SEM images of (a) Laves phase, MC carbides and higher magnification γ' precipitate, (b) δ needles, blocky MC carbides and Laves phases [11].

segregation and Laves phases. Powder metallurgy produced IN718 has near microstructure resemblance to wrought IN718 due to the hot isostatic pressing involved in consolidating the IN718 powder. However, this route is beneficial in producing near-net-shape complex components to reduce the dependability on hot working [3].

2.1.3. Commercially used post-process heat treatments for IN718

There are several possibilities for which heat treatments can be used as a post processing step. The commonly used heat treatments for IN718 include stress relief, hot isostatic pressing (HIP), solution and ageing treatments. The standard heat treatment procedures for IN718 are shown in Table 3.2. The stress relief treatments are purposely used for minimizing thermal strains and distortions, and are relevant for alloys manufactured by all types processing routes. HIP is beneficial in reducing the proportion and size of enclosed porosities, in turn leading to the densification of the alloy. HIP is highly relevant in the context of AM for the reduction of process induced pore density, the occurrence of which is explained briefly later. The aging heat treatments are essential in tweaking the size, proportion and morphology of the strengthening γ'/γ'' and δ precipitates formed in IN718. The aging heat treatments are almost exclusively preceded by a homogenisation heat treatment which, as the name suggests, homogenize the grain structure, remove any micro-segregation induced during processing as well as dissolve the brittle Laves phases [1, 11, 14, 15]. Naturally, each heat treatment will have a distinct effect on the underlying microstructure in IN718 and subsequently the properties of the heat treated components. Hence, the principle motive in using any type of treatment is to improve the favourable properties of the processed alloy [15].

Table 2.2: Standard heat treatments applicable to IN718 according to SAE (Society of Automotive Engineers) [1, 12, 13]

Standard	Heat treatment	Temperature	Hold time	Cooling
AMS 5663	Solution	980 °C	1 h	Air cooling
	Aging	720 °C	8 h	Furnace cooling to 620 °C at 55 °C/h
		620 °C	8 h	Air cooling
AMS 5383	Homogenisation	1080 °C	1.5 h	Air cooling
	Solution	980 °C	1 h	Air cooling
	Aging	720 °C	8 h	Furnace cooling to 620 °C at 55 °C
		620 °C	8 h	Air cooling
AMS 5664E	Hot isostatic pressing	1180 °C at 150MPa pressure	3 h	Furnace cooling
	Homogenisation	1065 °C	1 h	Air cooling
		760 °C	10 h	Furnace cooling to 650 °C at 55 °C
	Aging	650 °C	8 h	Air cooling

2.2. Additive manufacturing of IN718

2.2.1. Introduction to additive manufacturing methodology

As such, the novel technique of additive manufacturing was coined in the late 20th century, but the possibility of using this as a feasible processing route wasn't looked into by the researchers and the industries until the 1980s. Additive manufacturing is able to manufacture complex shapes and geometries using the CAD files and automated systems integrated to generate components without using any kind of molds or casts. This allows an efficient build up of the desired components without substantial wastage compared to conventional processing routes, reducing the hustle in manufacturing complex shapes and geometries of components. Further compensated by the reduced requirement of incorporating the post-processing steps such as machining, helps save time as well as financial investments [16].

Additive manufacturing is categorised either by the type of feedstock used – powder or wire, or the type of energy source used. The most widely used metal additive manufacturing (MAM) is the powder bed fusion category. Selective laser melting (SLM), electron beam melting (EBM), direct metal laser sintering (DMLS) etc. are the commonly used powder bed based MAM techniques. The powder bed fusion category relies on a thermal source to build components layer by layer over the powder bed. Typically, a laser, an electron beam or a plasma arc is used as the source. SLM has seen a tremendous growth in its usage for MAM [1]. As this research primarily focuses on SLM, it will be the only method to be discussed in detail.

Previous researches have shown that the as deposited AM alloys possess fracture toughness and fatigue crack propagation properties in the region of the cast and wrought alloys. But the characteristics have been argued to be widely different for AM alloys because of the presence of porosity, lack of fusion, and other additional defects [17]. There is not a general consensus about this behaviour, hence leading to a plethora of possibilities in this topic.

2.2.2. Selective laser melting: an additive manufacturing method

Selective Laser Melting (SLM), Direct Metal Laser Sintering (DMLS) and Selective Laser Sintering (SLS) fall under the same umbrella of additive manufacturing which is the laser based powder-bed fusion (L-PBF). Typically, for all these processes, a laser beam is used to either partially (sinter) or fully melt the pre-produced powder. In SLM, the powder is simply fully melted as the name suggests. A 3D model is designed and fed into the AM machine and a software therein breaks the model down into layers/slices of equal thickness. Using this 3D model, the machine maps and scans the specific locations on the layer of powder bed spread across the building platform. The component keeps building up layer by layer as the building platform is lowered and a new layer of powder is spread on top. Subsequently, scanning the new layer of powder each time in a specific location also fuses it to the previous layer. After the complete component is scanned, the loosely aggregated powder bed is removed revealing the processed component. This component is then either removed from the building platform or passed on directly for any stress relief heat treatment if required [3, 13]. The whole process is carried out in an inert gas atmosphere to avoid any contamination or oxidation [1]. A large number of recent research has also been devoted on reusing the unscanned and unmelted powder. Figure 2.4 shows a schematic with the process setup of SLM.

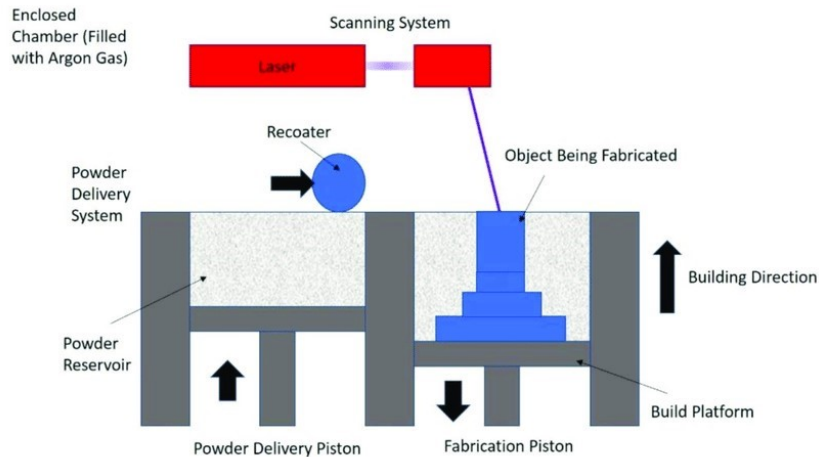


Figure 2.4: Schematic showing SLM setup [18].

Process of selective laser melting

A distinct set of parameters outlined in this section govern the cooling variations during SLM processing which in turn affect the final solidification microstructure which is then inter-twinned with the mechanical properties of the components fabricated [19]. The high cooling rates leading to a rapid solidification make the SLM process partly comparable to a continuous welding process. And the fact that IN718 shows a good weldability is why it is suitable for SLM [20].

The most essential parameters affecting the final product can be distinguished on the basis of laser characteristics, scan type, material properties, temperature or the environment. However the most commonly adjustable process parameters

associated with SLM are: laser power, scanning speed, hatch spacing and layer thickness (shown in Figure 2.5) [21].

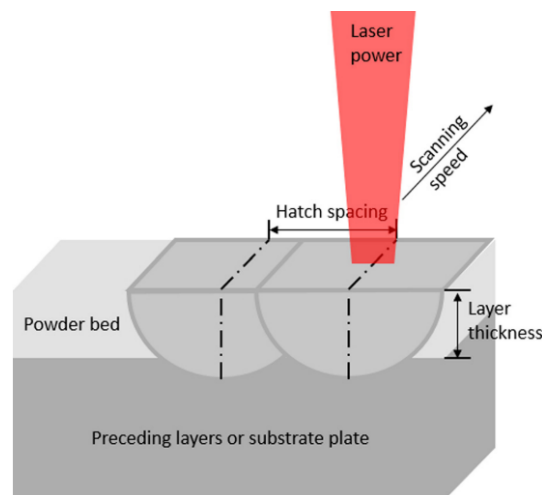


Figure 2.5: Schematic showing SLM setup [21].

Defects associated with the process of selective laser melting

The most common defects associated with the SLM fabricated components are the residual stresses, porosity and cracking.

Residual stresses are introduced during SLM fabrication because of the highly transient temperature profile in and around the laser spot and the heating zone. Residual stresses are to a certain degree, a cause of concern since they may affect the geometrical accuracy because of a resulting distortion or non-uniform deformation during solidification. Additionally, the final residual stresses after solidification can also significantly alter the mechanical properties of the components. A simple model to explain the residual stresses arising during SLM proposed that there are tensile stresses present towards the upper portion of the scanned layer while compressive stresses towards lower portion. Preheating the building platform and using an optimal scanning strategies have shown to significantly reduce the residual stresses [3].

Pores observed in the as-fabricated SLM components are of two types. One type are the spherical pores formed as a consequence of the inert environment interacting with the melt pools or gas entrapment into the melt pools. This type of pores are less deleterious on the mechanical properties of the components and come into consideration only at high temperatures wherein the entrapped gases may expand increasing the internal stress. However another type of irregular pores are also formed during SLM. Their irregular shape can give rise to undesirable stress concentrations under service conditions leading to failure. Such irregular pores are a direct consequence of the lack of fusion. Unmelted powder particles appear between the deposited melt pool layers. These particles remain unmelted due to insufficient heat: high scanning speed, large hatch spacing, high layer thickness and a low laser power [1, 3, 22].

2.2.3. Microstructure of IN718 processed by additive manufacturing

AM parts are inherently classified with an an-isotropic microstructure due to the uneven thermal profile because of the directional heat transfer during processing. In SLM, it is even more pronounced due to higher cooling rates as a result of localised melting of powder. This leads to growth of fine γ dendrites along the building direction as the heat is dissipated through the relatively cooler building platform. These dendrites can extend well into several layers depending on the process parameters. With the micro-dendrites growing along the building direction, microstructure of SLM IN718 is further characterised by a typical epitaxial growth of the columnar grains which are also almost parallel to the building direction. The fcc lattices have an inherent characteristic of solidifying along the $\langle 001 \rangle$ crystallographic direction, SLM IN718 has a prominent $\langle 001 \rangle$ texture relative to the building direction (seen in Figure 2.6.(b)) [19]. Globally, the melt pools have a Gaussian morphology with a horizontal as well as vertical overlap to bond the melt pools together. This Gaussian appearance of the melt pools can be seen in Figure 2.6.(a). The resulting overlap may change the solidification structure per melt pool from the one mentioned above and is almost always dependant on the local thermal profile. The columnar grains can therefore stretch across several melt pools due to remelting if the heat flow is sufficiently high along the building direction [5].

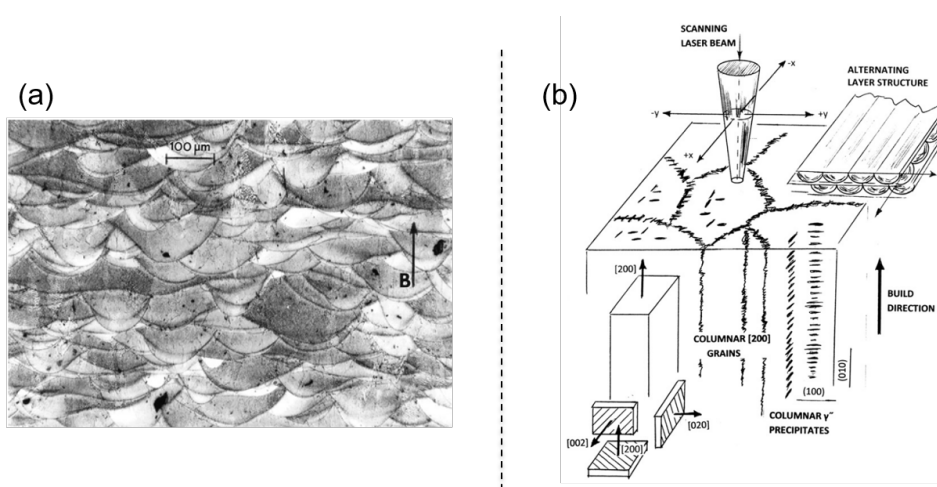


Figure 2.6: (a) Optical micrograph showing the build layers (arrow indicates the building direction), (b) Schematic showing development of microstructure and its correlation with the building direction during SLM scanning [19].

The steep thermal gradients and cooling rates involved in the processing of IN718 by SLM does not allow the precipitation of γ' and γ'' phases in the as-processed condition. These conditions coupled with the temperatures reached during SLM are also unfavourable for the decomposition γ'' phase into δ phase. The most prominent phases favoured to form in the as-processed IN718 are the γ phases and the Laves phases. Laves phases have been observed to segregate between the γ dendrites during SLM [23]. Hence, to obtain enhanced proportion of the dispersed γ' and γ'' strengthening precipitates, post processing heat treatments

become increasingly necessary.

2.2.4. Effect of post-processing heat treatment on the microstructure

The main heat treatments discussed in the context of IN718 are hot isostatic pressing (HIP), solution annealing, homogenisation and lastly aging. The temperatures and their brief effects were discussed in section 2.1.3. This section will try to decipher the effect of these post-process heat treatments on the microstructure of as-printed IN718 using AM methods.

It has been already discussed that the SLM process has a characteristic effect on the grain structure in IN718. The same can be seen visually from the findings of Aydinöz et. al. [24]. Figure 2.7 (a) shows the inverse pole figure (IPF) map of IN718 processed via SLM. Grain elongation with a strong $\langle 001 \rangle$ texture along the building direction is seemingly apparent in this map. Solution annealing heat treatment is expected to redistribute the precipitates formed during processing at the grain boundaries. Other than that it does not have any significant effect on the printed microstructure, which is evident from Figure 2.7 (b). Seen from this map is a clear indication of texture and grain structure retention. Tucho et. al. [25] and Brenne et. al. [26] reported the same effect of solution annealing. On the other hand HIPing step involves high pressures of upto 1000 bar and high temperatures of around 1150°C. The former promotes recrystallization and twin formation while the latter erases the sub grain structure and leads to equiaxial granular microstructure evolution. This completely alters the printed microstructure. The same can be seen from Figure 2.7 (c). It is also reported that HIPing leads to precipitation of MC carbides at the grain boundaries. In addition, the subsequent homogenisation and aging treatments that accompany HIPing, occasionally lead to further coarsening of these intergranular MC carbide precipitates. Other studies on the HIPed microstructure reported similar observations [5, 19, 27].

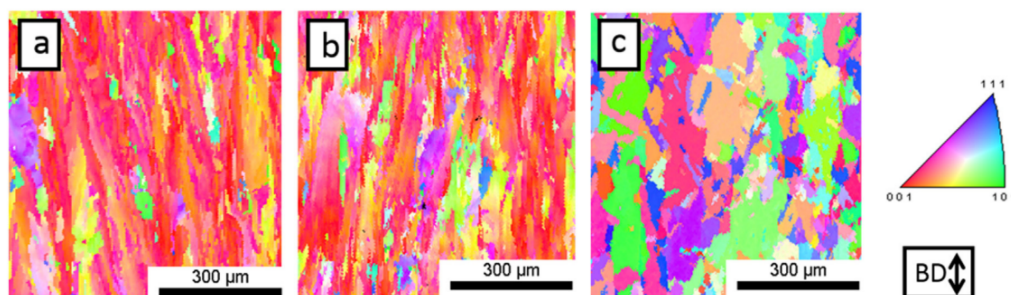


Figure 2.7: Inverse pole figure maps of Inconel 718 processed by SLM (a) as-printed, (b) solution annealed, (c) HIPed [24].

Homogenisation heat treatment has more effect on the microstructure than solution annealing due to the higher temperatures involved. It is already discussed that it is beneficial in dissolving the brittle Laves phases, homogenising the grain

structure and removing micro-segregation. In addition, it certainly has a small effect on the columnar grain structure as well. This is evident in Figure 2.8. Authors reported an increase in the grain size as well as development of random orientations after homogenisation heat treatment [5].

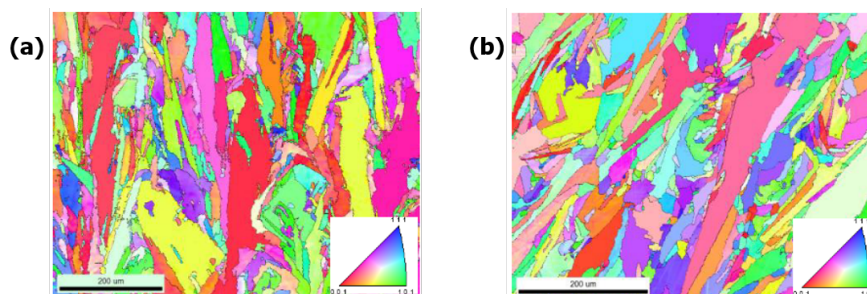


Figure 2.8: Inverse pole figure maps of Inconel 718 processed by SLM (a) as-printed, (b) homogenised [5].

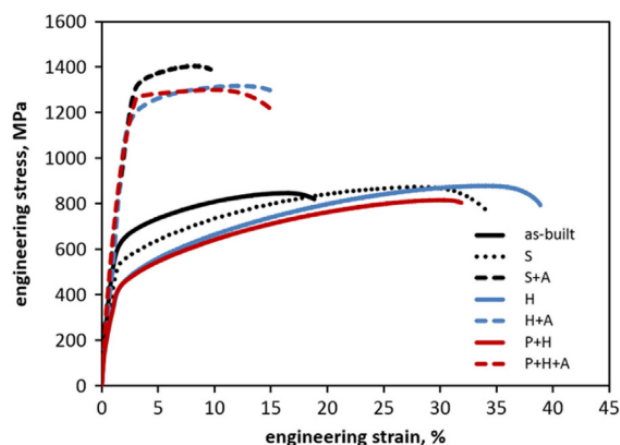
2.2.5. Mechanical properties

It has been consistently reported that the as-printed parts processed by AM are inferior compared to the properties of wrought material. This is natural considering that the production of wrought materials itself involves the heat-treatment steps that includes aging. This will form the strengthening γ'/γ'' phases while they are not formed in the as-printed IN718. However, a subsequent aging treatment is expected to improve the mechanical properties of printed IN718 [1, 20, 22, 24, 28, 29]. Table 2.3 summarises the tensile properties of IN718 processed via SLM, as well as through wrought and casting routes. As discussed previously, it is reported here that the as-printed parts possess strength more comparable to aged cast IN718 while these values are substantially lower than the aged wrought IN718. On the other hand they showcase better ductility than both wrought and cast material. Cast products are expected to showcase poor properties due to high amounts of defects and porosity. Also shown in this table are the tensile properties of SA (solution+aged) and HSA (homogenised+solution+aged) treated IN718. It is clearly seen that these conditions render the properties of printed IN718 into the ballpark of wrought material. A similar effect of the aging on tensile stress-strain curves can be seen in Figure 2.9. This shows why the heat treatments in the context of precipitation hardening are of utmost importance in all discussions involving super-alloys and IN718.

Alternately, many studies have also been done to evaluate the anisotropy observed in properties of AM IN718 owing to the typical $\langle 001 \rangle$ texture and columnar grains along the building direction [1, 30, 31, 32, 33, 34, 35, 36]. It has been mutually accepted in all the studies that printed IN718 showcases better tensile properties in a direction perpendicular to the building direction rather along building direction. The main reason associated with this is how the grain boundaries and shape of the pores produced during AM are oriented with the loading direction. String-like pores will be aligned along the loading direction between the subsequent layers for the vertically

Table 2.3: Room temperature tensile properties of IN718 processed via SLM [29].

Processing Condition	Yield Strength (MPa)	Tensile Strength (MPa)	Elongation (%)
As-printed	849	1126	22.8
Wrought (AMS5663)	1034	1276	12
Cast (AMS5383)	758	862	5
SA treated (AMS5663)	1084	1371	10.1
HSA treated (AMS5383)	1046	1371	12.3

**Figure 2.9:** Stress-strain behavior of SLM parts under tensile loading. Here S - solution annealing, H - hot isostatic pressing, A - aging and P - arc PVD [24].

built IN718 and thus provide easier path for fracture. On the other hand, grains oriented along the building direction will introduce more obstacles for the dislocation motion when the grain boundaries are perpendicular to the loading direction rather than along the loading direction. Hence improving the strength across the grain boundaries rather than along them. Table 2.4 summarises the results obtained from one such study. Clearly, the strengths are lower in direction along the building direction than perpendicular to building direction. This is valid for the results after post-processing as well.

HIPed IN718 post-processed with AMS 5664E will aid in improving the strength of printed material as it also involves the aging treatment. In fact, it is seen in Table

Table 2.4: Room temperature directional tensile properties of as-printed and post-processed IN718 processed via SLM [34].

Processing Condition	Tensile direction with BD	Yield Strength (MPa)	Tensile Strength (MPa)	Elongation (%)
As-printed	0°	734 ± 13	980 ± 10	22.8
	90°	837 ± 25	1067 ± 21	10.1
SA treated (AMS5663)	0°	1195	1361	12.3
	90°	1219 ± 24	1423 ± 43	12
HSA treated (AMS53833)	0°	1228	1398	15
	90°	1333 ± 29	1505 ± 33	14

Table 2.5: Room temperature tensile properties of HIPed IN718 processed via SLM [34]. (PBF - powder bed fusion and BPD - blown powder deposition)

Processing Route	Yield Strength (MPa)	Tensile Strength (MPa)	Elongation (%)
L-PBF	1087 ± 8	1385 ± 6	23 ± 1
L-BPD	1092 ± 33	1264 ± 25	12.3 ± 8
Wrought	1034	1241	12

2.5 that these materials have better tensile properties than the wrought IN718. This is expected since in addition to the precipitate strengthening and dissolution of brittle Laves phases, HIPing stage involved here also reduces the porosity and makes the grain structure equiaxed [34].

2.3. Functionally graded materials (FGMs)

Functionally graded materials (FGMs) are a result of locally tailored microstructures and/or compositions. This allows a swift shift in characteristics to accommodate two or more varying systems in a single component. Hence, FGMs are intentionally in-homogenised spatially to reap the benefits of local tweaks in the properties that in a unique way contribute to the superior bulk material properties. FGMs were introduced in the 1980s to replace the traditional thermal barrier coatings. FGMs were initially designed as a response to benefit from the novel composite nature and to incorporate the ability to control the abrupt shift across the interfaces. Many studies have ventured into the effect of such a piece-wise characteristics of man-made composites. These conventional composites have shown a tendency to possess deleterious effect on the bulk properties. This has been attributed to the cumbersome principles such as adhesion, stresses, defects, etc. as a result of abrupt changes and mismatch in properties at the interface. These interfaces act as stress concentrators and become favourable sites for cracking and/or de-bonding. Such interfaces can be overcome by introducing a continuous or a step-wise gradation in the material [37].

2.3.1. Types of FGMs

The concept of FGMs has been inspired from the naturally available materials such as that in the bone structure, bamboo [38], exoskeleton in crab shells [39], etc. With the main objective of tailoring the mechanical response to improve the damage tolerance, FGMs can be obtained with shifting characteristics by changing the inherent structure in three different ways which is seen also in Figure 2.10 and are introduced below [40].

Composition

This type FGMs can be obtained by spatially altering the chemical composition of the material to affect the chemical structure of the material from one plane to the other. This can either be a result of formation of different phases or the varying solid solubility of the elements incorporated in the solidifying single matrix phase.

Microstructure

This type of FGMs can be generated by incorporating a shift in the grain size or structure. Conventionally, this is a result of the cooling characteristics of the component when the surface of the material is rapidly quenched which then helps in generating different microstructure from the surface of the material to the core; elsewhere read as surface or case hardening. Other techniques such as the SLM which can affect the thermal profile of the material through it's cross section can also lead to such microstructure gradient FGMs.

Porosity

Herein, the porosity gradient in the material is gradually controlled in the bulk of the material. Ideally, the main objective here is to fabricate light-weight components for bio-implants in the biomedical applications. By controlling the porosity gradient, the density of the components can be varied to alter the mechanical properties of an implant wherever required while also aiding the implant's fixation and the surrounding tissue growth through the pores.

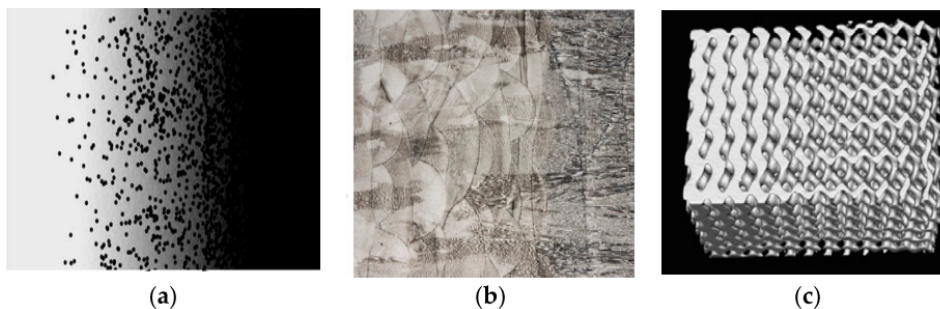


Figure 2.10: Types of FGMs according to (a) Composition gradient, (b) Microstructure gradient, (c) Porosity gradient [41].

2.3.2. A combination of SLM and FGMs

The effect of steep thermal gradients in the context of forming columnar grains with a strong $\langle 001 \rangle$ texture was discussed in section 2.2.3. However, this is not the general trend especially in cases where the thermal gradient is not high enough due to a scanning strategy with low laser power, high scanning speed or a large hatch spacing. Under such conditions with a lack of steep thermal gradient or a lack of strict unidirectional heat flow, the individual melt pools solidify with a similar grain structure shown in Figure 2.11. This image also helps in outlining that the epitaxial growth of dendrites along the $\langle 001 \rangle$ direction is still retained. The equiaxed grains seen near the melt pool boundaries are a result of this melt pool being the first layer to be deposited on the substrate. However, such a strategy with low net heat input can be employed to obtain a similar fine grain structure without texture and constricted to the individual melt pools as is seen here.

With such a difference in the effect of SLM processing condition on the final microstructure, component fabrication can be locally altered to change the final solidification structure and hence the local properties. Several such studies that focused on the influence of a low and high laser power were performed by

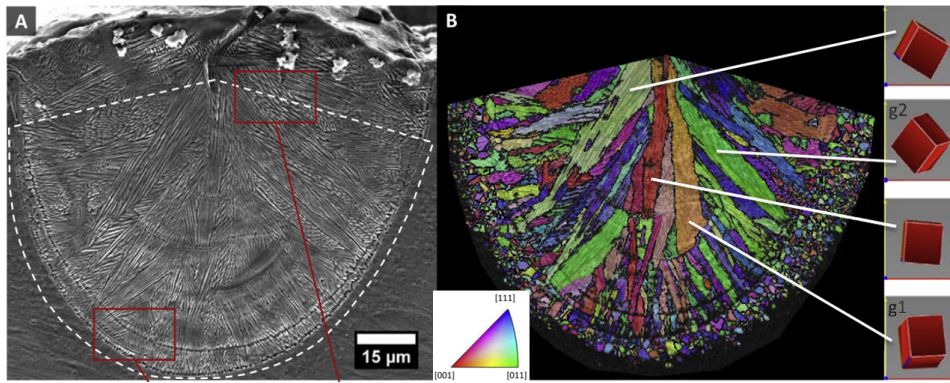


Figure 2.11: (a) SEM micrograph and (b) EBSD map of the melt pool grain structure in CoCrFeMnNi high-entropy alloy fabricated by laser powder bed fusion [42].

Popovich et. al. [30, 31, 32]. The main focus in these studies was to obtain components with a tailored microstructure as a result of intermittent shift in the processing condition during the fabrication itself. Hence, a functionally graded material can thus be obtained with microstructural design variation. This is done with the help of two different scanning strategies. The main variables in discussion here are the laser powers - 950 W and 250 W. Both these laser powers are seen to form a distinct microstructure. The 950 W laser power leads to coarse grains elongated along the building direction with a strong $\langle 001 \rangle$ texture while the 250 W leads to a fine equiaxed grains with no texture as seen in Figure 2.12. The two transient regions can also be seen at the interface between the three zones.

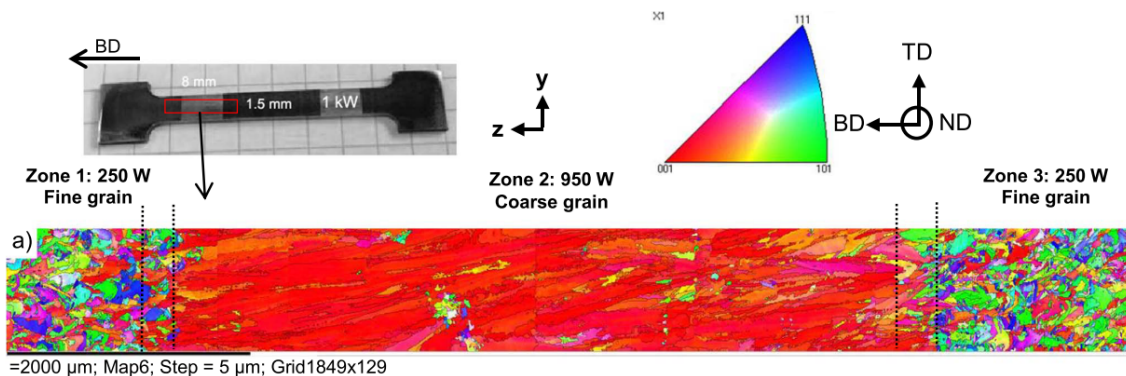


Figure 2.12: EBSD map of IN718 functionally graded sample fabricated by selective laser melting showing the 950 W zone sandwiched between two 250 W zones [30].

One of the other important findings from these studies is that there is a definitive correlation between the microstructure and properties by using different laser powers. By incorporating functional grading and suitable post-processing heat treatments, the authors were able to fabricate AM parts with room temperature tensile properties superior to the conventionally produced cast and wrought Inconel 718 [31]. Therefore, it is worthwhile to study such an effect in the context of other significant mechanical properties as well. One such important mechanical behavior is the material failure under cycling loading leading to fatigue.

Niendorf et. al. [43] performed a similar study on the anisotropy of 316L stainless steel produced using a laser power of 400 W. On the other hand, it is observed that

the steel produced with a laser power of 1000 W shows a strong <001> texture in the columnar grains elongated along the building direction. These observations are again consistent with the findings of Popovich et. al. It is also reported in these studies that the highly anisotropic fine grain microstructure came out on top with a higher yield strength and Young's modulus. While the textured coarse grain microstructure shows better % elongation.

2.4. Fatigue: Basics and Mechanisms

The failure under dynamic loading is a local phenomenon. Unlike static loading, and microstructural features such as the grain structure, defects, impurities, etc are play an important role in fatigue as they induce localised stress concentrations. Fatigue is an even more interesting topic because cyclically loading the material well below its tensile strength can also lead to failure. [44]

Damage evolution due to fatigue involves three stages: crack initiation, crack propagation and final fracture or rupture. Crack initiation exclusively begins at the sites of local stress concentrations such as inherent defects, notch or due to surface roughness. During this stage of Mode *II* shear loading, grain boundaries play an important role in introducing barriers to small cracks propping up on the surfaces. This is because of the change in slip orientations leading to a crack propagation through a less favored slip system. This may lead to the crack changing its direction or coming to a standstill until further load is applied which activates the less-oriented slip system. Many such cracks can be formed through the slip systems at the surface leading to a phenomenon called persistent slip bands. Such bands due to deformation act in a way as a notch. Due to such a complex mechanism, crack initiation is associated with a slow crack growth which makes it difficult to characterize crack propagation on the basis of this stage in fatigue [44, 45, 46].

Crack propagation stage on the other hand can be characterised easily due to fast crack growth during Mode *I* tensile loading and easier detection. An initiated crack grows along the principal stress directions Figure 2.13 shows a curve for fatigue crack growth rate derived from the empirical equation $da/dn = C(\Delta K)^m$. This equation is alternately labeled as Paris' Law where C and m are the material specific Paris constants [47]. $\Delta K = K_{max} - K_{min}$ is the instantaneous amplitude of cyclic stress intensity defined by $K = \sigma(\pi a)^{1/2}$ (σ is stress and a is crack length). From the curve it is clear that lower the steepness or m value, lower is the change in crack growth rate with a certain progression in ΔK . Region *II* in such a curve is termed as the Paris region. ΔK_{th} value is technically considered as the threshold stress-intensity below which the crack growth rate is virtually non-existent, that is close to zero.

During the crack propagation stage, a loading cycle will plastically deform the crack tip leading to a small opening and thus a small progression in the crack. On the other hand, the unloading cycle will close the crack but a deformed crack tip retains its width due to plastic strain. Such an opening and closing action over several cycles leave behind a typical fracture surface decorated with the *fatigue striations*.

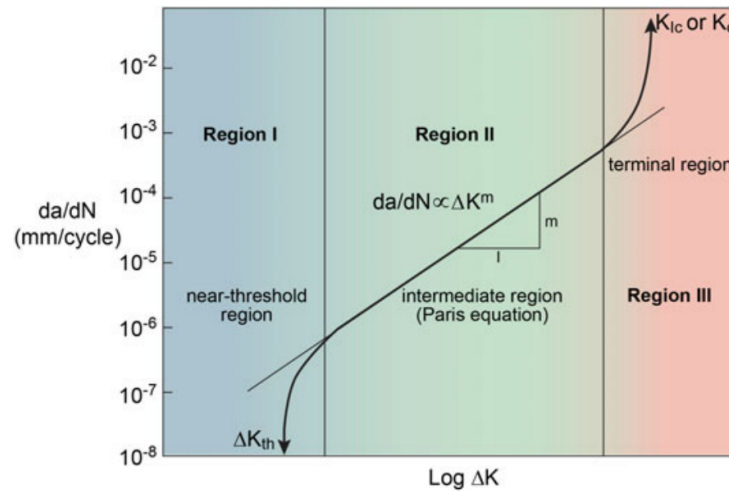


Figure 2.13: Schematic representation of da/dN versus ΔK fatigue crack growth under constant amplitude loading. [48]

Fatigue in AM and IN718

For parts produced with AM, surface finishing is an important step for improving their resistance to crack initiation under cycling loading [49]. However, the main focus of this study is to put more emphasis on the crack propagation stage under fatigue loading. As such, this section tries to conclude the findings of previous researches on this topic. Many studies have been previously conducted to investigate the fatigue in as-printed additively manufactured IN718 [23, 49, 50, 51, 52, 53]. All the studies indicate towards the inferior fatigue endurance performance of AM IN718 as compared to the wrought IN718. It has been a constant agreement that the lower endurance limits of as-printed parts is a consequence of the presence of pores, lack of fusion between built layers as well as process induced residual stresses leading to a reduced fatigue strength. Another important aspect covered by several studies is the anisotropy in fatigue behavior due to the variation in building orientation [23, 53, 54]. All the studies reported that the fatigue response changes with respect to the changes in building direction. As-printed AM IN718 when loaded in a direction perpendicular to the building performs better than parallel. As is the story with building directions, this is an outcome of the elongated columnar grains along building direction. Such grains introduce more grain boundaries along the crack path in one direction than in other. Grain boundaries are known to disrupt the dislocation motion perpendicular to the load in the case where load is parallel to the columnar grains. As seen before, the same reason was applicable for the better tensile properties in horizontally built AM IN718. Incorporation of post-process heat treatments has been reported to improve the fatigue performance of AM IN718 due to the precipitation of γ'/γ'' strengthening phases after aging step [55].

Many studies have also given substantial efforts to studying the fatigue behavior under constant load amplitude conditions. Such conditions are useful in procuring the da/dn v/s ΔK curve which was discussed before. Konecna et. al. [54] described the crack propagation for vertically built AM IN718 in Paris region by the equation

$da/dn = 2.25 \times 10^{-7} \Delta K^{2.31}$ (in ΔK range of 2-10 $\text{MPa}\sqrt{m}$). They also reported a rather low ΔK_{th} value of 3 $\text{MPa}\sqrt{m}$ when compared to the 13-14 $\text{MPa}\sqrt{m}$ value for wrought IN718 [56].

Another study based on the SLM IN625 was performed by Hu et. al. [57]. They studied the effect of build orientation on the fatigue crack propagation in solution and aging heat treated IN625 processed via SLM. It was reported that the IN625 tested parallel to building direction performed slightly better than those tested perpendicular to the building direction. The reason was associated with a higher degree of secondary cracking in the former than the latter. Secondary micro-cracks are expected to form owing to the precipitation strengthening. The subsequent effect was observed to be more pronounced in the threshold region than the Paris region.

A similar study was performed by Kim et. al. [58] that ventured into reflecting upon the building directions of SLM IN718 and their effects on the fatigue curves after solution and aging heat treatment. They reported a negligible effect of building direction on the da/dn values of IN718 parts manufactured via SLM. These parts showed better crack resistance than the conventionally manufactured wrought IN718 in threshold regions however SLM parts were inferior in lower as well as higher ΔK Paris regions.

2.5. Conclusions

A literature review has been provided to cover the important aspects that will eventually form the basis of the current study. The main conclusions drawn from this literature review are as follows,

- Inconel 718 is a Nickel based super-alloy initially designed to possess high temperature strength and excellent corrosion resistance. Recently, IN718 has also been used in applications at room temperatures or in cryogenic conditions.
- The main reason attributed to the high strengths in such super-alloys are the γ'/γ'' strengthening phases while the γ phase forms the matrix. Other phases formed in IN718 are the detrimental Laves phases, the metastable δ phase and MC type of carbides. A proper selection of standard post-process heat treatments is important in optimising the precipitation of favorable phases.
- Additive manufacturing is an evolving processing methodology especially for IN718. Selective laser melting was discussed as one such alternative to the conventional routes. Typical features associated with SLM are the effects of thermal gradients on the final solidification microstructure of IN718. An epitaxial dendritic growth accompanies the elongated columnar grains with strong $\langle 001 \rangle$ texture along the heat flow direction which in case of SLM also happens to be the build direction. The high cooling rates also promote precipitation of Laves phases in as-printed conditions. Presence of porosity and residual stresses form the other drawbacks associated with SLM and AM.
- The effect of standard post-processing heat treatments on the microstructure of AM IN718 was also discussed. Solutioning redistributes the precipitates, homogenisation dissolves Laves phases and reduces micro-segregation, HIPing reduces porosity while aging introduces the γ'/γ'' phases.
- This was followed up by studying the role of microstructure on the mechanical properties of AM IN718 in as-printed as well as post-process heat treated conditions. It is concluded that the tensile properties of as-printed AM IN718 are poor in comparison to the wrought IN718. These properties are even poorer when the loading direction is along building direction. AM IN718 properties can be improved by precipitation strengthening as a result of post-process heat treatments.
- The concept of functionally graded materials and different types of FGMs were introduced. The role of SLM process parameters in fabricating the tailored microstructures in FGMs is also discussed. Such tailored microstructures have been previously fabricated by essentially changing the effective energy density to obtain fine grain and coarse grain microstructures across interfaces.
- A basic background on the fatigue as a result of cycling loading is provided. It is reported that fatigue endurance performance shows anisotropy as it is relatively better perpendicular to building direction than along it, while both are substantially inferior compared to wrought IN718. This can be adjusted with post-processing heat treatments.

2.6. Research objectives

Based on the conducted literature study the following knowledge gaps have been identified:

- Fatigue crack growth behaviour in functionally graded AM IN718 (considering the grain size, orientation, and most importantly graded interface) as compared to conventional wrought material.
- Effect of post-process heat treatments on microstructural evolution in relation to fatigue crack growth in functionally graded IN718.

In order to address the above identified gaps the following research objectives were set for this study:

1. Study the variability of microstructure evolution in ungraded as well as graded specimens with the post-processing heat treatment AMS 5383 and compare with as-printed and AMS 5664E wherever necessary.
2. Perform a quantitative and qualitative analysis of the combined influence of grain size, grain orientation, functional grading and heat treatments on the fatigue crack propagation behaviour.
 - Develop Paris curves for ungraded heat treated specimens to complete the set of testing with as printed and hot isotactic pressed + heat treated specimens from the previous study.
 - Replicate constant ΔK tests for the graded heat treated specimens to evaluate any substantial crack arrest or changes in the crack growth rate at the interface.
3. Evaluate the underlying effect of microstructure evolution in all the specimen conditions on fatigue crack propagation through the interfaces in graded specimens with the aid of EBSD analysis and fracture surface analysis.

Materials and Methods

This chapter deals with the information on specimens used hereby, their processing conditions, experiments performed and the relevant experimental procedures.

3.1. Materials

A wide variation of specimens were used to realize the outcome of the research objectives underlined in section 2.6. Provided in the subsequent sections is a breakdown of the manufacturing parameters, post processing steps and a distinctive categorization of all the specimens used.

3.1.1. SLM fabrication and post processing

A gas atomized Inconel 718 powder was used in tandem with the SLM@280 HL facility (SLM Solutions Group AG, Germany). Two different Ytterbium fiber lasers with a wavelength of 1070 nm and maximum power outputs of 400 W and 1000 W were used to build the specimens at laser powers of 250 W (denoted as 250W) and 950 W (denoted as 950W) respectively which have been used in this project. The processing parameters shown in Table 3.1 have been derived from earlier research carried out by Popovich et. al. [30, 31, 32]. Further details pertaining the usage of laser powers are appropriately touched upon in the subsequent sections.

Table 3.1: SLM fabrication process parameters of the specimens

Laser power (W)	Laser scanning speed (mm/s)	Hatch distance (mm)	Layer thickness (μm)	Beam diameter (distribution type), (μm)	Volume energy density (J/mm^3)
250	700	0.12	50	80 (Gaussian)	59.5
950	320	0.5	100	100 (Flat top)	59.4

There are 2 distinct global types of specimens - **Graded (hereby denoted as G)** and **Ungraded (hereby denoted as UG)**. Two laser powers - 250 W and 950 W have been used to fabricate the UG specimens and will also be rightfully denoted wherever necessary. The significance of using these laser powers has been discussed briefly in section 2.3.2. While the G specimens have been fabricated by intermittent shift in the laser power from 250W to 950W to affect the grain size of the components across the interface where this shift takes place. Hence a single G specimen will not be distinguished on the basis of laser power hereafter.

A further division is done on the basis of post processing heat treatment applied to the specimens or the lack of it. There are three divisions on this basis: **As-Printed (AP)** specimens which were retrieved as it is after the SLM printing, **Heat Treated (HT)** specimens with AMS 5383 post processing heat treatment, and **Hot Isostatic Pressing and Heat Treated (HIPHT)** specimens with AMS 5664E post processing heat treatment. Refer Table 3.2 for the heat treatment conditions specified according to the standard. The term 'heat treated' for the remainder of this text will correspond to the homogenisation and solutioning followed by double aging while 'HIPing' will correspond to the hot isostatic pressing.

This research also focuses on the variation of the building direction of the specimens relative to the notch and post-testing crack direction which will be explained in the next section.

Table 3.2: Standard heat treatments applicable to IN718 according to SAE (Society of Automotive Engineers) [1, 12, 13].

Standard	Heat treatment	Temperature	Hold time	Cooling
AMS 5663	Solution	980 °C	1 h	Air cooling
	Aging	720 °C	8 h	Furnace cooling to 620 °C at 55 °C/h
		620 °C	8 h	Air cooling
AMS 5383	Homogenisation	1080 °C	1.5 h	Air cooling
	Solution	980 °C	1 h	Air cooling
	Aging	720 °C	8 h	Furnace cooling to 620 °C at 55 °C
		620 °C	8 h	Air cooling
AMS 5664E	Hot isostatic pressing	1180 °C at 150MPa pressure	3 h	Furnace cooling
	Homogenisation	1065 °C	1 h	Air cooling
	Aging	760 °C	10 h	Furnace cooling to 650 °C at 55 °C
		650 °C	8 h	Air cooling

3.1.2. Specimen geometries and categorization

ASTM E399 [59] specifies the specimen dimensions for Single Edge Notched Bending (SENB) specimens used for fatigue testing. Specimens used in this study have been designed according to this standard and are suitable for three point bending tests. The final dimensions of the specimens achieved after milling have been shown in Figure 3.1. The specified notch (inset) having total depth of 0.5 mm and radius of 0.2 mm was machined using Electro-Discharge Machining (EDM).

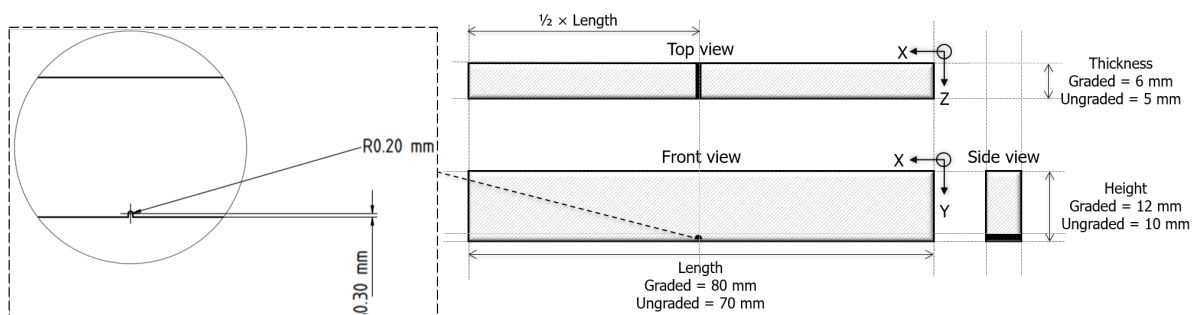


Figure 3.1: Schematic showing dimensions of the IN718 samples fabricated in this research. Notch specifications are seen in the inset.

Each set of specimens from AP, HT and HIPHT has a total of 5 divisions, 2 in G and 3 in UG. The inherent characteristics for their distinction is outlined below.

Ungraded (UG)

It is mentioned in section 3.1.1 that this study utilised specimens fabricated with two laser powers - 250 W and 950 W. Section 2.3.2 shows the relevant effect of laser powers on the inherent microstructure. With the 250W laser power, a relatively fine grained and equi-axed microstructure is expected to be obtained while with the 950W laser power, a directional microstructure with coarse and columnar grains is expected. Hence, this study will also focus on the directionality of SLM fabricated specimens with 950 W laser power. Two building directions (BD) were used to fabricate the specimens with 950W laser power. These specimens are designed so that the anticipated **crack direction (CD)** is either perpendicular or parallel to the **building direction (BD)**. While for the 250W specimen, the BD is always parallel to the CD as shown in Figure 3.2 (c). Figure 3.2 (a) and (b) show schematic symbols for the UG specimens fabricated with 950 W laser. The schematic depicts the expected coarse grain orientation for both the BD with respect to CD.

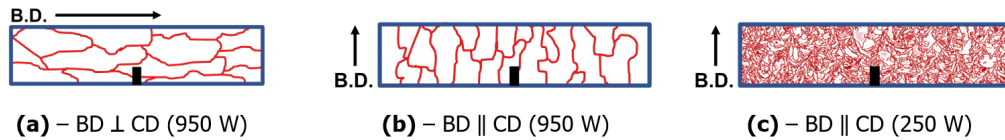


Figure 3.2: Ungraded (UG) specimen symbols showing the correlation between the building direction (BD) & grain size/direction, and orientation of BD with respect to the crack direction (CD) per specimen.

Graded (G)

Grading is a result of fabricating a single specimen with an intermittent shift between the laser powers (from 250 W to 950 W). For all the G specimens, this shift takes place halfway through the specimen height. The two possibilities with BD either perpendicular or parallel to the CD are shown in Figure 3.3. Essentially the G specimens are a combination of the individual microstructures of UG specimens, with the expected fine equi-axed grains in one half and the coarse columnar grains in the other half.

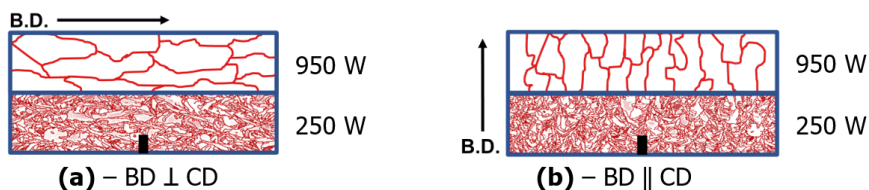


Figure 3.3: Graded (G) specimen symbols showing the combination of individual laser powers used per specimen.

3.1.3. Graphical summary

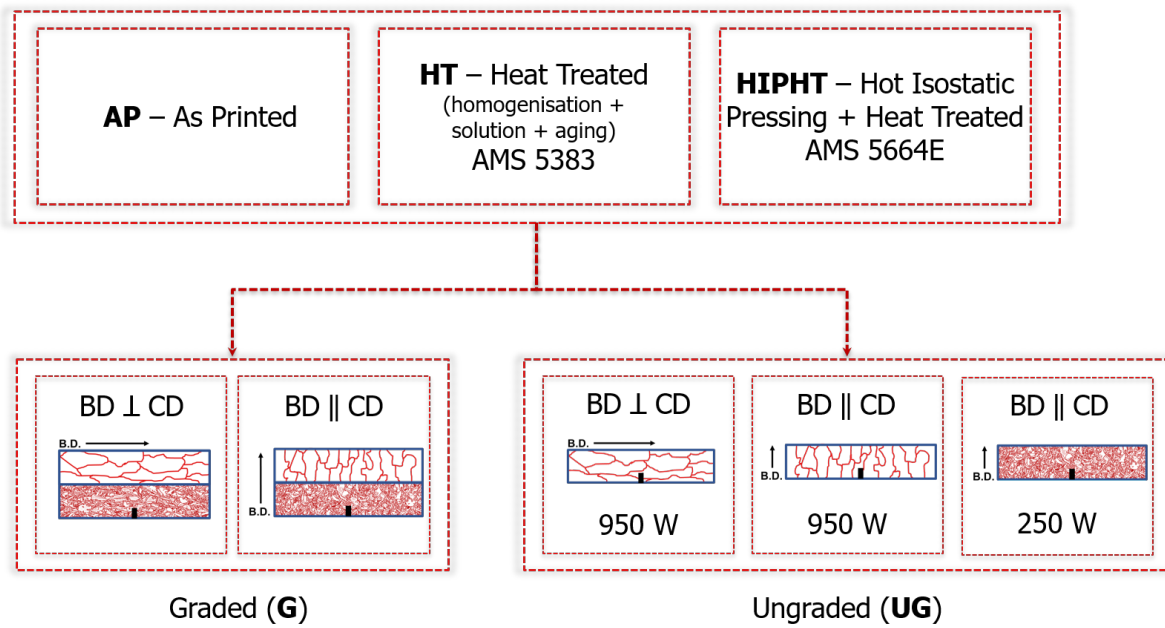


Figure 3.4: A flow chart showing a distinction between the specimens on the basis of post processing heat treatment, building direction and the different combinations of laser power used in this study.

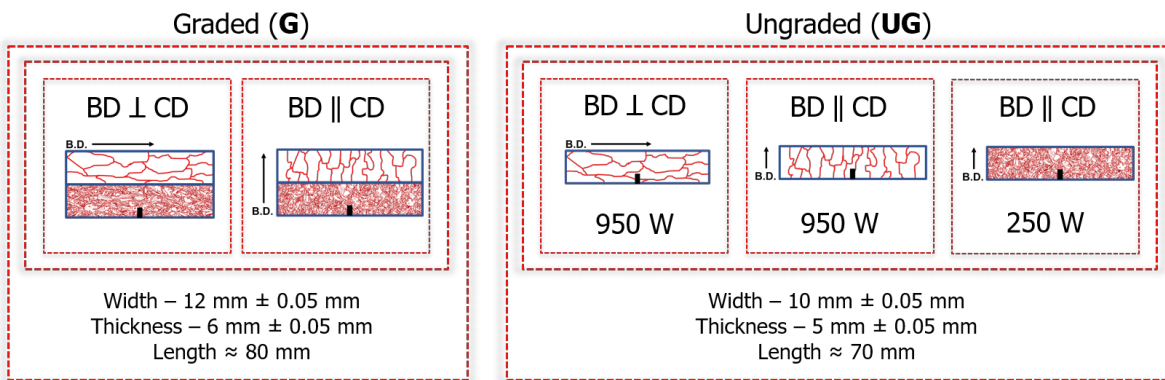


Figure 3.5: A flow chart showing a distinction between the specimens on the basis of their dimensions according to the respective fabrication methodology.

3.2. Microstructure characterization

3.2.1. Microscopy

After the milling procedure, specimens used in this study were used as is for characterizing the microstructure. SiC abrasive papers with a grit size from 180 till 2000 were used for grinding the specimens on their longest faces (XY plane of the specimen in Figure 3.1). The specimens were subsequently polished to a mirror finish with 3μ and 1μ diamond slurry. In order to reveal the microstructure on these polished surfaces, *HT* and *HIPHT* specimens were etched with Kalling's reagent (5g CuCl_2 , 100 ml HCl, 100 ml ethanol) while *AP* specimens were etched with Glyceregia (5 ml HNO_3 , 10 ml Glycerol, 15 ml HCl). The microstructure was then observed under optical microscope (Leica DMLM) and scanning electron microscope (Jeol JSM IT-100). Microscopy was primarily used to observe the grain structure in directions parallel and perpendicular to the build. Other features observed are the precipitates, carbides, porosity, etc.

3.2.2. XRD analysis

The main goal of carrying out XRD analysis was for phase determination in *AP*, *HT* and *HIPHT* specimens. The phase determination analyses were performed only on XY planes (refer Figure 3.1) in the ungraded (*UG*) specimens. XRD measurements were performed using the Bruker D8 Advance Diffractometer and $\text{Co-K}\alpha$ radiation on a beam size of 0.5 mm diameter. The step size used is $0.040^\circ 2\theta$ with 45 kV and 35 mA in 2θ range of $20^\circ - 140^\circ$. The peak identification and data evaluation was done using Bruker software Diffrac.EVA vs 5.0. The XRD setup can be seen in Figure 3.6.

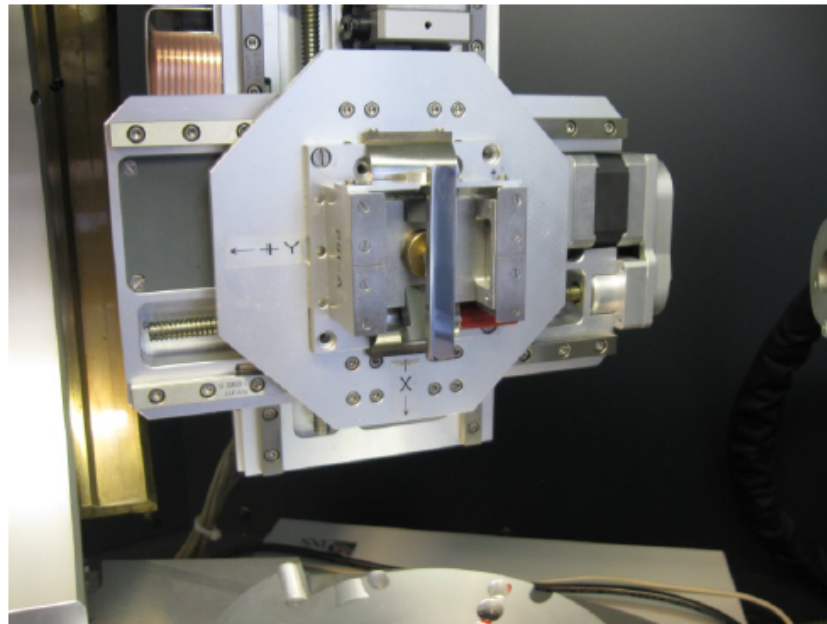


Figure 3.6: Image showing XRD setup with the specimen arranged inside.

3.2.3. Hardness measurement

Specimens for hardness measurements were prepared in a similar way as that for microscopy. Except that the etching stage is entirely eliminated. A set of 10 measurements were done at several positions for each specimen using a Durascan microhardness tester provided by Ecos workflow.

3.2.4. EBSD analysis

For EBSD analysis, samples with dimensions 20 mm × 12 mm × 6 mm were retrieved from the graded specimens that were tested using constant ΔK tests (detailed explanation in section 3.3.3). These specimens were retrieved such as to include the cracks on the XY plane of the specimen (refer Figure 3.1) after testing at the centre. The specimen thus produced are ground with 2000 grit sanding paper and cloth-polished with 3 μ and 1 μ diamond slurry until a surface with mirror finish is obtained. A last step of cloth-polishing was performed with 0.4 μ OP-S alumina slurry until the inherent build layers are revealed to the naked eye. The last stage is also beneficial in marking the interfaces in these specimens.

The main motive of performing EBSD analysis was to reveal the microstructure at the surface along crack path in graded specimens. All the measurements were performed using SEM Mira 3 Tescan at accelerating voltage of 20 kV and a step size of 1 μ for *AP* and *HT*, and 0.5 μ for *HIPHT*. The scans were retrieved and converted to a supported format using a channel 5 - HKL software. EBSD data was analysed and the inverse pole figure (IPF) orientation maps were processed using the TSL-OIM software. The cleanup techniques used while processing are the Neighbour CI correlation (Level = 3) followed by Grain Dilation (Grain Tolerance Angle = 15 and Minimum Grain Size = 8). The parameters mentioned have been obtained by trial and error to arrive at the best possible outcome. The feature of Image Quality (IQ) threshold filtering was also employed to overlay the grain boundaries and crack onto the processed IPF maps.

3.2.5. Fracture surface analysis

The specimens for performing the the fracture surface analysis were obtained by simply overloading the graded specimens that were used during the constant ΔK tests. Overloading breaks these specimens into two halves thus revealing the fractured surfaces on the YZ plane of the specimen in Figure 3.1. The surfaces from both the halves were cleaned using isopropanol, coupled together and preserved in a dessicator before the final inspection. These halves were then mounted on a sample holder and placed upright into the SEM chamber for acquiring the desired micrographs.

3.3. Fatigue testing

The contents of this section describe the fatigue testing methodologies implemented to obtain the desired characterization of fatigue crack propagation behavior - in the individual ungraded (UG) samples as well as graded (G) specimens with interface. Dummy tests were performed with aluminium and wrought Inconel 718 specimens to undergo the training procedure and understanding the setup itself. The test setup used for both the category of specimens remains the same and is explained in the following section.

3.3.1. Test set-up

Figure 3.7 shows the servo-hydraulic loading unit used. It is a table top MTS machine with hydraulic grip heads (1), actuator attached to the top grip and a cross-head mounted load cell. Platform (2) attached to the lower grip serves as the main support for the specimens. This platform is made with S690 steel. The sample fixtures (3) clamp the specimen (6) into position between the support rollers (4). The specimen is insulated from platform by attaching small layers of GLARE material (not seen in the images). Two rollers are permanently glued to the support and one to the top head, thus act as the three contact points of loading in the SENB specimen used here. These rollers are made according to the ASTM-E399 standard. Reference marks were made by scratching the specimen surfaces at an interval of 0.5 mm from the edge of the notch until 7 mm height. Two Limes cameras (5) were used to monitor these reference marks on either side for visual crack calibration. Primarily done to determine the dependence between the actual crack length and the voltage measurements from Direct Current Potential Drop (DCPD) equipment. The equipment itself is not shown here. The DCPD setup supplies current to the specimens through connecting wires (7), and the probe wires (8) attached to the fixtures measure the voltage drop across the specimens at two positions - close to the crack and away from the crack. The schematic drawings of the fixtures, rollers and support are provided in the appendix. A rigorous calibration procedure was required to tune the whole setup. To keep the contents concise, this procedure is not mentioned here. Refer appendix 6.1 for fixture drawing.

3.3.2. Fatigue characterization of ungraded specimens

Characterizing the fatigue crack propagation behavior of individual microstructures in the ungraded (UG) specimens involved two procedures. The first one determines the ΔK_{th} (threshold). This procedure will be called as constant K_{max} test hereon. The second one determines crack growth rate as a function ΔK values under constant load amplitude (and hence the name). Both the procedures rely on the existing sharp crack progression other than the notch itself. This crack is called as pre-fatigue crack and was produced as per the standard. For the tests in this study, the length of pre-fatigue cracks was 2 mm. To initiate the crack, higher load levels are required which are then decreased as the crack-length increases. The crack length calibration with the voltage measurements were also done with the pre-fatigue crack formation.

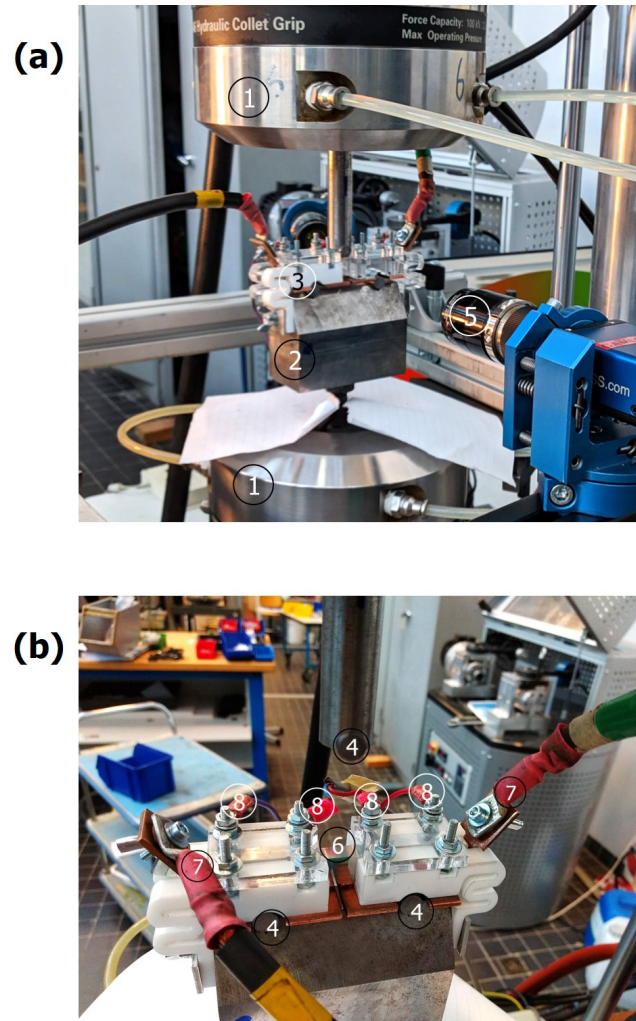


Figure 3.7: Images showing the testing setup (a) front view and (b) top view. (1) MTS machine, (2) main support, (3) specimen fixture, (4) support rollers, (5) cameras, (6) specimen, (7) current supply from DCPD, (8) DCPD probes.

Constant K_{max} tests / Threshold tests: These tests involved choosing a value of K_{max} such that the ΔK value was high enough leading to crack propagation in the initial stages. All the threshold tests were performed at a frequency of 30 Hz in K control mode. With the starting stress ratio of $R = 0.1$ ($R = K_{min}/K_{max}$), a K_{max} value can be calculated from Equation 3.1. The value obtained was then constant for the remaining procedure. On the other hand, K_{min} is linearly ramped up to decrease the K amplitude until the crack growth rate drops below 1×10^{-6} mm/cycle. The instantaneous K_{min} can be calculated from Equation 3.2, where K_0 is the initial K_{min} , $C = -0.4 \text{ mm}^{-1}$ is the stress intensity gradient defined according to the test itself. a_0 and a are the initial and instantaneous crack lengths respectively. Figure 3.8 shows the graphical representation of the ramping up procedure.

$$K_{max} = \frac{\Delta K}{1 - R} \quad (3.1)$$

$$K_{min} = K_0 \exp(C(a - a_0)) \quad (3.2)$$

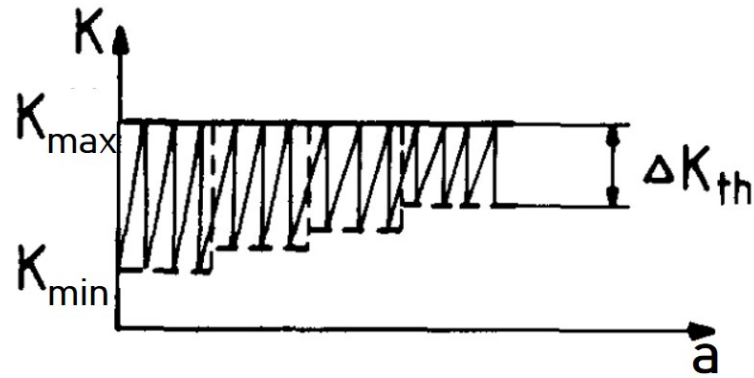


Figure 3.8: Schematic showing the ramping up phenomenon of K_{\min} in constant K_{\max} tests.

Constant load amplitude tests / Crack growth rate tests :

The fatigue crack growth tests were done under constant load amplitude at a frequency of 50 Hz using procedure mentioned in the standard ASTM-E647 [60]. As mentioned previously, reference marks at a regular intervals of 0.5 mm were scratched on the specimen surfaces. This is done to aid the calibration of voltage signal with crack length at the end of tests. The crack length is visually recorded using the two cameras at several positions and the corresponding voltage signals from the DCPD are also noted down. The raw data recorded includes the peak/valley load, voltage and cycle numbers. Voltage are converted to crack length using the calibration obtained. All these values are then fed into a Matlab algorithm provided in appendix 6.2. The Matlab algorithm systematically processes these values to generate da/dn and ΔK values and their plot thus reveals the fatigue curves.

3.3.3. Fatigue characterization of graded specimens

FEM model to obtain K solutions for constant K amplitude tests

Fatigue characterization of graded specimens is done with the aid of constant K amplitude tests. Constant ΔK tests help in understanding the effect of microstructure on the fatigue crack propagation. As a result, the effect of interfaces in graded specimens can be isolated on the basis of their fatigue behavior. In these tests, ΔK is held constant with the fatigue crack progression to record the changes in crack growth rate. For a particular microstructure, the crack growth rates obtained from this test should more or less be constant. However, varying the load levels to maintain a constant ΔK value requires accurate estimation of the K solutions. Ideally, these are calculated from the standard K solutions provided in the literature.

The standard K solutions used in determining the load levels as a function of $f(a/W)$ are only applicable for homogeneous materials. Here, the definition of homogeneous material is the one with a constant Young's Modulus (E). However, the graded materials under consideration for this part of the study are specifically produced with in-homogeneous microstructure to incorporate grading across the interface. Microstructure directly affects the material properties and hence the value of E is expected to be dependant on the grading. This leads to a need for using customized K solutions for doing the constant ΔK tests. Hence, finite element

modeling is required to estimate the accurate K solutions. Previous work by Sahu et. al. [12] studied this same phenomenon on the principle that E of the graded material varies as a function of grading between E of the two homogeneous components. Hence for such materials with grading, it is also required to estimate E for two parts under consideration here - 250W fine grain microstructure and 950W coarse grain microstructure. The displacement method was employed to estimate these E values from the three point bending tests.

The finite element modeling was done using ABAQUS software to find the custom K solution applicable to the graded materials used in this study. This model formulated graded specimen containing two halves of coarse grain and fine grain separated by a 1 mm interface. With the assumption that the Young's Modulus (E) is constant in the two halves, the interface is modelled as an elastic material divided into 5 layers of thickness 0.2 mm. These layers are then assigned a linearly changing value of Young's Modulus. With the expectation that K varies for different crack lengths, tiny elements of 0.02 mm are also modelled at the crack tip at different pre-defined positions. The J integral value is then calculated for a small boundary around the crack tip. Readers are referred to Sahu et. al. [12] for a more detailed explanation on the model. The stress intensity K was then calculated as per equation,

$$K = \sqrt{J \times E / (1 - \nu^2)} \quad (3.3)$$

where E is the Young's Modulus at the crack tip, J is the J integral values obtained from the model and ν is the poisson's ratio. The E of the two halves in these specimens was calculated using the Displacement method as mentioned below.

Displacement method for E modulus The displacement during three point bending is related to the stiffness and cracklength as given by Tada as follows:

$$\Delta_{total} = \Delta_{crack} + \Delta_{no-crack} \quad (3.4)$$

$$\Delta_{crack} = \frac{3.P.S^2(1 - \nu^2)}{2.E.B.W^2} V_2\left(\frac{a}{W}\right) \quad (3.5)$$

$$V_2\left(\frac{a}{W}\right) = \left(\frac{\frac{a}{W}}{1 - \frac{a}{W}}\right)^2 \left\{ 5.58 - 19.57\left(\frac{a}{W}\right) + 36.82\left(\frac{a}{W}\right)^2 - 34.94\left(\frac{a}{W}\right)^3 + 12.77\left(\frac{a}{W}\right)^4 \right\} \quad (3.6)$$

$$\Delta_{no-crack} = \frac{P.S^3}{4.E.B.W^3} \quad (3.7)$$

In the set of equations above, P is the load, S is the span length, ν is the poisson's ratio, E is the modulus at the crack tip, B is the thickness of the specimens, W is the width of the specimen and a is the cracklength. The displacement recorded from the fatigue tests is Δ_{total} . For a given value of load P, the modulus E can then be easily calculated.

The E values thus obtained are shown in Table 3.3. The E values obtained from displacement method are representative for these specimens and are only to be used for further calculations in this study. This stems from the notion that displacement method used here for calculating E is not a standard procedure and hence may contain systemic errors.

Table 3.3: Summary of values for Young's Modulus (E) obtained from Displacement Method through the three point bending tests

Processing Condition	Laser Power / Grains	Specimen	Young's Modulus (E in GPa)
As - printed (AP)	950 W / Coarse	BD \perp CD	139 \pm 36
	950 W / Coarse	BD \parallel CD	136 \pm 10
	250 W / Fine	-	186 \pm 15
Heat treated (HT)	950 W / Coarse	BD \perp CD	132 \pm 8
	950 W / Coarse	BD \parallel CD	130 \pm 9
	250 W / Fine	-	159 \pm 21
Hot isotactic pressed +	950 W / Coarse	BD \perp CD	134 \pm 25
	950 W / Coarse	BD \parallel CD	140 \pm 27
Heat treated (HIPHT)	250 W / Fine	-	173 \pm 28

Constant ΔK tests

The guidelines for introducing sharp pre-fatigue crack to the notch remains the same as mentioned before. Here as well, the crack length was visually recorded and calibrated with the voltage. However, to maintain a constant ΔK value, it was necessary to continuously feed these calibrated values back into the software as it changes the load levels in the K control mode. This was done in real time using a third degree polynomial fit of crack length v/s voltage measurement. As mentioned above in section 3.3.3, the K solution that was used for graded specimens is obtained from the FEM model.

3.3.4. Graphical summary

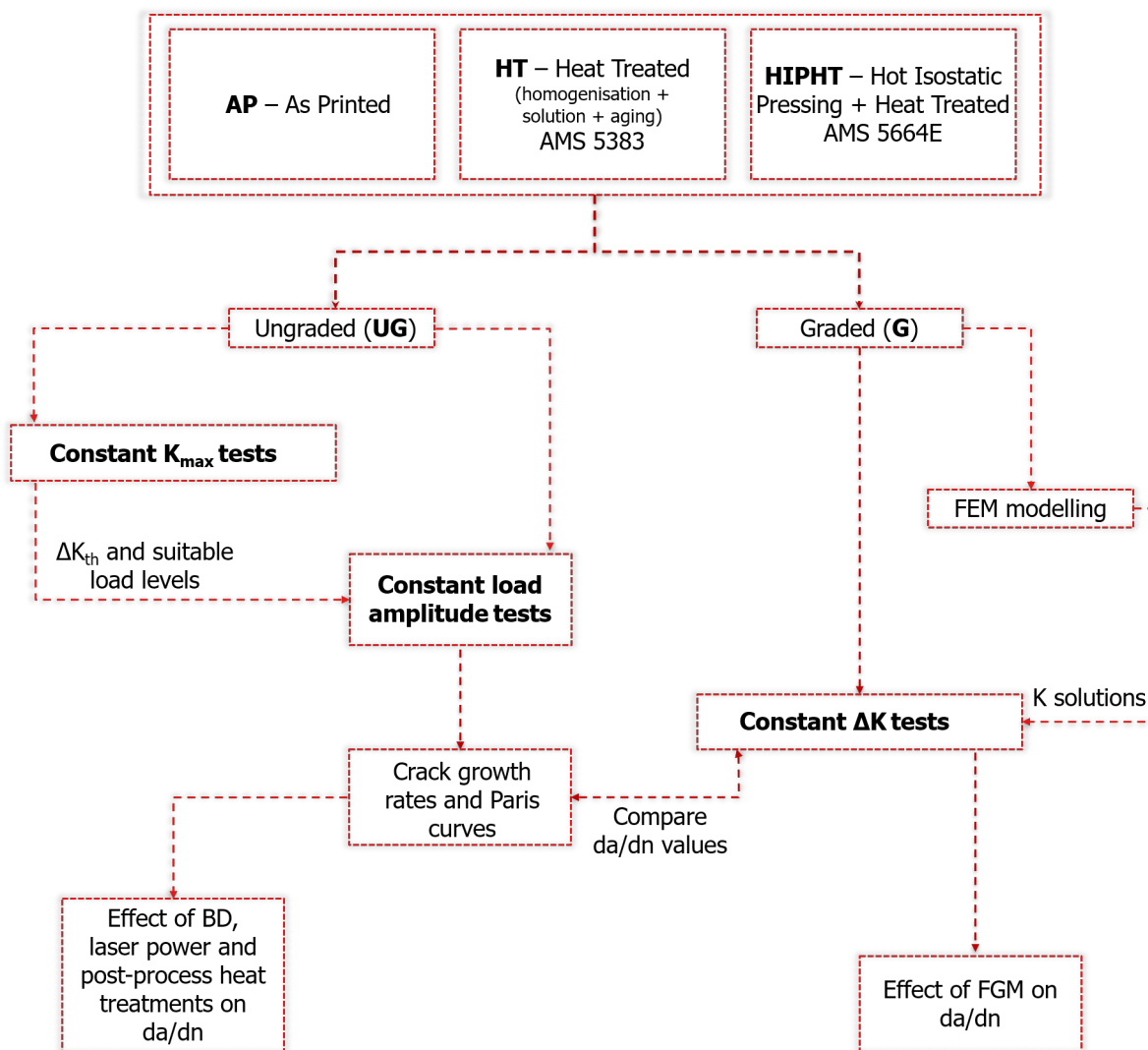


Figure 3.9: A flow chart showing the different test methodologies adopted to characterize the fatigue crack propagation in individual microstructures of ungraded specimens and the effect of tailored microstructure of FGM on the crack propagation.

Results and Discussion

4.1. Microstructural characterization

The following chapter deals with the study of microstructure in the context of grain structure using microscopy, phase identification using XRD and micro-hardness. The chapter begins by introducing the printed microstructure seen in the as-printed (*AP*) specimens obtained for this study. This helps in understanding the characteristic grain structure produced by SLM process. Subsequently, the primary focus will be on the effect of post processing heat treatment on these specimens. The specimens thus obtained are categorised as heat treated (*HT*). As a continuation from a previous study, appropriate comparisons are made with the hot isotactic pressed and heat treated (*HIPHT*) specimens wherever necessary. All the micro-graphs shown in this section have been recorded for a XY plane containing both the building direction (BD) and the crack direction (CD). XY plane is the specimen face with length and height in Figure 3.5.

4.1.1. Effect of laser power and build direction on the grain structure in as-printed condition

Figure 4.1 shows the melt pools (Gaussian features) in *AP* condition for a specimen with BD \parallel CD. Figure 4.1 (a) represents melt pools for 950W specimen while Figure 4.1 (b) represents melt pools for 250W specimen. It has been already established that for 250W specimen a fine grain microstructure is obtained and this micrograph helps in understanding how the inherent grain structure is related to the melt pools. On observing an individual melt pool, the main conclusion that can be drawn is that in general the solidification structure is strictly restricted to that specific melt pool. This structure in retrospect can be deemed similar to the solidification structure seen in ingots wherein the columnar grains grow from the mold towards the centre. It is seen here as well that the columnar grains grow from the melt pool boundaries towards the centre later appear to be equiaxed in nature with the epitaxial growth of γ dendrites within the grains. Such a growth was well documented by Pigliione et. al. [42] (as seen in Figure 2.11).

On the other hand, the solidification structure for 950W specimen is quite straightforward with the columnar grains aligned to the BD and penetrating several melt pools. The penetration aided by the steep thermal gradients produced

with a high heat input involving 950 W laser power.

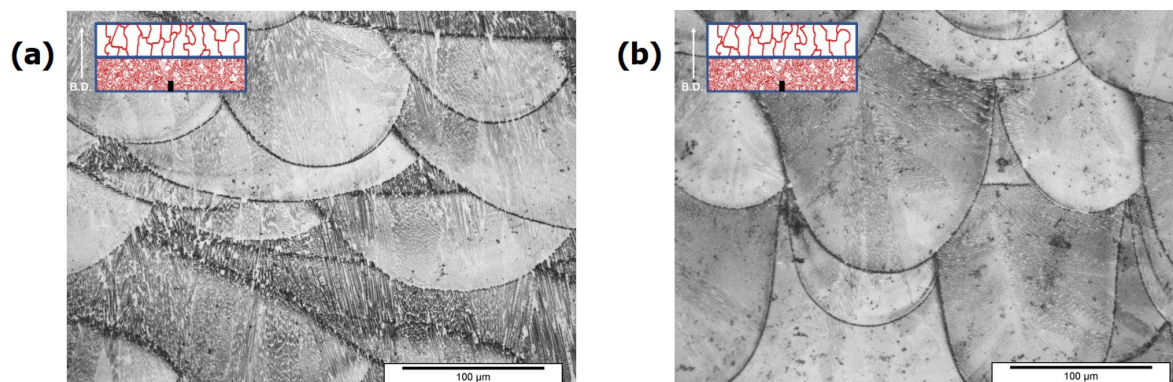


Figure 4.1: Optical micrographs of AP specimen for the regions produced using (a) 950 W laser power and (b) 250 W laser power.

Optical micrographs of AP specimens fabricated with 950 W laser power with $BD \parallel CD$ and $BD \perp CD$ are shown in Figure 4.2 (a) and (b) respectively. These micrographs help in understanding how the orientation of melt-pools is intertwined with the BD. For both the cases, melt-pools are seen to have solidified along the BD which is natural considering that the plane of scanning will always remain perpendicular to BD. More interesting to note however is the arrangement of grains and dendrites in these cases. As seen previously, 950W specimens will have coarse grain microstructure due to the columnar grains elongating along the heat flow direction and thus BD. The same is seen in these micrographs as well. More emphasis is laid upon the relationship between grain orientation and BD while discussing effect of post-processing heat treatment on HT specimens in the next section.

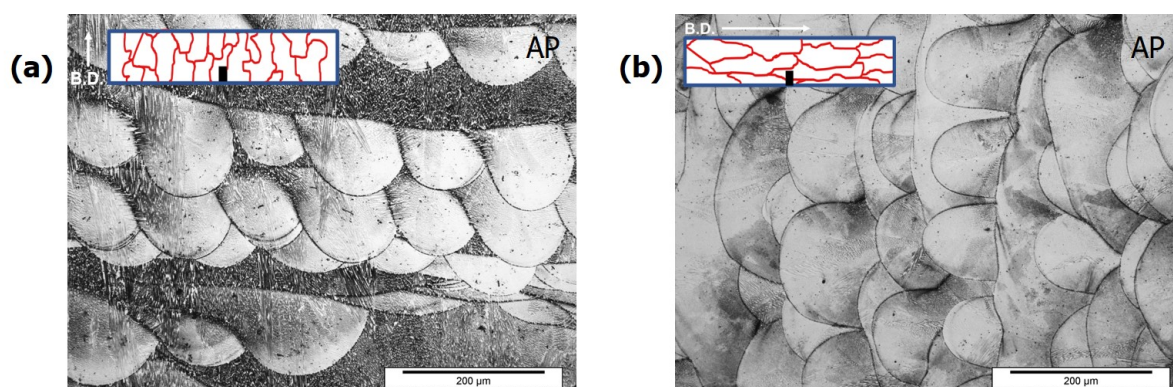


Figure 4.2: Optical micrographs showing 950W as-printed (AP) specimens with (a) $BD \parallel CD$ and (b) $BD \perp CD$.

SEM micrographs of AP specimens showing the combined effect of laser powers and then the BD. Figures 4.3 (a) and (b) represent specimens produced with 250 W and 950 W laser powers respectively. Observations about the random orientations of near equi-axial columnar grains in the former while elongated grains along BD can

be seen in the latter. Figures 4.3 (b) and (c) show that for the 950W specimens, longitudinal grain directions as well as dendritic growth, both are largely bound with BD. The SEM micrographs also help in distinguishing the dendrites from other microstructural features. It is seen here that the dendritic growth follows a close relationship with the grain elongation direction for 950W specimens and thus again the BD.

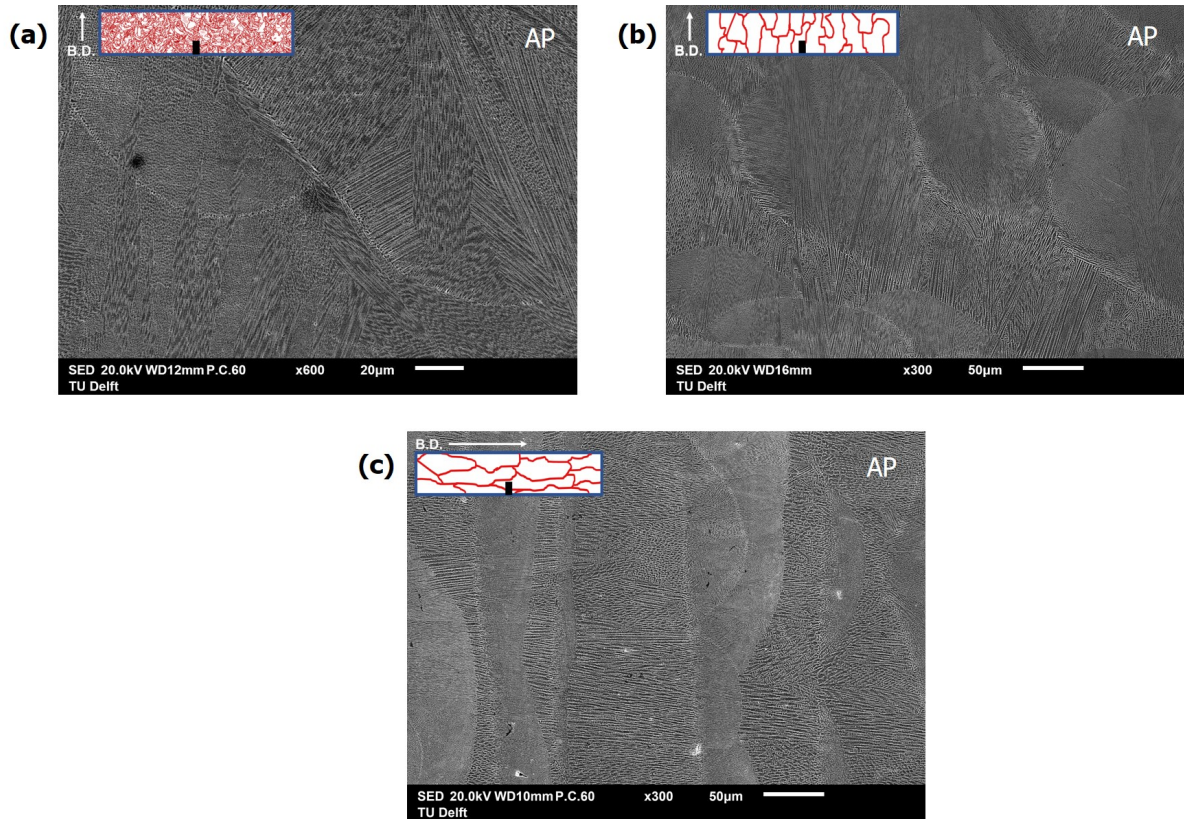


Figure 4.3: SEM micrographs showing as-printed (AP) specimens produced using (a) 250 W laser power, (b) 950 W laser power with BD \parallel CD and (c) 950 W laser power with BD \perp CD.

4.1.2. Effect of post-process heat treatments

It is expected that the characteristic grain growth for both 250W and 950W is not completely erased after homogenisation and solution heat treatment followed by aging. This is also evident from the microstructure study of *UG-HT* specimens in this section. Although in *HT* specimens it is still difficult to validate the effect of melt pools as the melt pool tracks are not visible after such a heat treatment.

Heat treated

Coarse grained microstructure produced with 950 W laser power: Figure 4.4 shows the optical micrographs of *UG-HT* specimen with BD \perp CD. It can be clearly seen that orientation of grain elongation is along the BD of the specimen. This indicates that the temperatures involved in homogenisation heat treatment step are not high enough to dissolve the grain structure obtained in the typical printed microstructure. A very faint pattern of the building layers can also be seen at both

the magnifications. The dendritic structure of the γ matrix for these specimens cannot be confirmed from the optical micrographs but their presence is validated through the electron micrographs in Figures 4.5 (a) and (b). The electron micrographs also confirm the previous observation that the grain orientation is along the BD but also that the γ dendritic growth is also along the BD.

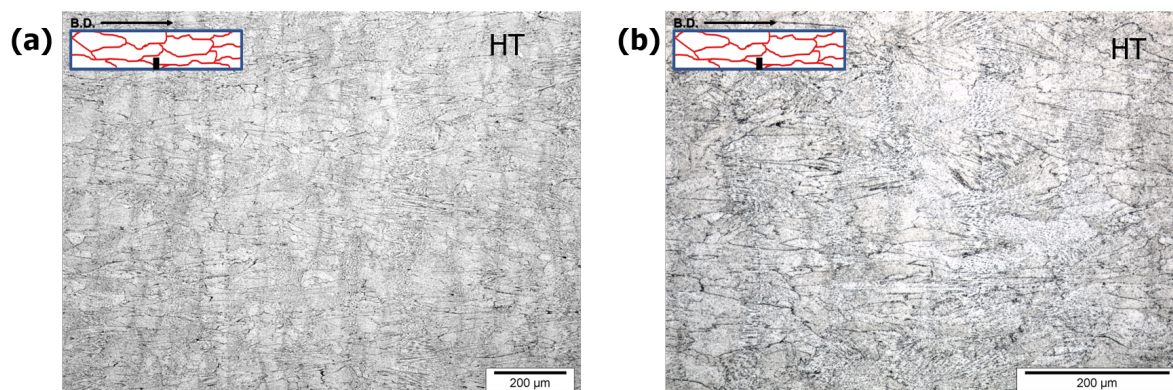


Figure 4.4: Optical micrographs of 950W UG-HT specimens with $BD \perp CD$ at a magnification of (a) 5X and (b) 10X.

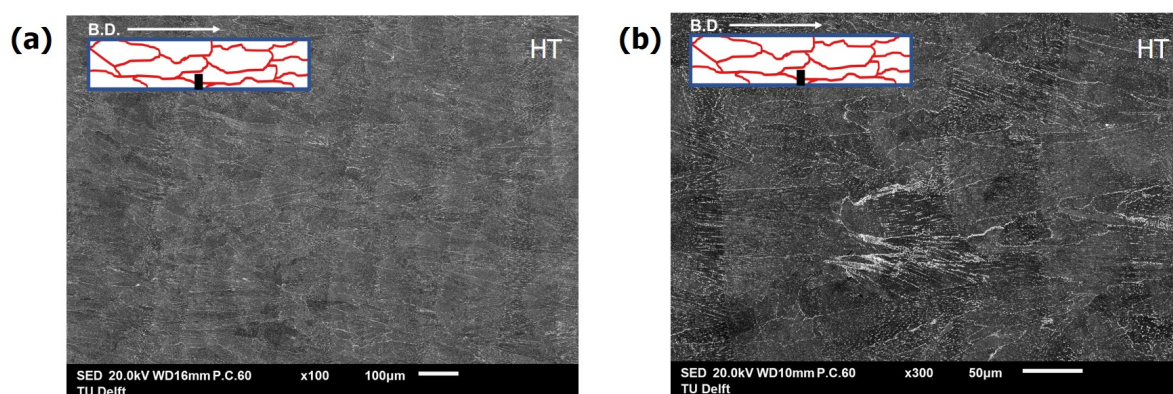


Figure 4.5: SEM micrographs of 950W UG-HT specimens with $BD \perp CD$ at a magnification of (a) 150X and (b) 300X.

The optical micrographs of *UG-HT* specimen with $BD \parallel CD$ can be seen in Figure 4.6. Unlike in $BD \perp CD$, the γ dendrites can be clearly seen in the optical micrographs. While the most identifiable dendrites are ones stretched along the BD however, columnar grains with dendrites inclined at an angle to the BD can also be seen here. These can be seen distinctively in electron micrographs from Figures 4.7 (a) and (b). The microstructure is largely similar the one with $BD \perp CD$ with the only apparent change being the BD. This validates the choice of symbols used for respective BD shown in Figure 3.2.

Fine grained microstructure produced with 250 W laser power: Figure 4.8 shows the optical micrographs of UG-HT specimen produced with a 250 W laser power. As was consistently discussed in section 2.3.2 and in the previous studies

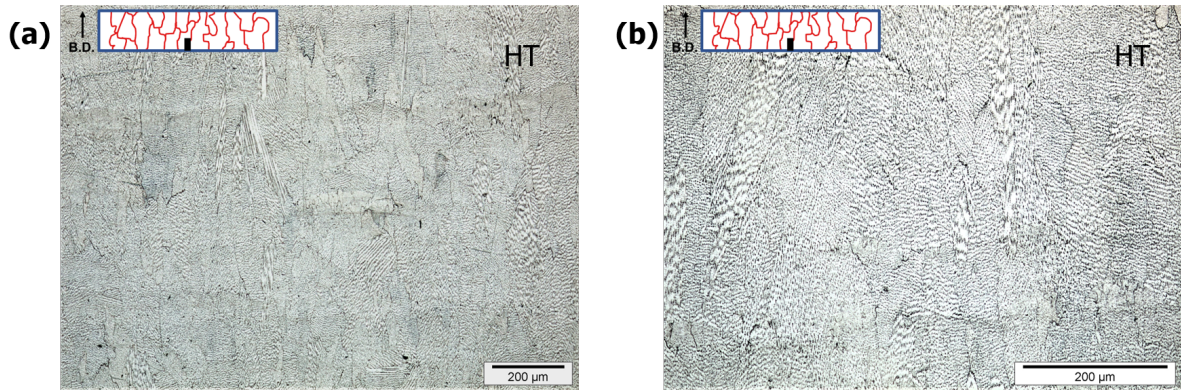


Figure 4.6: Optical micrographs of 950W UG-HT specimens with BD || CD at a magnification of (a) 5X and (b) 10X.

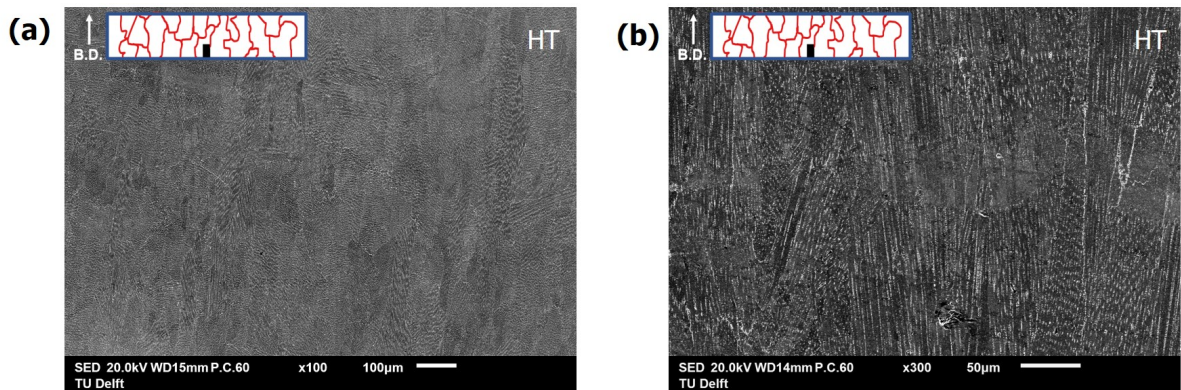


Figure 4.7: SEM micrographs of 950W UG-HT specimens with BD || CD at a magnification of (a) 150X and (b) 300X.

involving the usage of a lower laser power [30, 31, 32], the grain structure for 250W specimen is of equiaxed nature and on comparison with 950W specimens is comparatively finer. The difference becomes even more apparent when comparing the electron micrographs from Figures 4.9 (a) and (b) with the previous findings. The main reason associated with the such and equiaxed nature of the grains in these specimens is the low heat input resulting in the columnar grain growth confined to the individual melt pools. This low heat input also results in a significantly lower thermal gradients than in the case of 950W specimens allowing a dendritic growth in random orientations as opposed to primarily along BD in previous cases. However, closely observing Figures 4.9 (a) and (b) confirms that there are a few outliers that grow as elongated columnar grains. This sheds more light on why it is difficult to predict and generalise the local heat flow during SLM processing.

Hot isostatic pressed and heat treated

It is reported that the HIPing process which involves high pressures and temperatures, alters the as-printed microstructures in AM components [17, 1, 27]. The same is observed in the microscopy of *HIPHT* in this study. It can be seen from optical micrographs in Figures 4.10 (a) and (b), that microstructures for both 250W and 950W show no resemblance with the *AP* and *HT* specimens. The melt-pool

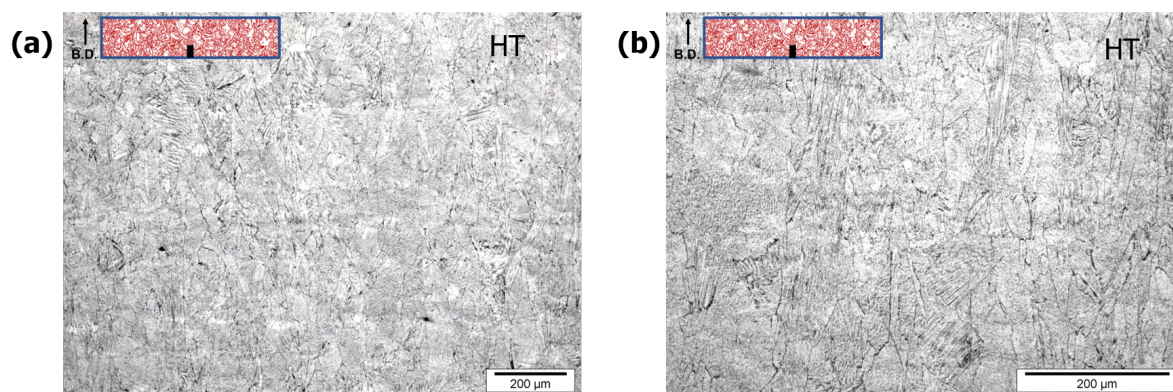


Figure 4.8: Optical micrographs of 250W UG-HT specimens at a magnification of (a) 5X and (b) 10X.

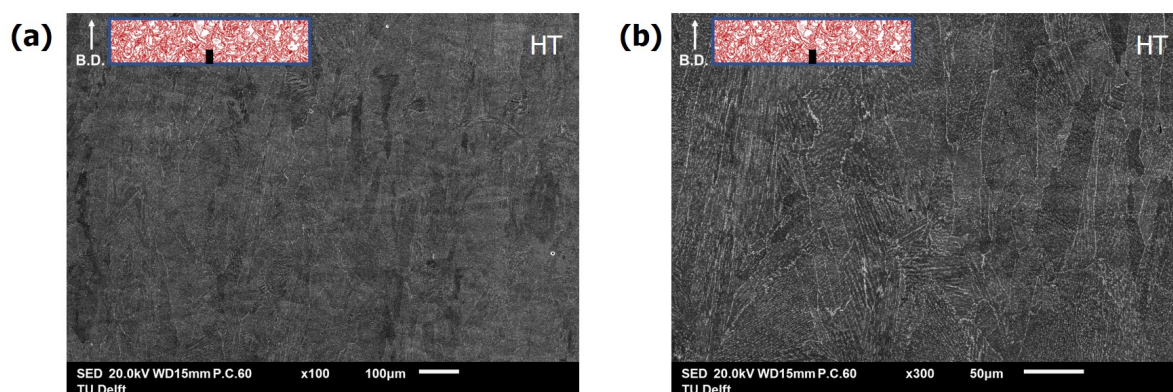


Figure 4.9: SEM micrographs of 250W UG-HT specimens at a magnification of (a) 150X and (b) 300X.

tracks, layers, columnar grains and the γ dendrites have all been completely erased. The fine grain structure is equiaxed while the coarse grain structure is a mixture of elongated (along BD) polyhedral and equiaxial grains. In addition, HIPing has also introduced an enormous amounts of twin boundaries in either microstructures. This is again because of the high pressures involved. SEM micrographs for the *HIPHT* specimens can be seen in Figures 4.11. The story remains the same for these micrographs as well.

Precipitate evolution after heat treatments

To have a better understanding of the bright lines running around the dendrites and grain boundaries in the microstructures shown in Figure 4.17, micrographs at a higher magnification of 600X were acquired. These micrographs shown in Figure 4.12 reveal an array of precipitates forming the bright regions seen previously. It is expected to see such an effect because of the homogenisation heat treatment followed by aging. The inset shows a closer look into the morphology of these precipitates with identification of a mixture of rod-like and globular precipitates. A few blocky precipitates are also distinguished from the background. From the literature, these rod-like precipitates are the δ phases while the blocky precipitates are carbides. EDS confirms this hypothesis with stronger Nb and Ni peaks for the precipitates than the background. A clear contrast is seen between the location of these precipitates in Figure 4.12. The precipitates appear to be concentrated higher

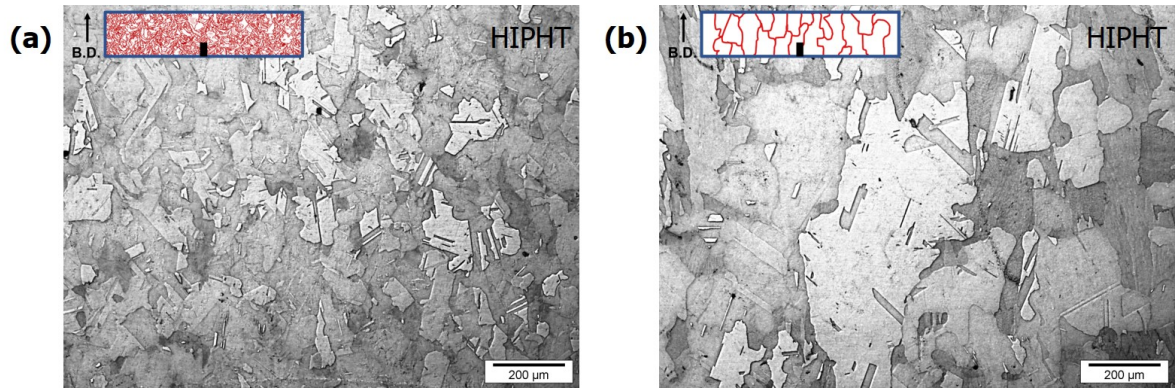


Figure 4.10: Optical micrographs of (a) 250W HIPHT specimen and (a) 950W HIPHT specimen with $BD \parallel CD$.

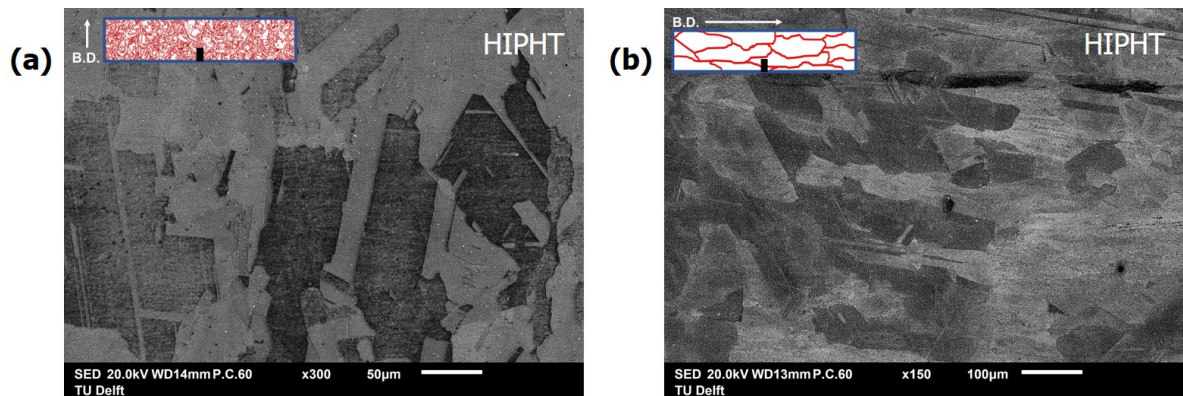


Figure 4.11: Optical micrographs of (a) 250W HIPHT specimen and (a) 950W HIPHT specimen with $BD \perp CD$.

along the the dendrites in 950W specimen than in 250W specimen. While for 250W, the grain boundaries are entirely filled with these precipitates. Higher magnification SEM micrographs are provided in Figure 4.13. Further, the resolution of microscope used is insufficient to identify the presence of γ' and γ'' as well as the Laves phases. With the help of XRD, an attempt to put the complete picture into perspective is made in the next section.

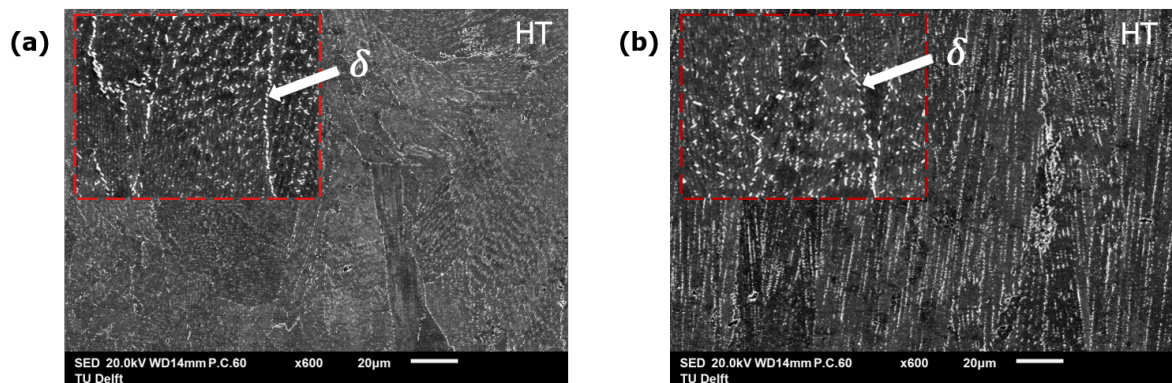


Figure 4.12: SEM micrographs showing rod like and globular precipitates in (a) UG-HT 250 W specimen and (b) UG-HT 950 W specimen with $BD \parallel CD$. Insets show respective magnified SEM micrographs, both at 2000X magnification.

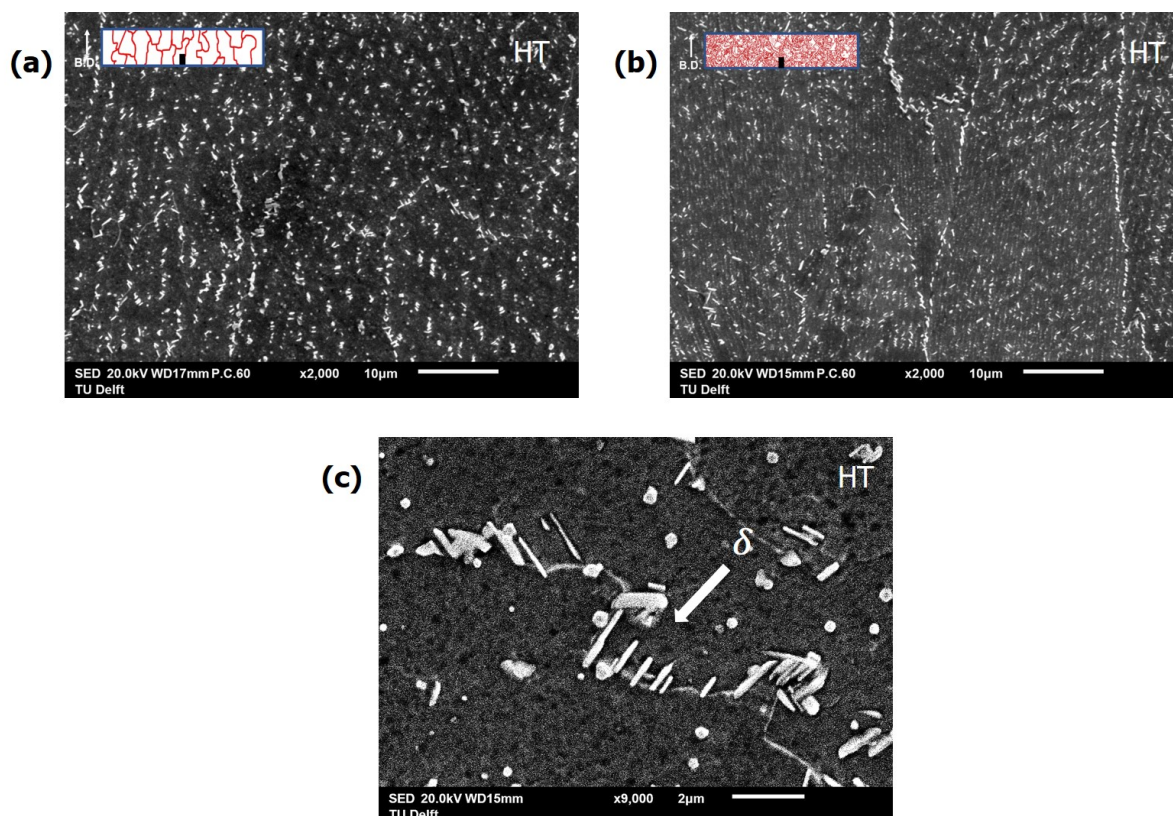


Figure 4.13: SEM micrographs showing a cluster of rod like and globular δ precipitates in heat treated specimen (a) 950W with BD \parallel CD in interdendritic spaces, (b) 250W primarily in grain boundaries but also interdendritic spaces, (c) 9000X magnification.

HIPing involved in *HIPHT* is expected to segregate the MC type of carbides at the grain boundaries. Due to the increased size of the MC carbides as compared to the as-printed condition, a subsequent homogenisation treatment coarsens these carbides instead of dissolving them [61]. The same is reported here from the SEM micrographs of the *HIPHT* specimens. Figures 4.14 both show the SEM micrographs of *HIPHT* specimens. It is seen that the carbides specifically precipitate along the grain boundaries. This is even more true for the graded specimens shown here.

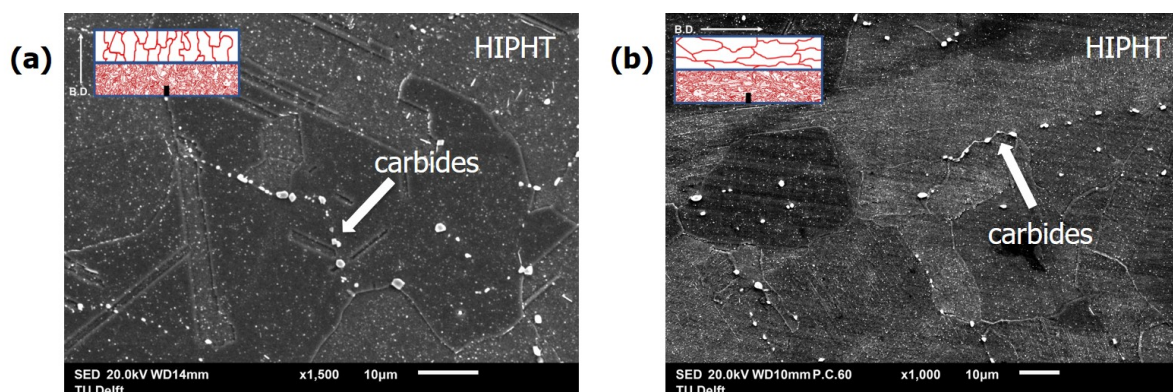


Figure 4.14: SEM micrographs showing blocky MC carbides along the grain boundaries in (a) 950W side of G-HT specimen with BD \parallel CD and (b) 950W side of G-HT specimen with BD \perp CD.

X-ray diffraction characterization: The main goal of obtaining the x-ray diffraction (XRD) measurements in this study is to identify the phases formed with the progression of post-processing heat treatments. To perform XRD analysis, a representative 950W UG specimen with BD || CD was selected for the coarse grain microstructure in their respective conditions while as has been the story, 250W specimen represents the fine grain microstructure. Figures 4.15 (a) and (b) show the results for 250W and 950W specimen respectively in all the three conditions - *AP*, *HT* and *HIPHT*.

The NbC and TiC peaks are consistently observed in *AP*, *HT* as well as *HIPHT*. Hence, it is safe to assume that the temperatures involved in these post-process heat treatments are not high enough to dissolve these carbides. Also, TiC is observed only in the coarse grain microstructure produced by 950 W laser power while NbC is observed in all the specimens. This argument is valid for all the conditions. The reason behind presence of TiC in only the 950W specimens could be associated with the available driving force for their precipitation due to higher heat flux. Elsewhere, the peaks corresponding to the Laves phases seen in *AP* specimens are neither identified in *HT* specimens nor *HIPHT*.

The γ phase produces strongest peaks at 2θ values of around 50° , 60° and 90° in all the specimens. However, one of the γ peaks at a 2θ value of around 50° is not obtained in the 950W *HT* specimen. A clear indication of the absence of the representative $\langle 111 \rangle$ grain orientations corresponding to this 2θ value. This argument will be further validated in section 4.3 when the EBSD scans with the inverse pole figure maps will be discussed for all the conditions. Similarly, the γ peaks at a 2θ value of around 90° are strongest for *HIPHT* while they are substantially weak in both *AP* and *HT*. These peaks correspond to the $\langle 101 \rangle$ orientations. Measurements for *HT* specimens were repeated to make sure that the missing peak at $\langle 111 \rangle$ orientations isn't an one off error but the final result. The reason for such results could very well be imbibed in the grain transformations occurring due to heat treatments. Providing a full-proof explanation seems difficult due to the lack of similar XRD measurements for homogenised and aged Inconel 718 processed via AM. However, Fayed et. al. [62] recently reported XRD measurements for IN718 post-processed with a similar triple stage heat treatment - homogenisation + solution annealing + double aging. It is observed in this study that indeed for a specific homogenisation hold time (1-2 h), the peaks for $\langle 111 \rangle$ as well as $\langle 101 \rangle$ are seen to be shortening at the end of whole set of heat treatments. Here as well, the authors of this study have stipulated the recrystallization characteristics of IN718 in the temperature range of around 1080°C to cause the observed behavior. It would be interesting to evaluate in detail the grain evolution in IN718 fabricated with lower and higher laser powers in the follow-up studies.

Another interesting detail to note here in *HT*, are the extra peaks for δ phase which are not seen in *AP* and *HIPHT* specimen (at a 2θ value of around 54°). Thus, the presence of δ phase is in line with the rod-like precipitates observed in microscopy. It is expected that γ' and γ'' strengthening phases are also formed after the aging treatment involved in *HT* procedure but given that most of their peaks overlap with γ phase, it is difficult to pinpoint their presence in *HT* specimens. However, substantial evidence of their presence is accrued in *HIPHT* specimens.

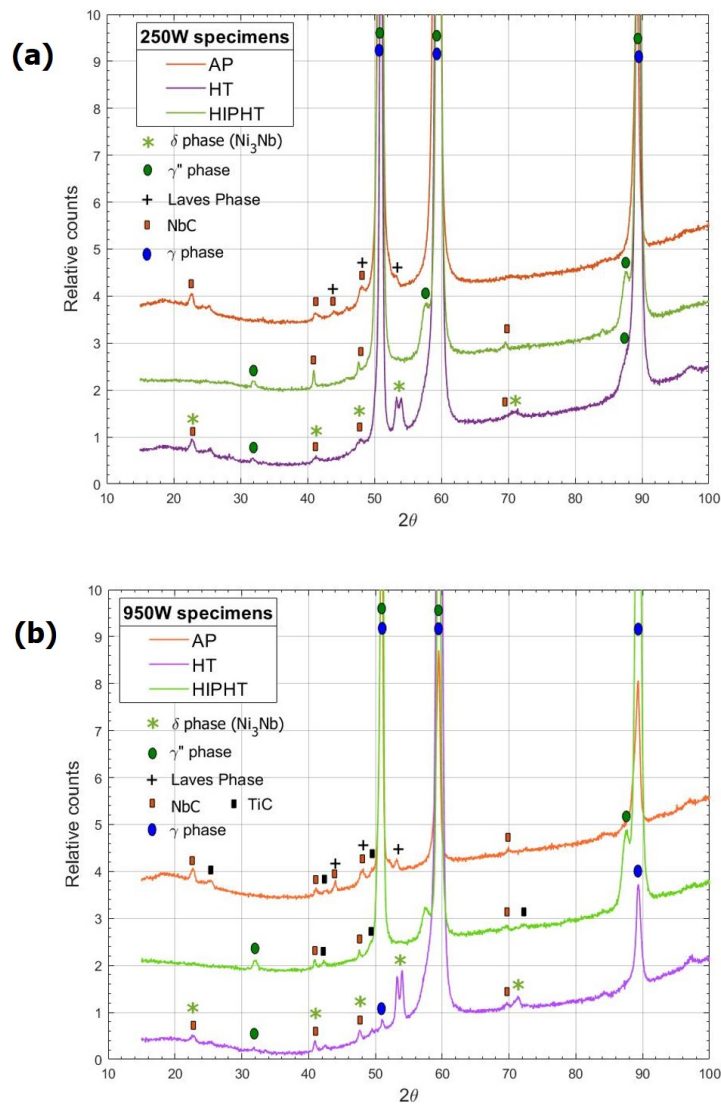


Figure 4.15: XRD plots for UG specimens produced using (a) 250 W laser power, and (b) 950 W laser power.

4.1.3. Micro-hardness measurements

All the micro-hardness measurements are summarised in Table 4.1. In each of the processing conditions - *AP*, *HT* and *HIPHT*, fine grain microstructures produced with 250 W laser power are seen to possess a higher hardness values than their coarse grain counterparts produced using the 950 W laser power. It is well documented in literature that the fine grains have a higher yield strength according to the hall-petch relation ($\sigma_y = \sigma_0 + kd^{-1/2}$) where the yield strength (σ_y) is linked inversely with the grain size (d). Hardness being considered as a direct indicator of the yield strength, fine grain having a higher hardness is nothing but natural. *AP* specimens have the lowest HV_1 values. This may be primarily attributed to the presence of pores and brittle Laves phases in *AP* condition aiding to the easier indentation. Higher hardness in *HIPHT* specimens could be an effect of reduction in pores, absence of

brittle Laves phases and precipitation of strengthening γ'/γ'' phases after aging. The highest values are observed in *HT* samples. This could be because of the precipitation of extra δ phases after the homogenisation treatment. Another reason could be the reduced amount of segregated carbides as compared to *HIPHT* specimens.

Table 4.1: Summary of micro-hardness measurements of ungraded specimens.

Processing Condition	Laser Power / Grains	Specimen	Hardness Measurements (HV ₁)
As - printed (AP)	950 W / Coarse	BD \perp CD	303 \pm 10
	950 W / Coarse	BD \parallel CD	341 \pm 9
	250 W / Fine	-	373 \pm 11
Heat treated (HT)	950 W / Coarse	BD \perp CD	513 \pm 7
	950 W / Coarse	BD \parallel CD	522 \pm 5
	250 W / Fine	-	533 \pm 21
Hot isotactic pressed +	950 W / Coarse	BD \perp CD	490 \pm 8
	950 W / Coarse	BD \parallel CD	501 \pm 7
Heat treated (HIPHT)	250 W / Fine	-	505 \pm 10
HT wrought	-	-	501 \pm 10

4.1.4. Interfaces in graded microstructure

Figure 4.16 shows the electron micrographs of interfaces in G-AP specimens. In case of BD \parallel CD, the interface is singled out on the basis of difference in the size of melt-pools in 250W region (deeper and narrower) and 950W (shallower). This interface can also be identified from the region of overlap of the melt-pools. Identification of interface in case of BD \perp CD is straightforward with the melt-pools forming a distinct region of overlap leading to a mishmash of the melt-pools due to the adjacent scanning using two different laser powers - 950W and 250W.

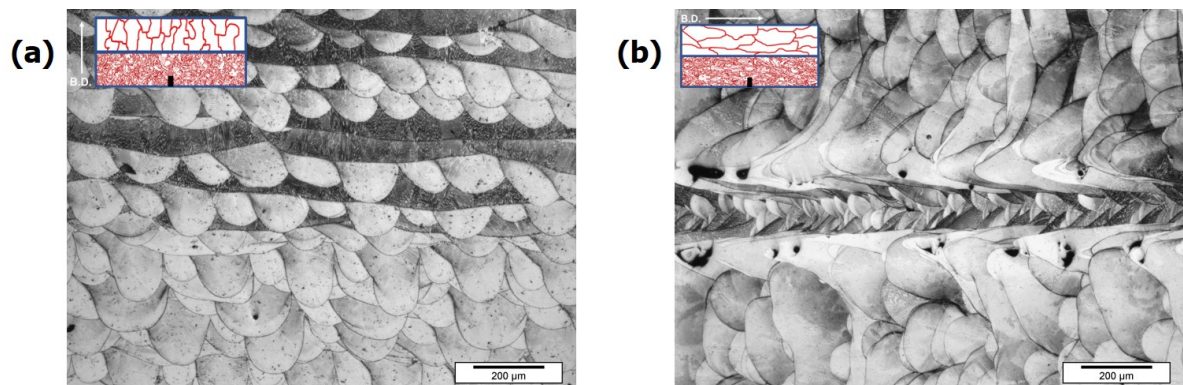


Figure 4.16: Interfaces in G-AP specimens with (a) BD \parallel CD and (b) BD \perp CD.

Figure 4.17 (a) shows an electron micrograph of the interface in G-HT specimen with $BD \perp CD$. At the interface, a weave like mishmash pattern can be seen as the dendrites from 950W coarse grain and 250W fine grain microstructure extend into the transition zone in the interface. At the interface are also seen the black spots as shown in Figure 4.17 (b). On initial observation, these look like the porosity however an appropriate reasoning will be provided in section 4.4 to determine what these features are. Figure 4.17 (b) on the other hand shows an electron graph for G-HT specimen with $BD \parallel CD$. Here, the interface is mainly distinguished on the basis of the appearance of the grains and the inherent γ dendrites. For 950W coarse grain, they are primarily orientated along the BD as can be clearly seen while the equiaxed nature of the 250W fine grains can be easily distinguished for these specimens. The oriented dendrites from coarse grain regions are seen to be extended into the fine grain region introducing a transition region at the interface in this case as well. Hence for both G-HT specimen with $BD \perp CD$ and $BD \parallel CD$, there is clear distinction between the 950W and 250W regions with the similar features from the corresponding individual microstructures in UG-HT specimen. The interface is seen to depict a mishmash of these regions. A look back at the interfaces in AP specimens shows that the grading generated in AP condition is retained after the post-processing homogenisation and aging steps involved to obtain the HT specimens.

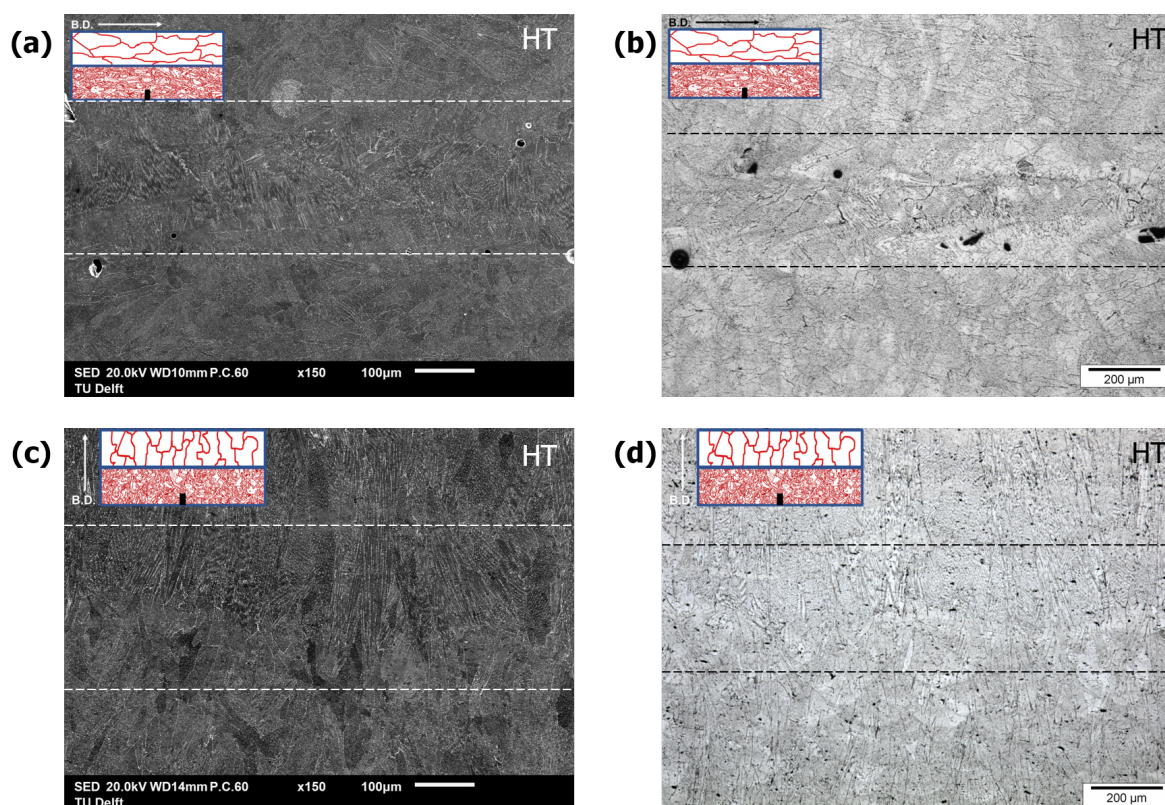


Figure 4.17: (a), (c) SEM micrographs and (b), (d) Optical micrographs of the interface region in Graded (G) specimens.

The extensive changes in the microstructure due to HIPing also removes any gradient in microstructure across the interfaces in *G-HIPHT* specimens. The *HIPHT*

are also marked with the formation of twins as a result of pressurised pressing stage. The irregularly shaped columnar grains from *AP* and *HT* are transformed into polyhedral grains with no dendrites within these grains as was reported earlier. These interfaces without any hint of grading left behind can be seen in Figures 4.18.

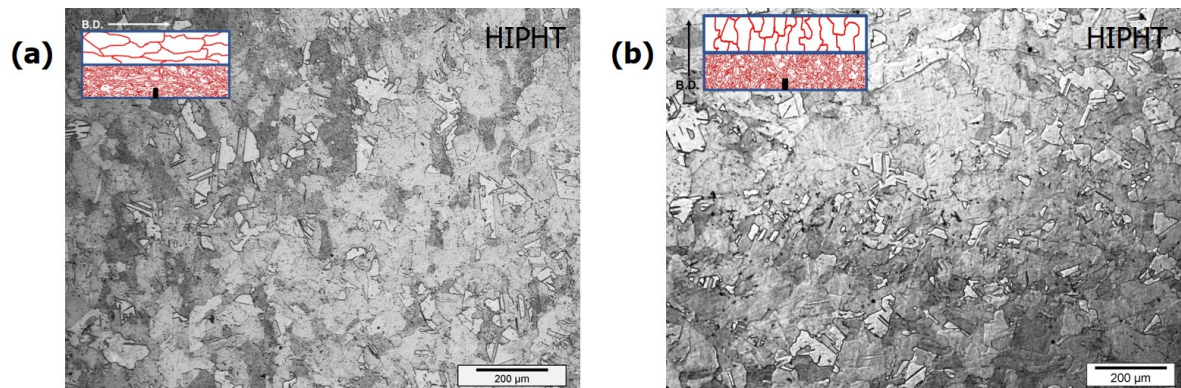


Figure 4.18: Interface region in Graded (G) specimens from HIPHT conditions with (a) $BD \perp CD$ and (b) $BD \parallel CD$.

4.1.5. Summary

1. As-printed

- Melt-pools formed during the SLM process were the first features to be characterized in all the *AP* specimens.
- The 950 W laser power produced a coarse grain microstructure. These grains have a columnar morphology, were elongated along BD and spanned across several melt-pools. The γ dendrites were seen to be elongated along the direction of elongated columnar grains which in this case is also the BD.
- The 250 W laser power produced an equiaxed fine grain structure compared to the previous case. These grains were randomly oriented and their growth was restricted to individual melt-pool.
- BD had a direct influence on the grain orientations for the specimens produced with 950 W laser power. Columnar grains and the inherent γ dendrites were both oriented along the BD in case of $BD \perp CD$ as well as $BD \parallel CD$.

2. Heat treated

- The presence of melt-pools was mostly removed as a result of the homogenisation post-processing heat treatment used. The layers on the other hand could still be identified.
- The grains structure remained the same as that in *AP* specimens with the relation between laser powers, BD and grain characteristics unchanged.
- Additional features such as the δ precipitates and carbides were observed to be precipitated along the grain boundaries and γ dendrites.

3. Hot isostatic pressed and heat treated

- Melt-pools and γ dendrites were entirely erased. Polyhedral grains were formed accompanied by twin formation and are attributed to the high pressure and temperature during HIPing.
- A small amount of columnar grains on the 950W side are also sighted as are the equiaxed grains on 250W side, but these grains are sharper than the ones in *AP* and *HT*.

4. X-ray diffraction

- Peaks for γ phases and NbC are observed in all the conditions - *AP*, *HT* and *HIPHT*.
- TiC is identified only in the 950W specimens. Laves phases are identified in *AP* specimens while δ phases in *HT* specimens.
- It is expected that the presence of γ' and γ'' phases in *HT* and *HIPHT* specimens is also confirmed through XRD however, their peaks overlap with γ peaks.

5. Micro-hardness measurements

- Fine grains had the highest hardness values in all the processing conditions. For the same category of specimen, the hardness values are in the order $HT > HIPHT > AP$. Presence of strengthening phases, lack of brittle Laves phases and reduced porosity (specifically in *HIPHT*) are few reasons outlined for the observed trend.

6. Interfaces in graded specimens

- Interfaces in *AP* specimens are mainly identified by the melt-pools. In the case of $BD \parallel CD$ interface is determined by the difference in the size of melt-pools from 950W region and 250W region. While in the case of $BD \perp CD$ it is the region of mishmash between the melt-pools from 250W and 950W regions.
- For the *HT* specimen with $BD \perp CD$, the region of mishmash in interface is retained after heat treatment. Interface in specimen with $BD \parallel CD$ is identified on the basis of grain size and orientation difference in these regions; with grains in 950W region coarser and orientated along BD and grains 250W region finer and randomly orientated. The same is also applicable to $BD \perp CD$ outside the region of mishmash.
- There is no concept of grading and interfacial region remaining in either of the *HIPHT* specimens because of the extensive microstructural transformation following the high pressure and temperatures during HIPing.

4.2. Fatigue Crack Propagation Behavior

The contents of this section deal with separate characterization of the fatigue crack propagation behavior in ungraded (UG) as well as graded (G) specimens. Main focus of obtaining the results in this section was on *HT* specimens as a continuation from a previous study by Sahu et. al. [12]. A proper comparison with the *AP* and *HIPHT* specimens is provided wherever necessary.

4.2.1. Fatigue characterization of ungraded specimens

Constant K_{\max} tests

Constant K_{\max} tests were primarily performed to estimate ΔK_{th} values. Table 4.2 summarises the variation of ΔK_{th} with respect to the grain size, grain orientation and post-processing conditions. Although, it is important to note that the data is represented by a single set of test and hence is not sufficient to draw a concrete conclusion. On other hand, a good understanding about the overall trend can definitely be obtained.

Effect of laser power: 950W *HIPHT* specimens have the highest values of ΔK_{th} . These values are higher than the 250W *HIPHT* specimen. This asserts that the coarse grain microstructure performs better than the fine grain in *HIPHT* condition. Such a behavior is in line with the general trend in conventionally produced metals. The grain boundaries act as a barrier to the dislocation motion and slip transmission leading to local stress concentrations which activate the slip systems in subsequent grains, thus increasing the effective ΔK [63, 64]. *HIPHT* is primarily performed to reduce the porosity and homogenise the microstructure. However, HIPing also completely erases the melt pools, columnar grains as well as the γ dendrites. This can very well explain the opposite trends in *AP* and *HT* specimens where the 250W specimens have higher ΔK_{th} value than both 950W specimens. In such cases, the grain boundaries will act in an opposite manner and aid to the dislocation motion and a subsequent tortuous crack will decrease the effective crack growth. This can be associated with the difference in grain morphologies and texture - randomly oriented near equiaxed in the former and textured elongated in the latter.

Effect of BD: In *AP* specimens, grains have an inherently lower strength as compared to *HT* and *HIPHT* specimens. So in such cases, grain boundaries play an important role by introducing differently oriented less favorable slip systems and thus increase the resistance to short crack growth [63]. This is the same case in *AP* specimen with $BD \perp CD$ where grains are oriented perpendicular to crack path introducing more grain boundaries. However, in precipitation strengthened grains and grain boundaries of *HT* and *HIPHT*, this does not seem to work out the same way.

Effect of post-process heat treatments: When comparing the *AP* and *HT* specimens, *HT* specimens have a higher ΔK_{th} value than their counterparts from *AP*. This is natural since the aging treatment from *HT* procedure introduces the

strengthening phases which lead to the crack arrest or deflection in initial stages of a short crack propagation. Also, as seen from XRD, the brittle phases Laves phases from *AP* condition are not observed in *HT* specimens, which can further improve the fatigue behavior under ΔK_{th} conditions.

Table 4.2: Summary of constant K_{max} tests with the corresponding threshold values.

Processing Condition	Laser Power / Grains	Specimen	ΔK_{th} (in $MPa \cdot m^{0.5}$)	R (stress ratio)
As Printed (AP)	950 W / Coarse	BD \perp CD	7.0 ± 0.3	0.7
	950 W / Coarse	BD \parallel CD	6.0 ± 0.2	0.7
	250 W / Fine		7.2 ± 0.3	0.7
Heat Treated (HT)	950 W / Coarse	BD \perp CD	7.5 ± 0.3	0.7
	950 W / Coarse	BD \parallel CD	7.9 ± 0.2	0.7
	250 W / Fine		9.5 ± 0.2	0.7
Hot Isostatic Pressed + Heat Treated (HIPHT)	950 W / Coarse	BD \perp CD	8.8 ± 0.2	0.7
	950 W / Coarse	BD \parallel CD	10.2 ± 0.2	0.6
	250 W / Fine		7.7 ± 0.3	0.7
HT Wrought	-		13.1 ± 0.9	0.6

Constant load amplitude tests

Figures 4.19 (a), (b) and (c) show the processed curves for *HT* specimens obtained from the Matlab algorithm mentioned in appendix 6.2. The generated data points for da/dn are plotted in these curves as a function of ΔK values. All the curves also contain their respective fitting lines from power law equation ($da/dn = C(\Delta K)^m$, where C is Paris Constant and m is Paris Exponent) in the Paris region. A summary of the these fitted lines is provided in Figure 4.20 (b). For comparison, the summary of fitting lines for all the specimens in *AP* and *HIPHT* conditions are reproduced in Figures 4.20 (a) and (b). These summarised results show a distinction between the positioning of the fitting lines in *AP*, *HT* as well as *HIPHT* specimens. Emphasized here is the dependence of fatigue behavior on the inherent microstructures produced, which will be touched upon shortly. As an aid for performing the quantitative analysis to mark out this distinction seen in the fitting curves, the Paris exponent (m) and Paris constant (C) are summarised in Table 4.3. The main principle behind pointing them out is that lower the C and m values, better are the fatigue properties of these specimens. However, this is still difficult to interpret in terms of the performance. Which is why crack growth rates are calculated from these C and m values at two ΔK values $16.5 MPa\sqrt{m}$ and $22.5 MPa\sqrt{m}$ (summarised in Table 4.4), hereon called as lower and higher ΔK respectively.

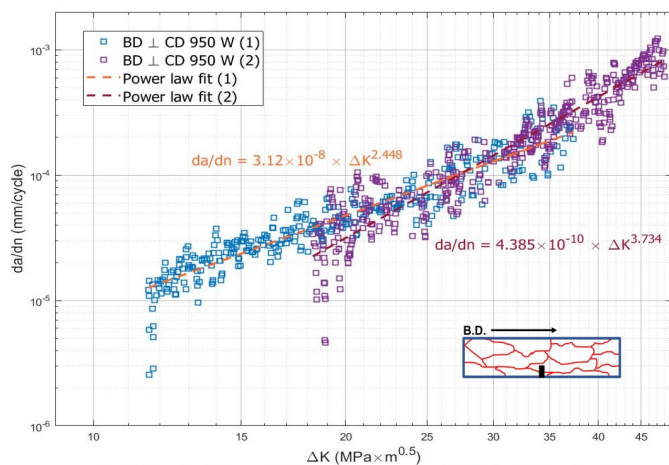
Effect of laser power: It appears that the fine grain microstructure produced using 250 W laser power has the lowest da/dn values in all the conditions - *AP*, *HT* and *HIPHT*. This is in comparison with their respective coarse grain microstructure counterparts (BD \perp CD and BD \parallel CD) produced using 950 W laser power. A lower da/dn indicates towards the better performance of fine grain microstructure in all the conditions, at lower as well as higher ΔK values. A detailed study of the fracture

surfaces (for graded specimens at later in section 4.4 will help shed more light on the lower values obtained for 250W specimens.

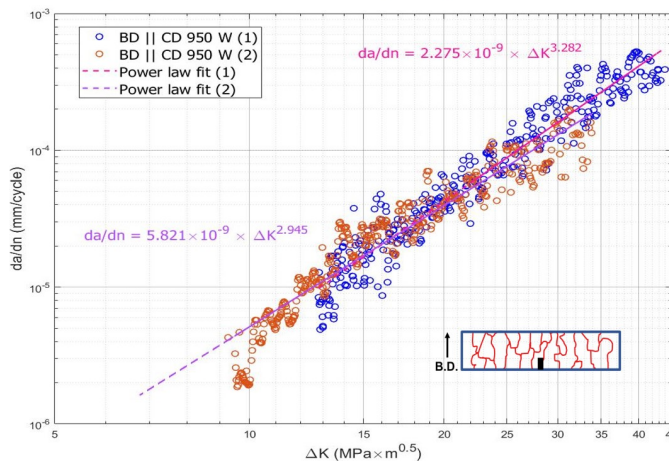
Effect of BD: No general trend is visible such as the one pointed out for laser powers is seen with regards to the effect of BD. The lowest da/dn values in *AP* condition is observed for $BD \parallel CD$. This is natural since a grain structure elongated in a direction perpendicular to the crack path, even if coarse will in hindsight act as a fine grain structure and deflect the crack front at the grain boundaries. Such an increased number of encounters with the grain boundaries is significant especially at the high angle grain boundaries which in turn changes the spatial arrangement of the slip planes with respect to the local crack path direction [63, 65]. An opposite trend is observed in case of *HT* and *HIPHT* specimens. This can be explained with the help of additional precipitates characterized in these specimens. It was discussed in section 4.1.2 that the γ'/γ'' and δ phases are formed in *HT* specimens. It was observed that their precipitation was preferentially along the dendrites inside columnar grains for the 950W specimens. Elsewhere, they are also observed at the grain boundaries. Depending on the size of these precipitates, it can substantially change how the dislocation motion interacts with these precipitates and the grain boundaries. It is important to note that homogenisation heat treatment also promotes recrystallization, the quantitative analysis of which is outside the scope of this study. An explanation for the lower da/dn values for $BD \parallel CD$ in *HT* specimens could be associated with a combination of all the reasons mentioned. The difference is insignificant in *HIPHT* and a reasonable cause is again derived in the effect that the HIPing has on their microstructures. Further explanation is provided below.

Effect of post-process heat treatments: *AP* specimens show a significant deviation between their values. This could be a result of the heterogeneity arising from the cellular grain structure coupled with high amount of pores and presence of brittle Laves phases in the as-printed condition. On the other hand, both the post-processing heat treatments are seen to diminish this deviation between the samples. This is also evident from the summarised fitted curves for *HT* - Figure 4.20 (b) and *HIPHT* - Figure 4.20 (c). The curves for these specimens are closely packed more than the ones for *AP* - Figure 4.20 (a), where there is a large scatter observed. This hints towards a possible homogenisation of fatigue properties in the individual microstructures of the *UG* specimens after post-processing heat treatments. For *HIPHT* specimens, this is a direct consequence of the drastic changes that the HIPing induces in these microstructures. Both the coarse grain - 950W and fine grain - 250W microstructures were associated with extensive grain coarsening, re-crystallization and combination. This lead to a little to no variation between their microstructures, the effect of which probably trickles down into the da/dn values observed for *HIPHT* specimens. On the other hand, no such significant changes in microstructure are observed for the *HT*, yet the variation in properties between the individual microstructures is seen to be diminishing here as well. This could be explained by another microstructural feature noticed in these specimens. The homogenisation heat treatment as the name suggests removes any local segregations while the subsequent aging treatments involved introduce the

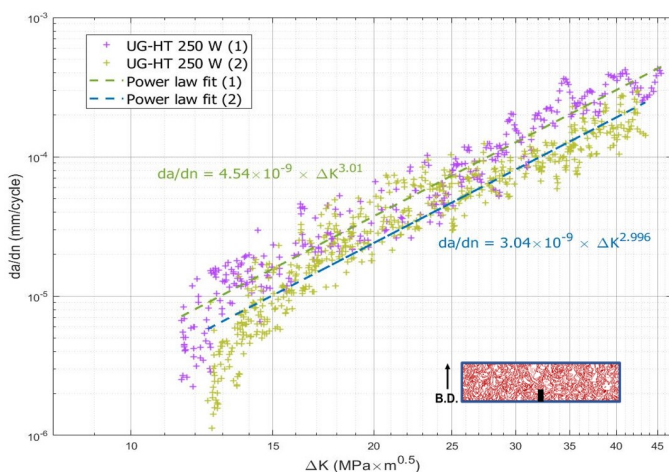
strengthening phases. This may have in turn reduced the effect of grain sizes and orientations in the *UG-HT* specimens. A similar concept was discussed by Suk et. al. [66] by studying the strain localisation characteristics in as-printed and post-process heat-treated IN718.



(a) Test data – HT coarse grain (950 W) BD ⊥ CD

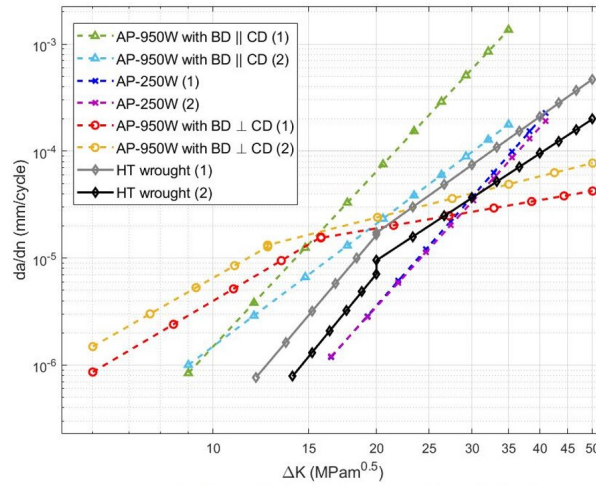


(b) Test data – HT coarse grain (950 W) BD || CD

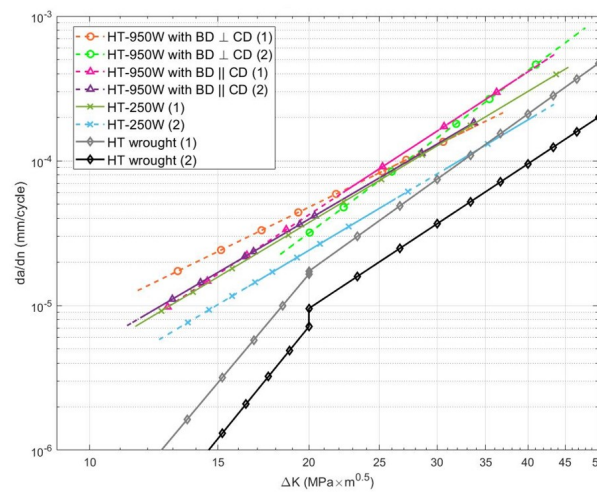


(c) Test data – HT fine grain (250 W)

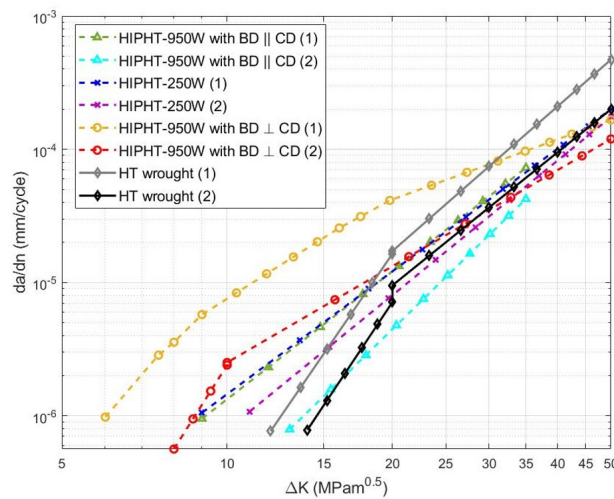
Figure 4.19: (a), (b), (c) - da/dn v/s ΔK plots showing the fatigue curves of ungraded specimens in heat treated (HT) condition.



(a) Summary of Paris law fit data for as-printed (AP) specimens



(b) Summary of Paris law fit data for heat treated (HT) specimens



(c) Summary of Paris law fit data for hot isotactic pressed + heat treated (HIPHT) specimens

Figure 4.20: (d), (e), (f) - Summary of power law fitted curves in the Paris regions for AP, HT and HIPHT specimens respectively, showing the effect of grain size and orientation on crack growth rate in Paris region (also shown here are the HT wrought IN718 specimens for reference).

Table 4.3: Combined summary of Paris fit data showing the Paris constants and exponents.

Processing Condition	Laser Power / Grains	Specimen	Paris Exponent (m)	Paris Constant (C)
As Printed (AP)	950 W / Coarse	BD \perp CD	m1 = 3.0 ± 0.1 m2 = 1.1 ± 0.2	C1 = $6.0 \times 10^{-9} \pm 2.3 \times 10^{-9}$ C2 = $9.4 \times 10^{-7} \pm 4.3 \times 10^{-7}$
	950 W / Coarse	BD \parallel CD	4.6 ± 0.8	$1.2 \times 10^{-10} \pm 1.1 \times 10^{-10}$
	250 W / Fine	-	5.7 ± 0.1	$1.6 \times 10^{-13} \pm 0.5 \times 10^{-13}$
Heat Treated (HT)	950 W / Coarse	BD \perp CD	3.1 ± 0.1	$1.6 \times 10^{-8} \pm 1.1 \times 10^{-8}$
	950 W / Coarse	BD \parallel CD	3.1 ± 0.1	$4.1 \times 10^{-9} \pm 2.3 \times 10^{-9}$
	250 W / Fine	-	3.0 ± 0.1	$3.8 \times 10^{-9} \pm 1.2 \times 10^{-9}$
Hot Isotactic Pressed + Heat Treated (HIPHT)	950 W / Coarse	BD \perp CD	m1 = 5.7 ± 0.9 m2 = 2.5 ± 0.1	C1 = $9.0 \times 10^{-11} \pm 9.0 \times 10^{-11}$ C2 = $1.5 \times 10^{-8} \pm 0.5 \times 10^{-8}$
	950 W / Coarse	BD \parallel CD	3.6 ± 0.4	$4.4 \times 10^{-10} \pm 4.2 \times 10^{-10}$
	250 W / Fine	-	3.2 ± 0.2	$8.1 \times 10^{-10} \pm 4.6 \times 10^{-10}$
HT Wrought	-	-	m1 = 6.1 ± 0.1 m2 = 3.5 ± 0.2	C1 = $1.6 \times 10^{-13} \pm 0.8 \times 10^{-13}$ C2 = $3.5 \times 10^{-10} \pm 1.1 \times 10^{-10}$

Table 4.4: Summary of da/dn values at $\Delta K = 16.5 \text{ MPa}\cdot\sqrt{\text{m}}$ and $22.5 \text{ MPa}\cdot\sqrt{\text{m}}$ obtained from fitting curves in Paris region.

Processing Condition	Laser Power / Grains	Specimen	Crack growth rate (da/dn) values in mm/cycle	
			at $\Delta K = 16.5 \text{ MPa}\cdot\text{m}^{0.5}$	at $\Delta K = 22.5 \text{ MPa}\cdot\text{m}^{0.5}$
As - printed (AP)	950 W / Coarse	BD \perp CD	2.0×10^{-5}	2.9×10^{-5}
	950 W / Coarse	BD \parallel CD	4.8×10^{-5}	2.0×10^{-4}
	250 W / Fine	-	1.4×10^{-6}	8.2×10^{-6}
Heat treated (HT)	950 W / Coarse	BD \perp CD	9.5×10^{-5}	2.5×10^{-4}
	950 W / Coarse	BD \parallel CD	2.4×10^{-5}	6.3×10^{-5}
	250 W / Fine	-	1.7×10^{-5}	4.2×10^{-5}
Hot isotactic pressed + Heat treated (HIPHT)	950 W / Coarse	BD \perp CD	1.7×10^{-5}	3.6×10^{-5}
	950 W / Coarse	BD \parallel CD	1.1×10^{-5}	3.3×10^{-5}
	250 W / Fine	-	6.4×10^{-6}	1.8×10^{-5}
HT Wrought	-	-	4.3×10^{-6}	6.4×10^{-6}

4.2.2. Fatigue characterization of graded specimens

FEM modelling results for obtaining K solutions

As discussed in section 3.3.3, to perform the constant ΔK tests, FEM modeling is required to obtain the customized K solutions for the graded specimens used in this study. The main outcome of this model are J integral values at the small boundary around crack tip as mentioned in section 3.3.3. These J integral values are calculated as a function of crack length. With the data obtained for Young's Modulus (E) in Table 3.3, Equation 3.3 can then be used to calculate the K solutions. Figure 4.21 (a) shows the plot for K v/s crack width ratio. For comparison, the values for K in all the conditions (AP, HT and HIPHT) are plotted alongside the K values obtained from standard solution of $f(a/W)$ shown below. It can be clearly seen that the custom K values obtained from the model are different than the standard K solutions, thus reaffirming the need to calculate these K values.

$$f(a/W) = 3 \left(\frac{a}{W}\right)^{1/2} \frac{\left[1.99 - \frac{a}{W} \left(1 - \left(\frac{a}{W}\right)\right) \left\{2.15 - 3.93 \left(\frac{a}{W}\right) + 2.7 \left(\frac{a}{W}\right)^2\right\}\right]}{2 \left(1 + 2 \left(\frac{a}{W}\right)\right) \left(1 - \left(\frac{a}{W}\right)\right)^{3/2}} \quad (4.1)$$

Figure 4.21 (b) shows the fitted curves for the non-dimensional part $f(a/W)$ in a form similar to that of standard solution. The dimensional part $\frac{P.S}{B.W^{3/2}}$ will remain same in the equations required to calculate these customised K solutions.

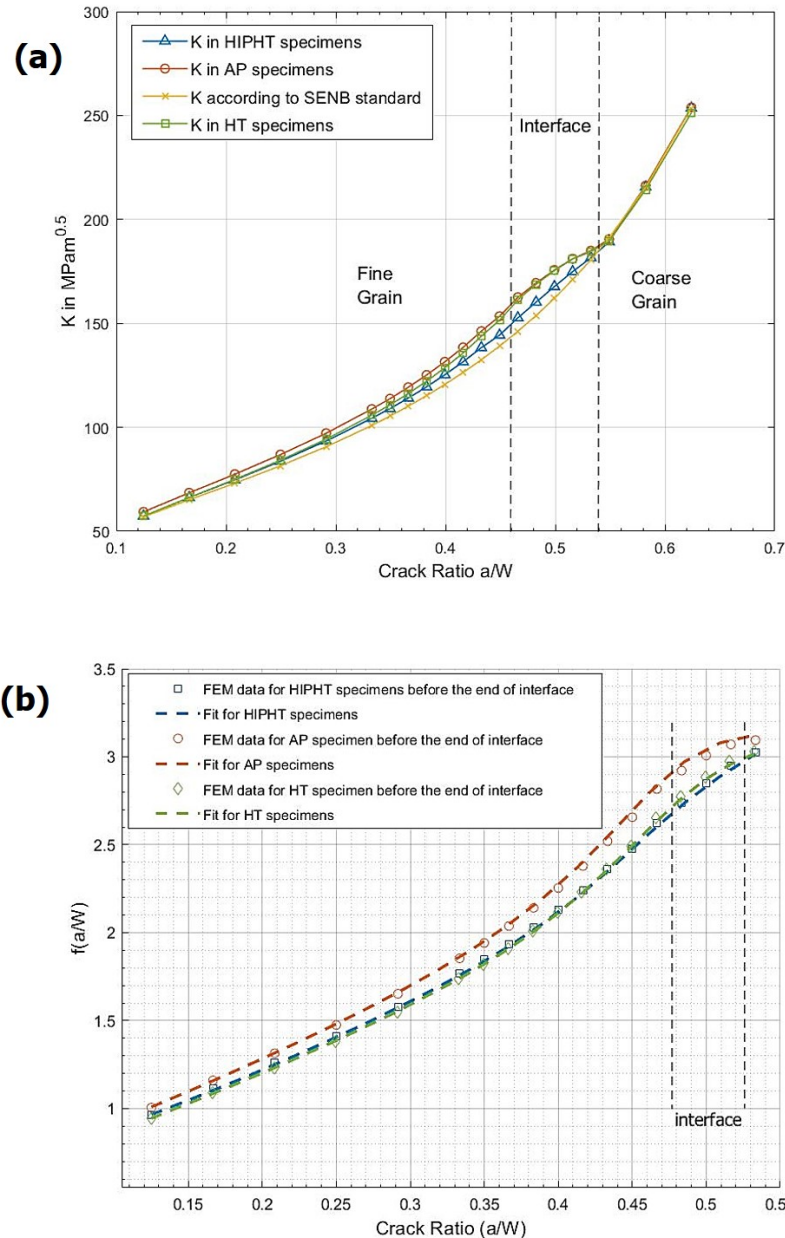


Figure 4.21: (a) K solutions obtained by modeling J integral, (b) Fit for the non dimensional $f(a/W)$ part of the K solutions.

The $f(a/W)$ equations thus obtained from the fitting data in the form $p(x)/q(x)$ are given below.

$$f_{new} \left(\frac{a}{W} \right)_{AP} = \frac{1.275 \left(\frac{a}{W} \right)^4 + 1.878 \left(\frac{a}{W} \right)^3 - 2.113 \left(\frac{a}{W} \right)^2 + 0.1888 \left(\frac{a}{W} \right) + 0.1447}{\left(\frac{a}{W} \right)^2 - 0.971 \left(\frac{a}{W} \right) + 0.2438} \quad (4.2)$$

$$f_{new} \left(\frac{a}{W} \right)_{HT} = \frac{1.363 \left(\frac{a}{W} \right)^4 + 1.588 \left(\frac{a}{W} \right)^3 - 1.939 \left(\frac{a}{W} \right)^2 + 0.1814 \left(\frac{a}{W} \right) + 0.1404}{\left(\frac{a}{W} \right)^2 - 0.9813 \left(\frac{a}{W} \right) + 0.2511} \quad (4.3)$$

$$f_{new} \left(\frac{a}{W} \right)_{HIPHT} = \frac{2.617 \left(\frac{a}{W} \right)^4 + 0.1831 \left(\frac{a}{W} \right)^3 - 1.217 \left(\frac{a}{W} \right)^2 + 0.01914 \left(\frac{a}{W} \right) + 0.1384}{\left(\frac{a}{W} \right)^2 - 0.9355 \left(\frac{a}{W} \right) + 0.2284} \quad (4.4)$$

The $f(a/W)$ values obtained from equations mentioned above can then be used to calculate the K values for each condition as follows,

$$K_{AP} = \begin{cases} \frac{P.S}{B.W^{3/2}} f_{new} \left(\frac{a}{W} \right)_{AP}, & \text{if } \frac{a}{W} \leq 0.533 \\ \frac{P.S}{B.W^{3/2}} f \left(\frac{a}{W} \right), & \text{otherwise} \end{cases}$$

$$K_{HT} = \begin{cases} \frac{P.S}{B.W^{3/2}} f_{new} \left(\frac{a}{W} \right)_{HT}, & \text{if } \frac{a}{W} \leq 0.533 \\ \frac{P.S}{B.W^{3/2}} f \left(\frac{a}{W} \right), & \text{otherwise} \end{cases}$$

$$K_{HIPHT} = \begin{cases} \frac{P.S}{B.W^{3/2}} f_{new} \left(\frac{a}{W} \right)_{HIPHT}, & \text{if } \frac{a}{W} \leq 0.533 \\ \frac{P.S}{B.W^{3/2}} f \left(\frac{a}{W} \right), & \text{otherwise} \end{cases}$$

Constant ΔK tests for graded specimens

The black vertical dashed lines represent interface regions for G specimens. These regions have not been marked accurately but are nevertheless denoted from the specimen design for an approximation to aid the comparison. The colored horizontal dashed lines on either side of these black lines correspond to the crack growth rate of *UG-HT* specimens at a ΔK value of $22.5\text{MPa}\sqrt{\text{m}}$ (and $25\text{MPa}\sqrt{\text{m}}$ wherever applicable) recorded from the Paris curve fit. As is the norm in this study, 250W corresponds to fine grain and 950W corresponds to coarse grain microstructure.

The constant ΔK curves for *AP* specimens are reproduced in Figure 4.22. For these specimens, the crack growth rate is seen to be increasing as the crack progresses into the interface. This is most probably associated with the microstructural features of the interface. For the *AP* specimen with $\text{BD} \perp \text{CD}$ tested at $\Delta K = 22.5\text{MPa}\sqrt{\text{m}}$, the crack growth rates are fairly constant with the da/dn observed to be between $4 - 5 \times 10^{-5}$ mm/cycle on both sides. While this da/dn value is higher than the corresponding fine grain microstructure from ungraded specimens, it seen to be lower than the corresponding coarse grain microstructure. The lowest value 2×10^{-5} mm/cycle is observed inside the interface. In $\text{BD} \parallel \text{CD}$ tested at $\Delta K = 25\text{MPa}\sqrt{\text{m}}$, the crack growth rate constantly increases from 6×10^{-6} mm/cycle in the fine grain microstructure to about 3×10^{-5} mm/cycle in the coarse grain microstructure. The primary factor leading to such a behavior was argued to be the nature of compressive residual stresses developed in this specimen during SLM process (decreasing from fine grain to coarse grain, refer appendix 6.3). High residual stresses of the compressive nature can lead to crack closure because of the stresses acting in opposite direction of the loading at the crack tip. This serves as a hindrance to the crack growth. More studies involving the residual stresses are required to arrive at a concrete conclusion.

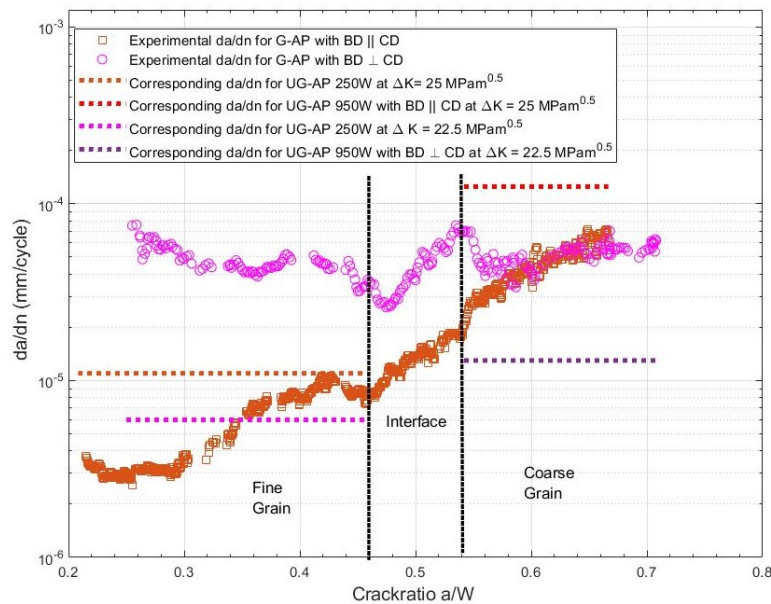


Figure 4.22: Fatigue curve for crack growth rate da/dn under constant ΔK conditions in as-printed (AP) specimens (with the crack progression seen as a function of crack to width ratio a/W).

Figure 4.23 summarises the test data for *HT* specimens used in this study. Observing Figure 4.23 closely, the crack rate is seen to decrease a bit just as the crack front is expected to encounter the interface region when initially progressing from the fine grain microstructure. This can be said for both the specimens, with $BD \perp CD$ as well as $BD \parallel CD$. Also, for the specimen with $BD \parallel CD$, the crack growth rate further keeps decreasing for around third quarter of the representative interface until da/dn value of 2×10^{-5} mm/cycle and then increases again probably when the crack front encounters the coarse grain microstructure on the other end of interface. The da/dn is observed to be between $3 - 4 \times 10^{-5}$ mm/cycle in both the individual microstructures. While this value is comparable to ungraded fine grain microstructure, it is substantially lower than the corresponding coarse grain microstructure. The same cannot be said about the interface in the specimen with $BD \perp CD$. da/dn value is seen to remain constant at 4×10^{-5} mm/cycle. Although, there is a definitive effect of the interface as the crack growth rate is seen to deviate to about 3×10^{-5} mm/cycle on either sides of the interface. These dips in crack growth rates are not significant however it is important to note that these tests are performed at high ΔK value for faster outcome. For representative components similar to the specimen used in this study, the fatigue life could improve by as high as 10^4 cycles.

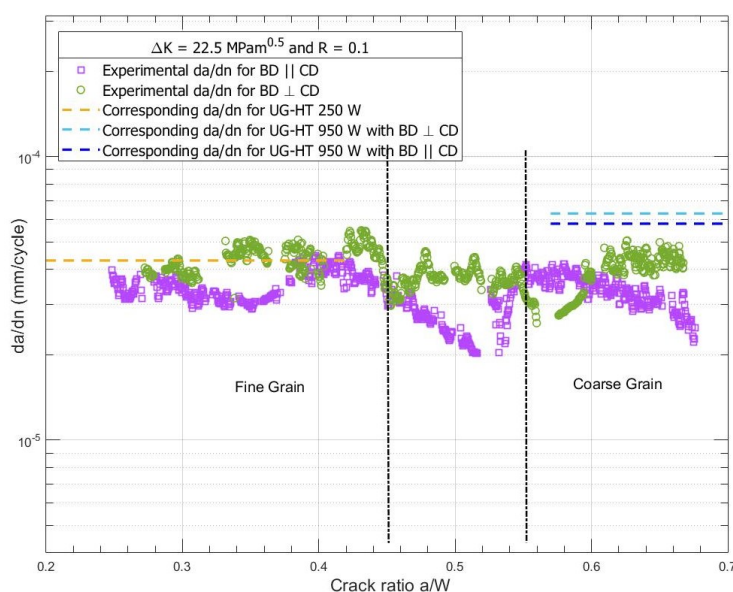


Figure 4.23: Fatigue curve for crack growth rate da/dn under constant ΔK conditions in heat treated (HT) specimens (with the crack progression seen as a function of crack to width ratio a/W).

The effect of interfaces on the crack propagation behavior in *HIPHT* specimens seems to be next to nothing as the crack growth rates are more or less constant throughout the crack progression. A more or less constant trajectory of da/dn is observed in Figure 4.24. For $BD \perp CD$, da/dn is observed to be around $3 - 4 \times 10^{-5}$ mm/cycle for fine grain microstructure whereas it is $4 - 6 \times 10^{-5}$ mm/cycle in the coarse grain microstructure. The same for $BD \parallel CD$ is observed to be around 3×10^{-5} mm/cycle for both. All the da/dn values are found to be higher than the

corresponding crack growth found in ungraded specimen. The obtained results for the graded specimens will be put into perspective by studying the crack paths using EBSD measurement and the fractured surfaces using SEM micrographs in the next sections.

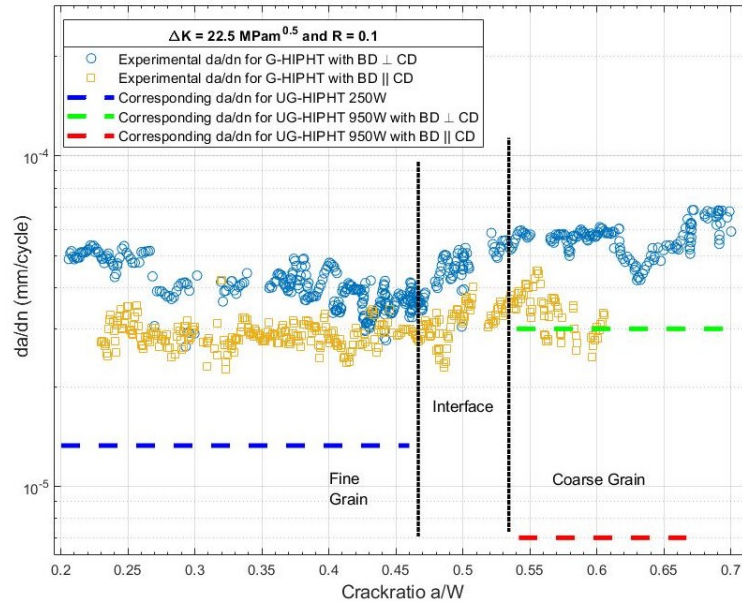


Figure 4.24: Fatigue curve for crack growth rate da/dn under constant ΔK conditions in hot isostatic pressed and heat treated (HIPHT) specimens (with the crack progression seen as a function of crack to width ratio a/W).

4.2.3. Summary

1. Ungraded specimens

- The threshold tests revealed that the *HIPHT* specimens had highest ΔK_{th} values followed by ΔK_{th} values in *HT* specimens and *AP* specimens having the lowest values. The performance of *HIPHT* in these tests can be explained by reduced porosity and absence of brittle Laves phases leading to fewer crack initiation sites. The precipitation of strengthening γ'/γ'' phases further improves their performance, which also holds true for *HT* specimens in comparison with the *AP* specimens.
- 250W fine grain microstructure had better fatigue properties than the 950W fine grain microstructure in all the conditions. The influence of grain size (laser power) and grain orientation (BD) was more pronounced in *AP* condition resulting in a sizeable scatter in the fatigue properties of these specimens.
- Post-processing heat treatments, both *HT* and *HIPHT* were seen to reduce such a scatter. This is stipulated to be the after effect of γ'/γ'' strengthening phases precipitated in these specimens, reduced brittle Laves phases and porosity (in *HIPHT*) influencing the fatigue behavior more than the grain structure.

2. Graded specimens

- New equations for customized K solutions were formulated using the FEM model. These equations helped in calculating the load levels required to maintain a constant ΔK value for the tests and hence isolate the variation in crack growth rate as a function of the position of crack front in the microstructure.
- These tests provided interesting results in and around the stipulated interface regions of *AP* and *HT*. The crack growth rates in *AP* specimens were seen to be decreasing at the onset of the interface and later continuously increasing as the crack propagates through the interface. While in the *HT* specimens as well, the crack growth rates decreased at the onset of the interface, a different u-shaped trend was observed in the interface.
- The crack growth rate curves for the *HIPHT* specimens more or less show no influence of the interface on fatigue crack propagation.

4.3. EBSD analysis of crack paths in graded specimens

EBSD maps for graded specimens in conditions *AP*, *HT* and *HIPHT* are provided in this section. The maps were scanned and processed such that the crack progression through the 250W fine grain microstructure to the 950W coarse grain microstructure in the graded specimens for both $BD \perp CD$ and $BD \parallel CD$ can be observed. Also seen in these scans are the interfaces for all the specimens. The main motivation to generate the EBSD maps was to visually characterize the effect of microstructure on the fatigue crack propagation behavior. It was previously mentioned that the graded specimens were tested with the constant ΔK tests where the crack growth rate is isolated as a function of crack length (or crack width ratio). In simpler terms, with the microstructure varying in graded specimens across the interface, any deflections or disruptions leading to crack arrest can be singled out on the basis of local microstructure which can then explain the results obtained in constant ΔK tests. In all the scans, crack has propagated from bottom (notch side and 250W) to top (crack tip side and 950W). For clarity in the following maps, an enlarged inverse pole figure is provided in Figure 4.25 below and is applicable to all the maps in this section.

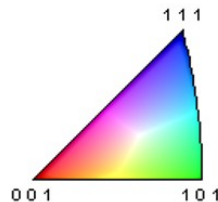


Figure 4.25: Inverse pole figure applicable to the EBSD scans.

4.3.1. As printed specimen

The crack path with respect to the microstructure of *AP* specimen with $BD \parallel CD$ can be seen from the micrographs in Figures 4.26, 4.27 and 4.28. Similar micrographs for the specimen $BD \perp CD$ cannot be provided due to difficulty in etching this specimen with a large crack width. The inverse pole figure (IPF) maps of *AP* specimens with $BD \perp CD$ and $BD \parallel CD$ are shown in Figures 4.29 (a) and (b) respectively. While the difference in grain sizes is apparent from the bottom (250W) to top (950W) in the case of $BD \parallel CD$, it is difficult to distinguish in the case of $BD \perp CD$. This is mainly because the scan area is not sufficiently large along *BD* in the specimens with $BD \perp CD$. Also, the crack width in specimen with $BD \perp CD$ is significantly higher than others due to overloading at the end of test.

Effect of interfaces and melt pools: The interface (seen between the horizontal dotted lines) in the specimen with $BD \parallel CD$ separates the regions with fine grains from 250 W laser power and the coarse grains from 950 W laser power. Significant deflections are seen in this interface (marked by *I* and *MP* in Figures 4.26 and 4.29 (b)). These deflections are confirmed to be the outcome of crack path encountering the melt-pool boundaries in the interface layer visible in the optical micrograph (after etching) shown in Figure 4.26 (refer Figure 4.27 for SEM micrograph). A similar influence of melt pool boundaries and layers is not observed when $BD \perp CD$ as the

shape of melt pools is curved along the crack path in this case which reduces the severity of such deflections. The interface in specimen with $BD \perp CD$ is fairly distinguishable because of the strong $\langle 001 \rangle$ and the region of mishmash (between the white dotted lines in Figure 4.29 (a)). The later was also observed during the microscopy of these specimens in section 4.1.4. A porosity (marked by P) is also seen right at the onset of the interface. Proper reasoning for such an appearance is provided in the section 4.4, where all the fractured surfaces are studied. Crack deflections are evident as a result of the crack path encountering interface in both these specimens (marked by I in Figure 4.29 (a)). For both the specimens, crack path becomes tortuous closer to the interface while it follows a straight trajectory away from interface. One such correlation can be derived from all the instances where the crack path encounters grains closer to $\langle 001 \rangle$ orientations. Crack is seen to be deflected by such grains which may be as a result of the slip planes being oriented at 45° to $\langle 001 \rangle$ direction in fcc lattice. Additionally, this could also be a result of the dendrites being slightly inclined to the crack path direction. A few of these deflections have been marked by 45° in Figures 4.29 (a) and (b).

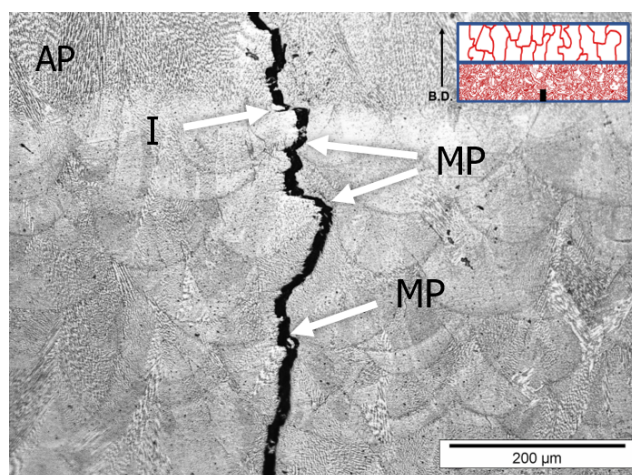


Figure 4.26: Optical micrograph showing the influence of melt pool boundaries and layer tracks on crack deflection in graded as-printed specimen with $BD \parallel CD$ in the 250W and interface region. Point I is interface, points MP are melt pools.

Effect of laser power: In 250W fine grain microstructure, the distinctive random appearance of the grains due to melt-pools can be seen in these maps. A detailed explanation has already been provided in section 4.1.1. Due to the small size of grains in 250W regions, grain boundaries appear to be acting as a barrier to crack progression at many sights. Melt pool boundaries also aid to crack deflection in $BD \parallel CD$. However, globally the crack follows a near linear path. On the other hand, 950W coarse microstructures show a distinction in crack propagation path due to the effect of BD and orientation of grains. In specimen with $BD \parallel CD$, crack shows a tendency to follow the long grain boundaries aligned along the CD . While in specimen with $BD \perp CD$, the same cannot be said as the grains elongated perpendicular to CD .

Figure 4.28 shown below helps in outlining that the effect of melt pool tracks is more pronounced in fine grained microstructure and interface region than the coarse grained

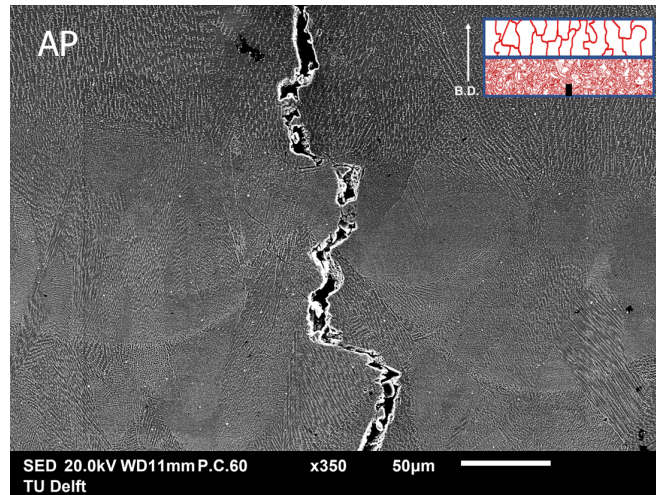


Figure 4.27: SEM micrograph showing the influence of melt pool boundaries and layer tracks on crack deflection in graded as-printed specimen with BD \parallel CD in the 250W and interface region.

microstructure. A closer examination of SEM micrograph from Figure 4.27 helps in understanding that the grain structure is again at the helm of affairs leading to such a distinction. The fine grains produced in 250W region are constricted to the individual melt pools while the coarse grains span across several melt pool boundaries. Due to the changing orientations of the fine grains at such a melt pool boundary, the crack path is deflected to travel along a more favorable path until the influence of principal stress direction starts to kick in. After which, the crack deflects again to keep growing along the original trajectory. The grains in 950W are oriented preferably along BD and cut through the melt pool boundary. Because of this, the effect of melt pools in 950W region is greatly reduced. In the coarse grain microstructure of BD \parallel CD, a point marked by *D* shows a significant deflection. Such a deflection is unwarranted and cannot be explained by the surrounding grain orientations. This could be an effect of the crack path at the surface realigning with the crack front growing in the bulk material or due to the local residual stresses.

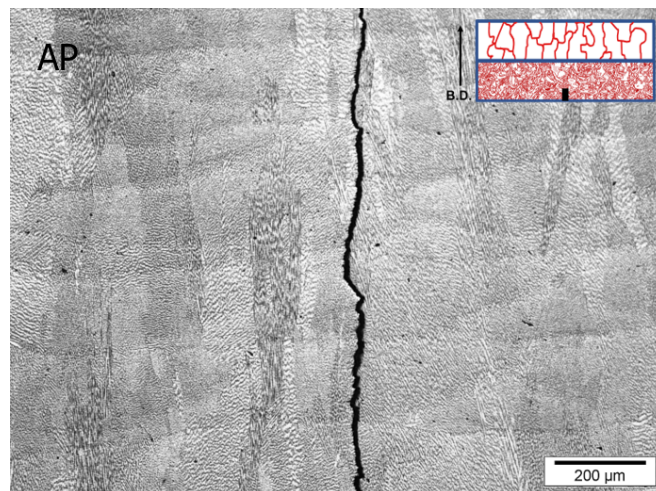


Figure 4.28: Optical micrograph showing the crack path in 950W region of as-printed graded specimen.

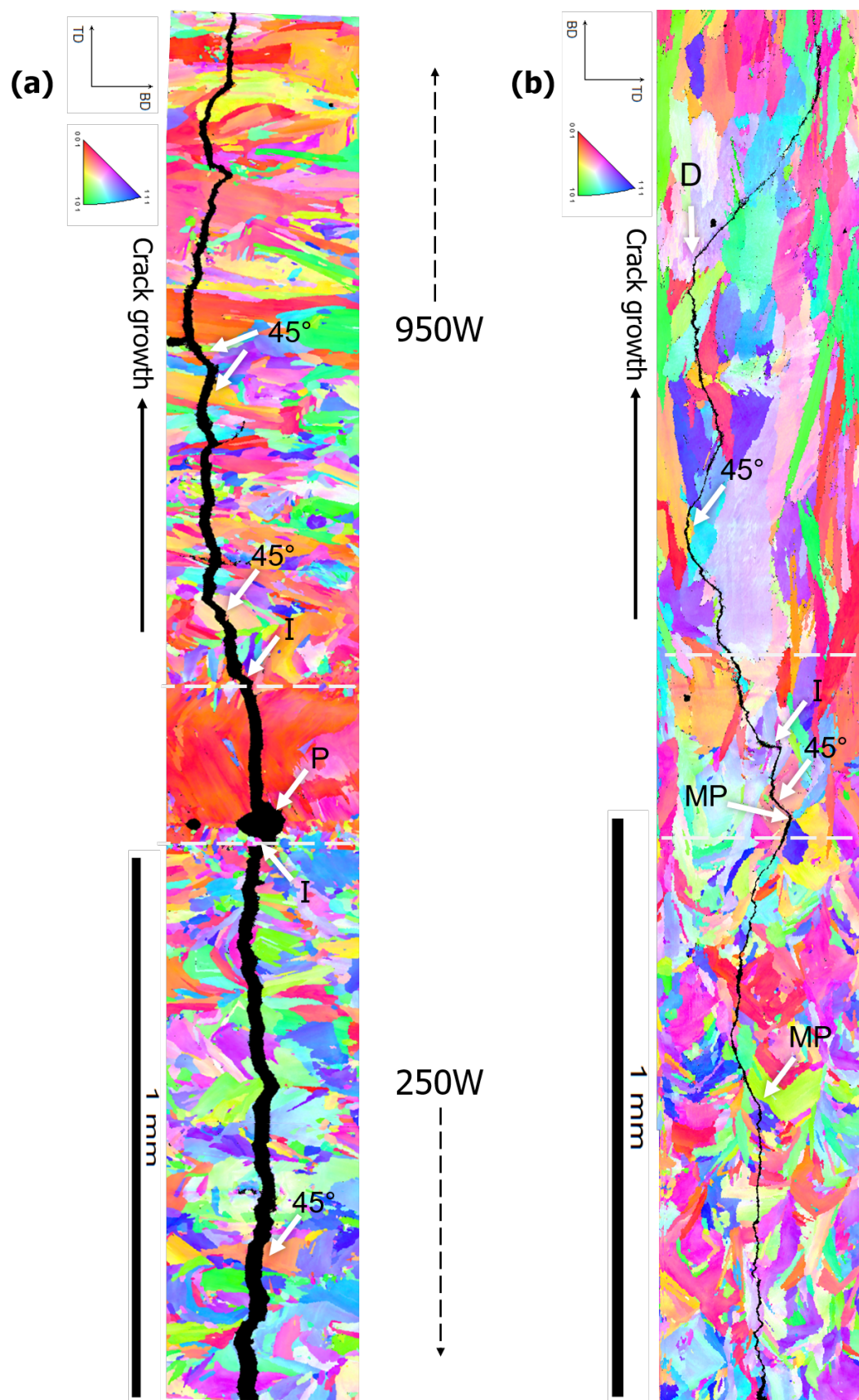


Figure 4.29: EBSD inverse pole figure (IPF) map of the interface region in G-AP specimens with (a) $BD \perp CD$ and (b) $BD \parallel CD$. Points I are interfaces, MP are melt pools, 45° is deflection by $\langle 001 \rangle$ grains and D is a rare deflection described in the text.

4.3.2. Heat treated specimen

Figures 4.30 (a) and (b) show the optical micrographs of the interface while Figures 4.31 (a) and (b) show IPF maps of *HT* specimens with $BD \perp CD$ and $BD \parallel CD$ respectively. Same as in *AP*, the significance of *BD* in the context of grain orientation is retained as the grains are still seen to be orientated along *BD* after homogenisation and solution heat treatment followed by aging. However, heat treatment has introduced a few outliers which was not the case with *AP* specimens. There are comparatively coarser grains visible in 250W region of fine grain microstructure while recrystallization has introduced a higher number of fine grains in 950W coarse grain microstructure.

Interfaces are depicted by horizontal dashed lines. The mishmash region seen at the interface (between the white dashed lines in Figure 4.31 (a)) in specimen with $BD \perp CD$ is hardly seen to be affected by the heat treatment. However, for specimen with $BD \parallel CD$ seen in Figure 4.31 (b), interface is difficult to distinguish due to the outliers. Here, the etched microstructure is helpful in pinpointing the interface layer and alleviates the possible confusion. For both specimens, the microstructure around interfaces disrupt the crack progression as seen from the deflected crack paths. This can also be seen closely in the etched microstructures from Figures 4.30 (a) and (b). Deflections at the interface are marked by *I*. As was previously observed in section 4.1.2, the melt pools are not visible here as well. This could be the knock-on effect of the partial recrystallization mentioned above and observed from IPF maps. Also observed from the IPF map of $BD \parallel CD$ is a rare secondary micro-crack at the surface (marked by 2nd in Figure 4.31 (b)). The formation of secondary micro-cracks in *HT* specimens is discussed in detail in section 4.4.

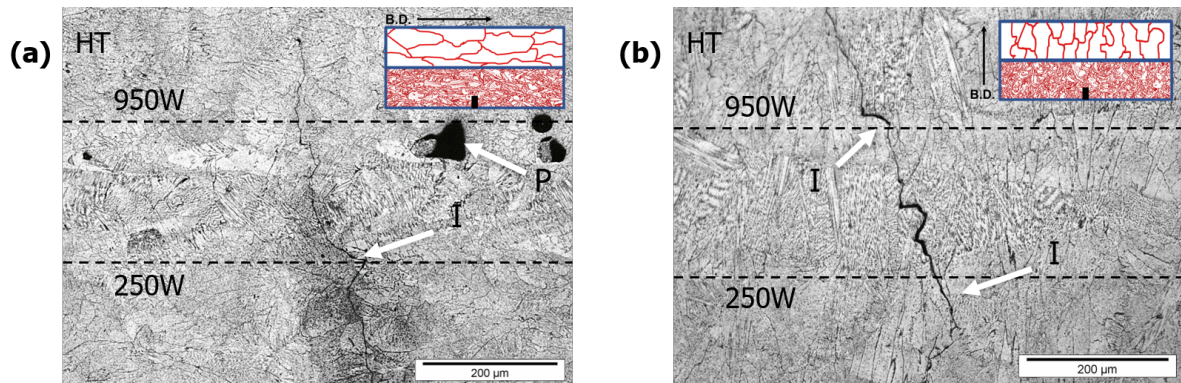


Figure 4.30: Optical micrograph showing the influence of layer tracks and mishmash dendritic pattern at the interface on crack deflection in graded as-printed specimen with $BD \perp CD$.

Also seen from Figures 4.31 (a) and (b) is the very low number of $\langle 111 \rangle$ grain orientations in the 950W coarse grain region. This observation is backed by the fact that the XRD peaks for $\langle 111 \rangle$ were seen to be missing in section 4.1.2. This was associated with the possible recrystallization characteristics in the temperature range of 1080°C. Also to be noted in the specimen with $BD \perp CD$ is a lack of porosity similar to the one seen in *AP* condition. This is confirmed to be only at the surface of the crack path and the scanned area since these 'porosity' features are seen in the optical micrograph in Figure 4.30 (a), marked by *P*. They are also observed later during the fracture surface analysis of these specimens in section 4.4.

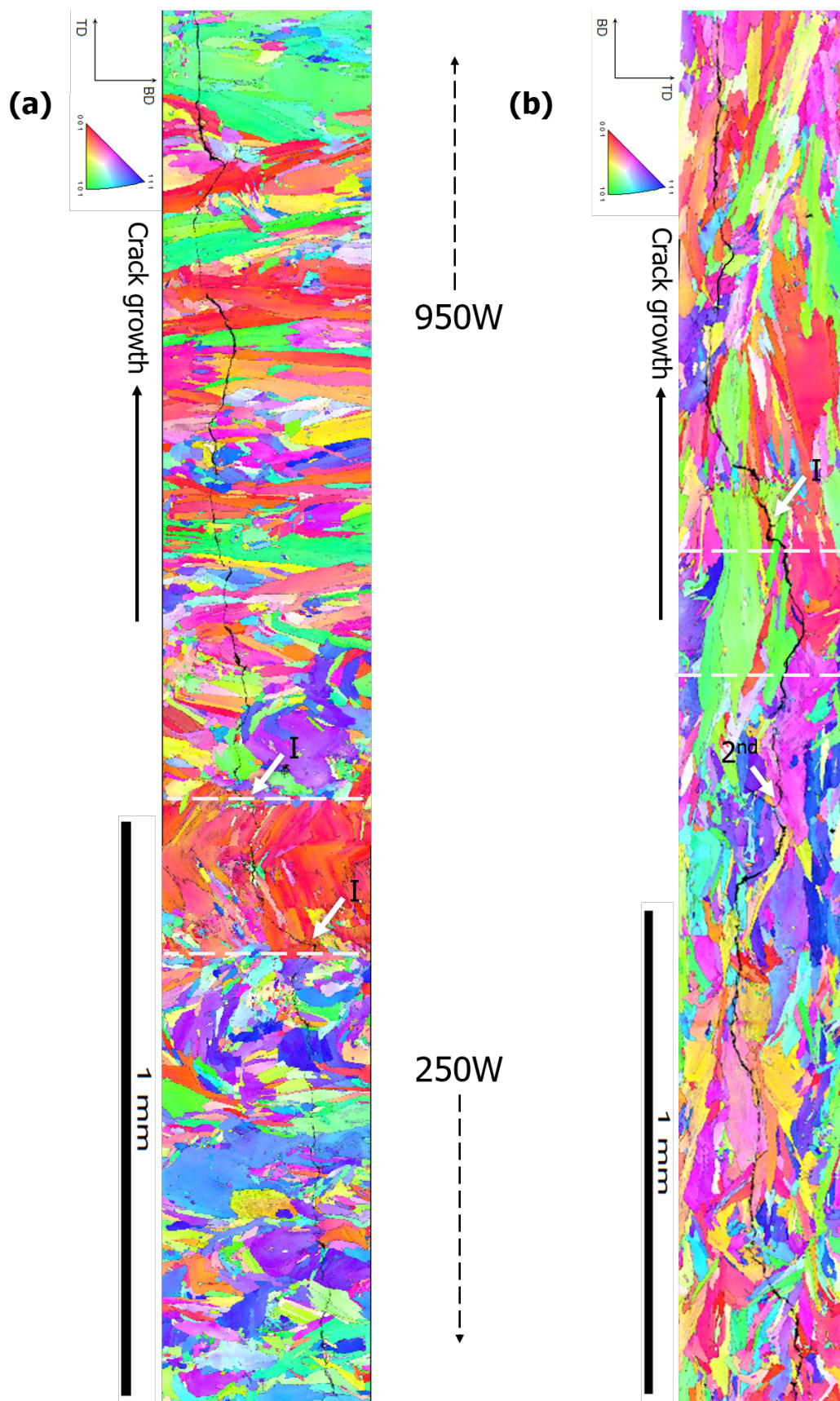


Figure 4.31: EBSD inverse pole figure (IPF) map of the interface region in G-HT specimens with (a) $BD \perp CD$ and (b) $BD \parallel CD$. Points I are interfaces and 2nd is a secondary crack at surface.

4.3.3. Hot isostatic pressed and heat treated specimen

The IPF maps for *HIPHT* specimens are different from the ones seen in *AP* and *HT*. *HIPHT* maps are seen in Figure 4.32. The distinct columnar grains generated from the SLM process have been altered into equiaxed grains with a polyhedral shape. Grain coarsening and recrystallization are also a direct outcome of hot isostatic pressing [27]. Another point to note here is that the resultant grain growth shows preference for the respective BD in both specimens. These grains are very similar to the ones expected in a heat treated wrought IN718 material. Such a recrystallization and annealing twins are expected in wrought materials due to the hot working which involves high pressure at elevated temperatures, similar to the HIPing process [56]. All the stated observations are applicable irrespective of the regions (250W, 950W and interface) as well as for $BD \perp CD$ and $BD \parallel CD$.

An interesting additional feature that aids the crack deflection in the *HIPHT* specimens are the twins introduced into the microstructure as a result of the hot isostatic pressing. There are numerous instances for the same marked by *twin* in Figures 4.32 (a) and (b). These twins are detrimental for crack initiation stages, however, prove to be beneficial in propagation stage as they deflect the crack path along the (111) planes due to a higher stacking fault energy associated with the twinning sites [64]. So, in the grains where these (111) twins are oriented at an angle to the crack path direction, a crack deflection is the resultant outcome. These twins are also observed during the fracture surface analysis and more discussion for the same will follow in section 4.4. The points marked by *GB* will be used as a reference for the further discussions in section 4.4.

Deflections at the interface that were seen in *AP* and *HT* specimens, are not observed in *HIPHT*. A possible aid to the above observation is again the complete removal of microstructure history during this post-processing.

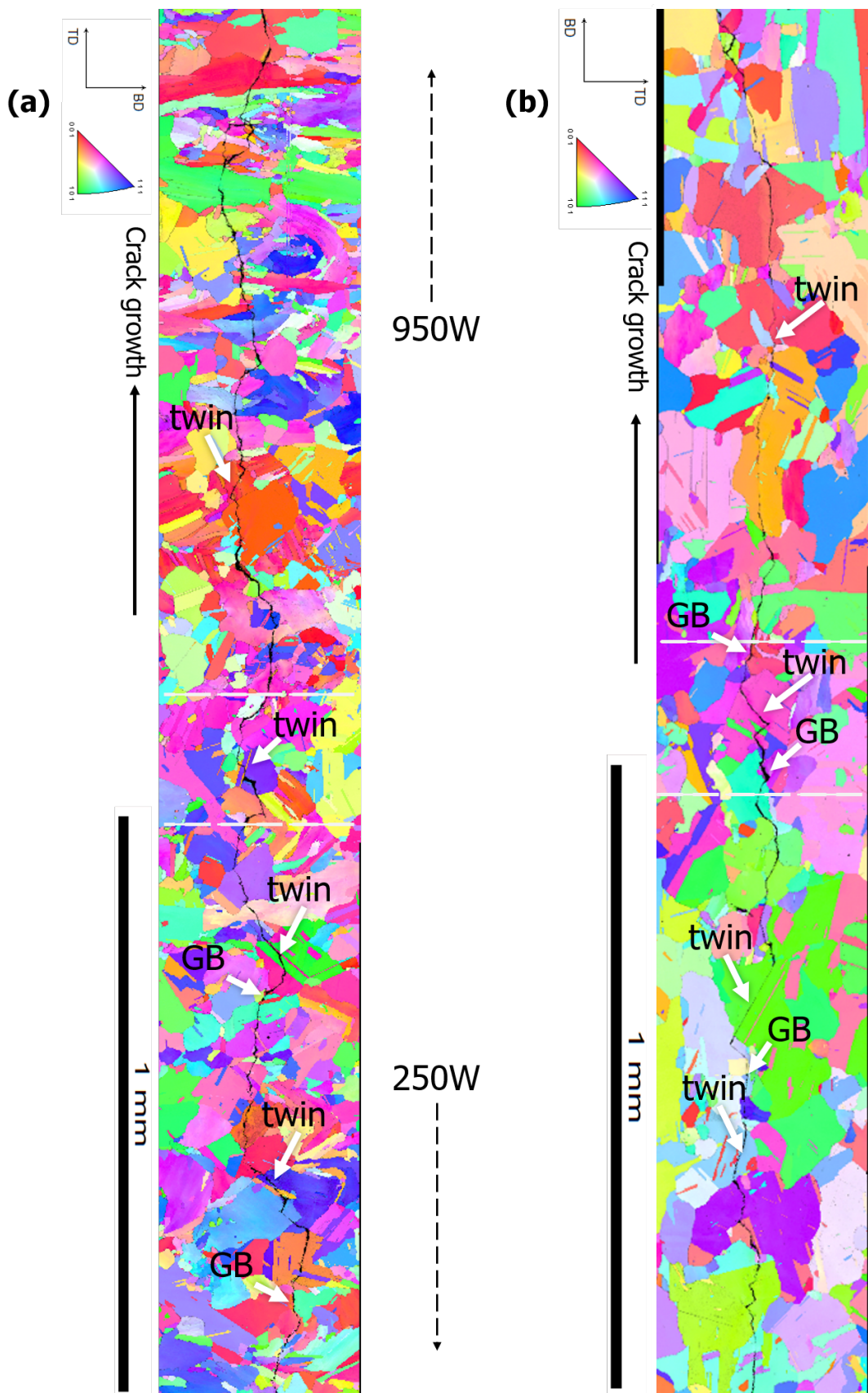


Figure 4.32: EBSD inverse pole figure (IPF) map of the interface region in G-HIPHT specimens with (a) $BD \perp CD$ and (b) $BD \parallel CD$. Points GB are the grain boundaries and twin are the twin boundaries.

4.3.4. Summary

- *AP* and *HT* specimens clearly show the relationship between BD and grain orientation in 950W regions of the graded specimens wherein the columnar grains are elongated along BD. The presence of coarser grains in regions produced by 950W laser power and finer grains in regions produced by 250 W laser power is confirmed again. A few outliers are introduced in the *HT* specimens due to partial recrystallization.
- The crack path is tortuous in the regions in and around the interface in all the specimens from *AP* and *HT*. Reasons associated to this could be derived from the several barriers introduced by such an interface including but not limited to - porosity in $BD \perp CD$, interface layer boundaries, gradient grain size (more tortuous in 250W and linear in 950W). In the case of *AP* specimens, the grain orientations closer to $\langle 001 \rangle$ also deflect the crack path. This was associated with the local dendritic orientations and slip plane directions.
- *HIPHT* show an entirely different microstructure as compared to *AP* and *HT* specimens. This microstructure consists of equiaxed polyhedral grains growing and recrystallizing due to HIPing. Twin boundaries are also introduced in the microstructure as a result. The presence of interface is completely erased in these specimens and subsequently has a direct effect on the crack path being far less tortuous than in *AP* and *HT*.
- The EBSD maps help in identifying the crack path in the individual microstructures as well as graded interfaces. The possible deflections in and around the interfaces also explain the dip in crack growth rate from constant ΔK tests for *AP* and *HT* specimens. While the lack of these deflections coupled with a drastic change in the microstructure of *HIPHT* specimens can explain the more constant crack growth rates.

4.4. Fracture Surface Analysis

Figure 4.33 shows 50X magnification micrographs of the fracture surfaces in *AP*, *HT* and *HIPHT* conditions revealing the interfaces in the respective graded specimens. Crack direction for all the micrographs presented in this section is from left (notch side) to right (overloaded side).

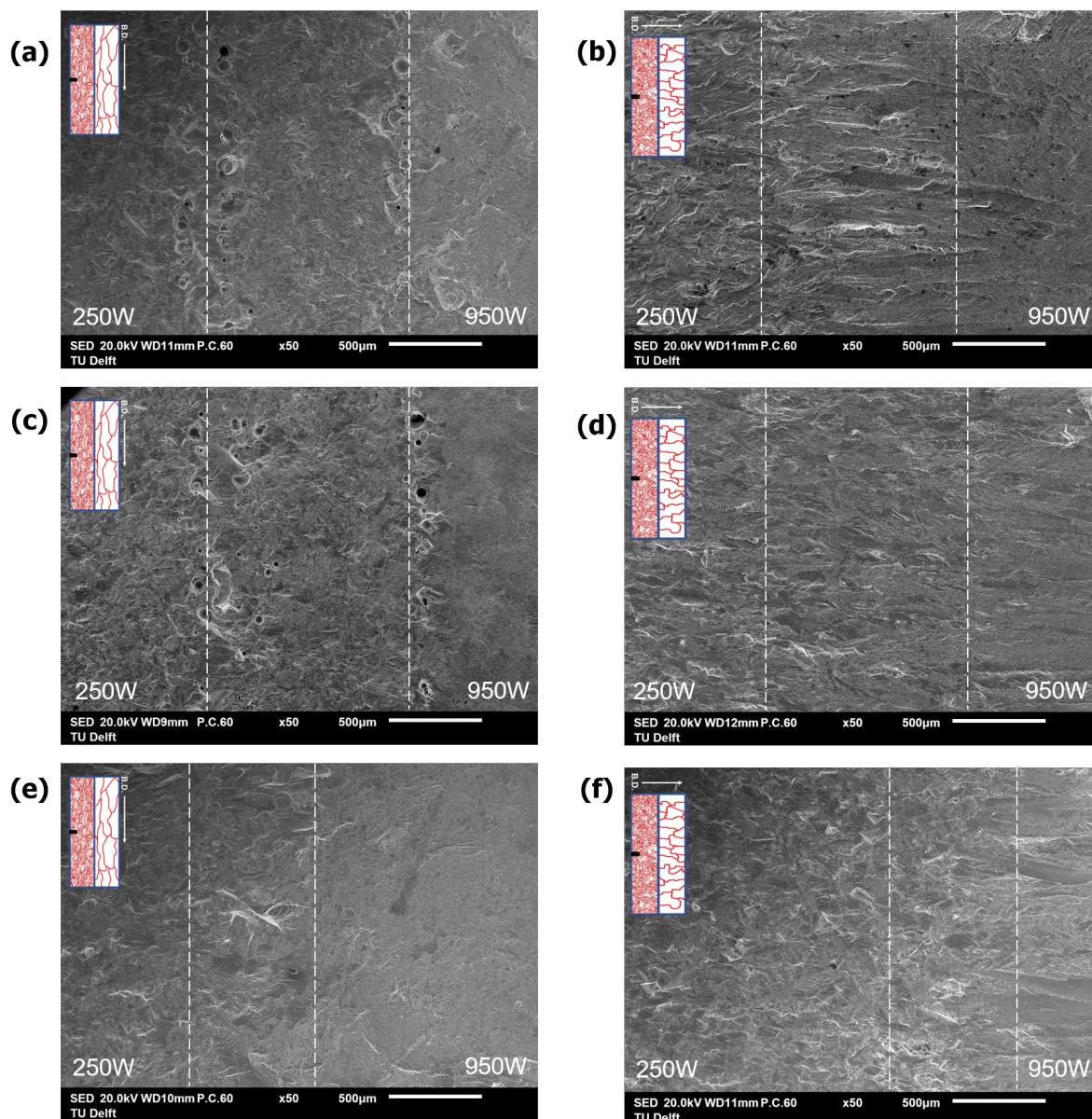


Figure 4.33: SEM micrographs showing fractured surface in interface regions for specimen conditions (a),(b) - *AP*; (c),(d) - *HT*; (e),(f) - *HIPHT*.

4.4.1. Fractured surfaces in fine grained (250 W) microstructure

From Figure 4.33, the streaks flowing along the CD in 250W regions are a usual characteristic of ductile transgranular crack propagation. However, a higher magnification reveals a significant difference between fracture surfaces and the inherent crack growth mechanism with the processing condition.

AP specimens from both $BD \perp CD$ and $BD \parallel CD$ are in general characterised by the appearance of stair like features (seen in Figure 4.34) oriented in multiple directions along the fracture plane. On first look these could be mistaken for the striations. However, the spacing between the stairs is too high for the crack growth rates obtained for these specimens. Such an appearance helps in concluding that the crack propagation takes place through the epitaxial dendrites that were seen to grow along the $\langle 001 \rangle$ directions of the columnar grains. This also helps in ascertaining the role of dendrites and $\langle 001 \rangle$ directions on the crack deflections in *AP* specimens discussed during the EBSD section 4.3. The stairs could indicate the local solidification direction of fine grain structure thus produced and are subsequently revealed as the crack progresses by separating the dendrites. Figure 4.34 (b) shows a ridge on the fracture surface. Such a ridge is left behind by the grain boundaries with different local orientations in adjacent grains. Subsequently, melt pool boundaries can also lead to such a ridge. The random orientation of the stairs across this ridge further signifies the lack of preference for solidification of these grains along the *BD* due to the low heat input of 250 W laser power. A similar fatigue crack propagation was well explained by the zigzag cracks in a randomly oriented fine grain microstructure from the work of Zhang et. al. [67].

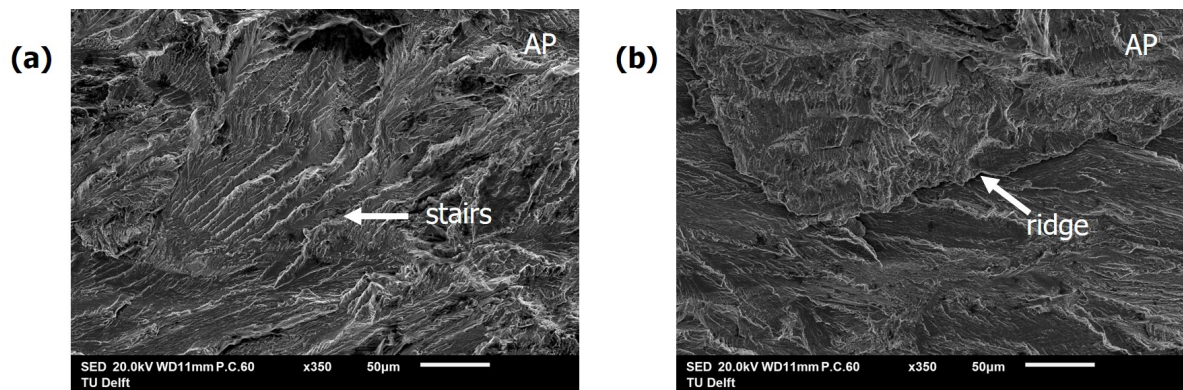


Figure 4.34: SEM micrographs showing fractured surface in 250W region of G-*AP* specimens with (a) stair like features, and (b) facets revealing two different grains with features aligned in two distinct directions.

HT specimens also have similar features but the stairs are significantly sharper and look like lamellae. These lamellae are also accompanied by the secondary micro-cracks (seen in Figure 4.35). Both of these can be attributed to the precipitation of strengthening γ' and γ'' phases inside the γ matrix while the comparatively brittle δ phase precipitating locally along the dendrites as also along the grain boundaries. The micro-cracks are formed as a result of secondary cracking along the slip bands oriented at an angle. The strengthening precipitates can promote such secondary cracks to diffuse the stress buildup along principal loading direction [68]. This further explains the better ΔK_{th} values of *HT* specimens compared to *AP* as the secondary cracks inhibit short crack growth (refer section 4.2.1). The observed secondary micro-cracks in precipitation strengthened AM IN718 are consistent with the results of Pei et. al. [50] and Zhang et. al. [67].

HIPHT specimens show all the combined features from *AP* and *HT* specimens. Other additional features observed in these specimens are the flat faceted surfaces

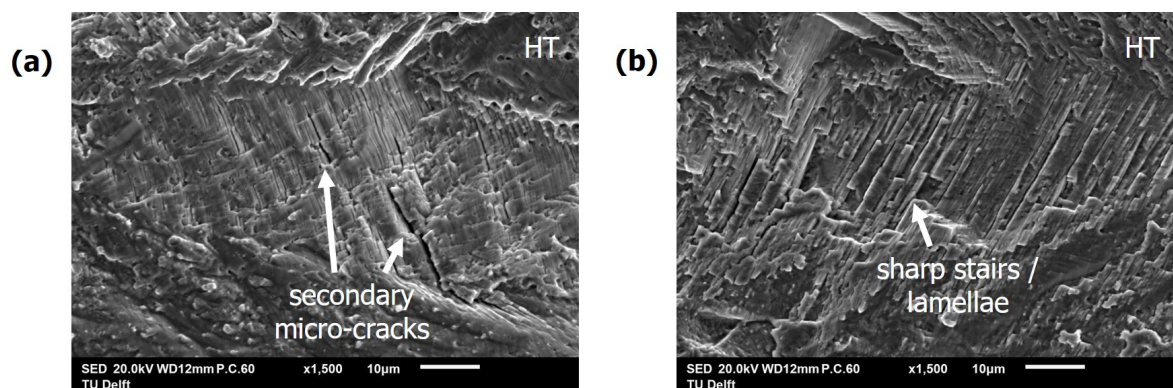


Figure 4.35: SEM micrographs showing fractured surface in 250W region of G-HT specimens with (a) secondary micro-cracks, and (b) sharp stair like features - lamellae.

and the twin boundaries revealed along the fracture surface (seen in Figure 4.36). It is natural to observe the twins as they are process induced during the HIP stage. The faceted surfaces are a result of the cracks propagating through the twin boundaries (marked by *twin* in Figures 4.32 (a) and (b)). Another reasoning for such facets is that the polygonal shape of grains promotes local intergranular crack growth whenever only a small part of grain boundary is encountered by the crack path as it progresses through them. The presence of carbides at the grain boundaries observed in *HIPHT* during the microscopy also make these sites susceptible to cracking. For reference, Figures 4.32 (a) and (b) show the EBSD maps for the same specimens, some small grains are seen to be aiding the crack growth through the sharp grain boundaries marked by *GB*. The grain boundaries in this case are a path for easier progression due to the carbide evolution along the grain boundaries after HIPing and subsequent HT as already mentioned. Such faceted fracture surfaces are similar to the ones observed for wrought IN718 (reported by Clavel et. al. [56]).

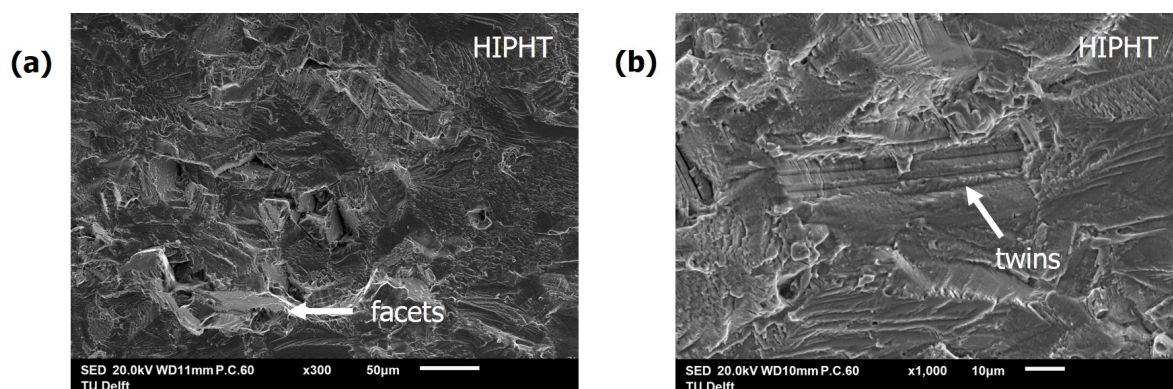


Figure 4.36: SEM micrographs showing fractured surface in 250W region of G-HIPHT specimens with (a) flat faceted surfaces with other features similar to those in AP and HT, and (b) twin boundaries on the fracture surface.

4.4.2. Fractured surfaces in coarse grained (950 W) microstructure

All the specimens produced with 950W laser power show similar story irrespective of the BD or the post-processing condition. This is a rather interesting find in the context

of HIPHT specimens as EBSD revealed that the grain structure is entirely changed as compared to AP and HT specimen for both BD. The fracture surfaces in all these specimens is entirely featureless (as seen in Figure 4.37). Such featureless fracture surfaces have been previously reported by Kim et. al. [58].

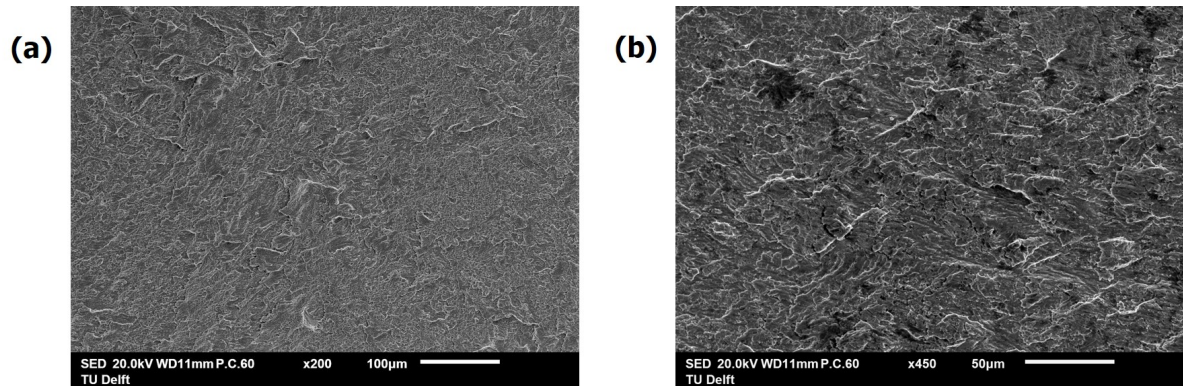


Figure 4.37: SEM micrographs showing fractured surface in 950W region of G-HIPHT specimens representative of both BD as well as all the post-processing conditions.

4.4.3. Interfaces in graded specimens

The interfaces for $BD \perp CD$ from AP and HT can be seen in Figure 4.33 (a) and (c) respectively. These interfaces showcase the black spots or the 'porosity like features' that were seen during microscopy as well as the EBSD analysis (marked by P in Figures 4.29 (a) and 4.30 (a)) for the specimens with $BD \perp CD$ with the mishmash grain structure at interface. Fracture surfaces has helped in revealing the identity of these spots as the unmelted powder particles induced during the processing itself. Lack of fusion at the interface with the surrounding matrix due to these regions being built side by side could be the primary reason for their lack of dissolution. Figure 4.38 shows the higher magnification micrographs of these particles and a subsequent EDS analysis on these particles revealed a composition similar to that of the IN718 powder. The unmelted particles probably dissolved into the matrix after HIPing which is why they are not seen in fracture surfaces in HIPHT specimen (Figure 4.33 (e)).

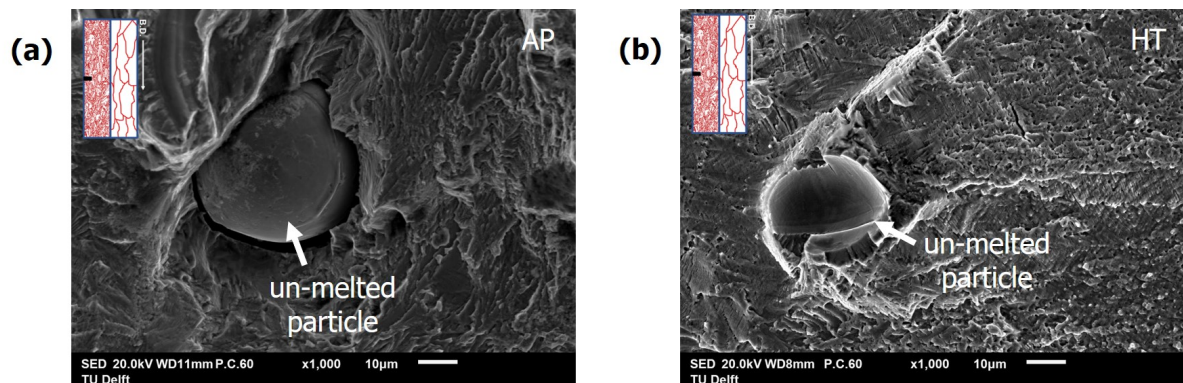


Figure 4.38: SEM micrographs showing fracture surfaces revealing the particulates in interface regions of AP and HT specimens with $BD \perp CD$.

4.4.4. Summary

- SEM observation of the fracture surfaces shows that for fine grain regions corresponding to 250W, the crack propagates locally in random directions for each individual grain. This is most likely associated with the solidification structure of the melt pools produced with lower laser power of 250 W. The equiaxed grains produced are anticipated to have no texture resulting in a higher degree of variation in crack propagation direction. Above conclusions drawn from the random direction of stairs and lamellae that were observed in these specimens. Such a complex appearance of these surfaces hints towards a disruptive crack propagation behavior. This could explain the lower da/dn values obtained for the fine grain microstructure in section 4.2.1.
- Significant features observed in 250W regions are: AP - local stairs formed due to the dendritic structure of the grains and ridges formed because of the different orientations in adjacent grains across grain boundaries and melt pool boundaries; HT - sharp lamellae and secondary micro-cracks because of the strengthening γ' and γ'' phases; HIPHT - twins and faceted recrystallised grains protruding out of surface at several places and also accompanied by all the features listed under AP and HT.
- Coarse grain microstructure produced with 950 W laser power has more or less a featureless fracture surface with a river pattern closer to the interface. This observation stands true for all the AP, HT and HIPHT specimens with both BD.
- Interfaces in AP and HT specimens with $BD \perp CD$ has un-melted powder particles embedded in the matrix which significantly affected to the crack deflection evident from the trials around them.
- There is a definitive region of transition from fine grain microstructure to coarse grain microstructure. This is evident from the varied differences in crack propagation behavior discussed for the respective individual microstructures. Such a transition is important in this context as is seen from the crack growth rate measurements in constant ΔK tests. These tests revealed a decrease in crack growth rates across the interface and such a transition possibly proves to be a barrier for crack progression.

Conclusions and Future Recommendations

5.1. Conclusions

Based on the set research objectives from section 2.6, the following conclusions can be drawn from this study:

- **Research Objective 1: Investigate the microstructural evolution in ungraded and graded IN718 with the post-processing heat treatments (AMS 5383 and AMS 5664E) and compare with as-printed condition.**

1. The process parameters of SLM have a direct effect on the microstructure of as-printed (*AP*) specimens. A higher 950 W laser produced a columnar coarse grained microstructure while a lower 250 W laser produced a relatively equiaxial fine grained microstructure.
2. For the coarse grain microstructure, columnar grains were elongated along the building direction (BD) with the γ dendrites following the same suit. Because of this, the grains were elongated along direction parallel to length for 950W specimen with $BD \perp CD$ and parallel to the width for 950W specimen with $BD \parallel CD$. On the other hand, fine grains were randomly oriented which is visible from the orientation of the inherent γ dendrites.
3. Heat treated (*HT*) specimens showed a similar grain structure as *AP* but the melt pool boundaries were not seen. Additionally, a large amount of rod-like δ precipitates are formed in grain boundaries and in interdendritic spaces.
4. Hot isostatic pressed and heat treated (*HIPHT*) specimens showed a tendency to undergo grain recrystallization and coarsening due to HIPing. The polyhedral grain structure thus observed had no resemblance to *AP* and *HT* specimens. Twins and intergranular carbides are other features observed in *HIPHT* microstructures.

5. The interface region of graded *AP* specimen with $BD \perp CD$ was characterized by a mishmash pattern of melt pools and dendrites extending from 950W and 250W zones. While, the interface region of graded *AP* specimen with $BD \parallel CD$ was characterized by the size of melt pools. The mishmash pattern from $BD \perp$ was unchanged in *HT* while the interface in $BD \parallel CD$ was identified from the sharp interchange between the grain size and orientation of dendrites in 950W and 250W zones. Interfaces in *HIPHT* specimens were seen to be entirely diminished.
- **Research Objective 2: Perform a quantitative and qualitative analysis of the combined influence of grain size, grain orientation, functional grading and heat treatments on the fatigue crack propagation behaviour.**
 1. The 250W fine grained microstructures were found to be showcasing superior fatigue crack propagation behavior (ΔK_{th} and da/dn) than the 950W coarse grained microstructure in *AP* and *HT* specimens. While the same was true for da/dn values in *HIPHT*, ΔK_{th} showed an opposite trend. The observed trends were explained on the basis of the effect that the grain sizes have on fatigue behavior.
 2. The post-process heat treatments reduced the scatter between fatigue properties of individual microstructures in *HT* and *HIPHT* as compared to *AP* specimens. This is attributed to the precipitation strengthening following the aging treatment. Such a strengthening could have led to a reduction in the cumulative effect of grain sizes and orientations on the fatigue propagation behavior. While for *HIPHT*, the possible explanation is also derived from the diminished distinction between the microstructures due to HIPing.
 3. It was observed from the constant ΔK tests that the graded microstructures in *AP* uniquely influence the da/dn values. While the values obtained for the 950W and 250W zones were different from their ungraded counterparts, the crack growth rates are seen to be reducing as the crack path encounters the interface regions in *AP* and *HT* specimens.
 4. There is no apparent effect of the interface on da/dn in *HIPHT* specimens due to the diminished graded interfaces as a result of the grain coarsening and recrystallization.
 5. Only the 250W *AP* specimen shows comparable or better da/dn values than the *HT* wrought IN718. None of the other *AP*, *HT* and *HIPHT* individual microstructures perform better than wrought material (ΔK_{th} and da/dn). However the gap progressively improves with post-process heat treatments, especially *HIPHT*.

- **Research objective 3: Evaluate the underlying effect of microstructure and heat treatment on the crack path in graded material.**

1. EBSD measurements of the crack paths in graded specimens served a dual cause: (1) to understand the microstructure evolution in the graded specimens in and around the interface regions due to the laser powers in two zones, building directions as well as the subsequent post-process heat treatments, (2) to understand the effect of microstructure evolution on fatigue crack path and relate the inference with the results obtained from respective constant ΔK tests.
2. Melt pool tracks and interface layer boundaries led to the crack deflection in specimens with $BD \parallel CD$ from *AP* and *HT* respectively while the mishmash interface layer in specimens with $BD \perp CD$ also has an influence on the crack path in both *AP* and *HT*. Additionally, the grain orientations closer to $\langle 001 \rangle$ influenced the crack path in *AP* specimens. Crack paths in *HIPHT* are deflected by the twins but the difference in the gradient microstructure across interfaces in these specimens was seen to be diminished due to HIPing.
3. Transgranular crack propagation is found to be dominant for all cases. The crack growth mechanism characterised by the featureless fracture surfaces is similar in coarse grain microstructure for all the conditions - *AP*, *HT* and *HIPHT*. However, different crack growth mechanisms are at action in case of the fine grain microstructure. In addition to the individual grains, dendrites also seen to be influencing the local crack propagation direction in these cases. In *HT*, micro-cracking is dominant while in *HIPHT*, occasional intergranular propagation through the twin boundaries and carbide containing grain boundaries lead to a faceted fracture surface.

- **General conclusions:**

1. A good understanding of additively manufactured Inconel 718 is established by studying the microstructures and fatigue crack propagation properties of the ungraded specimens.
2. This study on tailored microstructures processed via selective laser melting hints towards a positive outcome in the context of designing future Functionally Graded Materials. The interfaces and graded microstructures thus obtained have a definitive effect on the crack propagation behavior, observed experimentally (in constant ΔK tests) as well as visually (EBSD and fracture surface analysis) which confirms the feasibility of fabricating the FGMs from Inconel 718 using AM and SLM.

5.2. Future Recommendations

The following recommendations are proposed for the future work on the additive manufacturing of functionally graded Inconel 718:

1. A high resolution microscopy of the microstructures and fracture surfaces is required to understand the exact effect of the precipitate size and morphology on the fatigue crack interaction in as-printed Inconel 718 as well as in the post-process heat treated specimens. Additionally, a quantitative grain size analysis using EBSD of larger scan areas can better explain the link between microstructure, post-process heat treatments and grading.
2. Residual stresses have been previously linked to be influencing the local mechanical properties of printed parts. It is essential to study the development of the residual stresses during printing as well as the subsequent post-processing. This can also be done with the aid of simulations using FEA models of residual stress buildup and temperature profiles inside the material during printing of a specific specimen geometry. Refer appendix 6.3.
3. Porosity also plays an important role in the final mechanical properties as well as fatigue behavior in AM parts. An extensive study on the porosity size and number distribution using x-ray μ CT can help in understanding the process induced porosity in graded as well as ungraded specimens and their correlation with the observed results from this study.
4. This study only aimed at evaluating the effect of a single interface. It would also be interesting to fabricate specimens with multiple interfaces and sandwiched microstructures. This may help in further improving the fatigue response of AM IN718 parts in as-printed and heat treated conditions. Many studies have also discussed using a differently oriented building directions such as at 45° and 60° to the building platform to improve the mechanical response of AM parts. Using similar concept in graded microstructures can lead to further variation in the design of FGMs.
5. A few interesting results were found from the x-ray diffraction phase analysis. A lot of literature is available from the previous works involving phase field modelling of microstructure evolution during additive manufacturing. It will be worthwhile to perform more such studies in the context of texture evolution, precipitates and post-processing.
6. The main focus of this study was to evaluate crack propagation due to fatigue under cyclic loading at room temperatures. Studies involving but not limited to fracture toughness measurements can help isolate the shift in toughening mechanisms due to the graded microstructures and the inherent interfaces even further.
7. Designing such FGMs for high temperature applications can also be pivotal in further discussions involving AM. Testing these specimens at high temperatures such as to evaluate their performance under high temperature fatigue and thermomechanical fatigue will also be interesting.

6.1. Fixture drawing and test setup

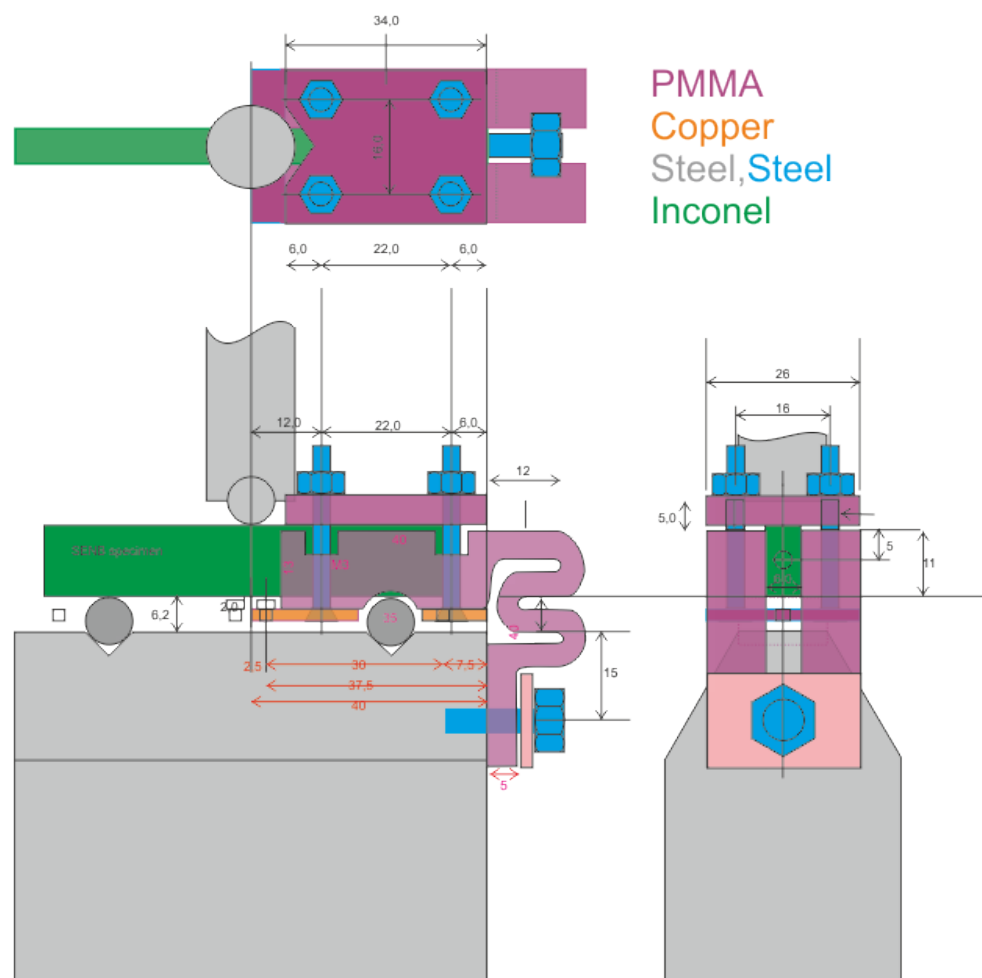


Figure 6.1: Drawing of the specimen fixture used to clamp the specimen on to the main support.

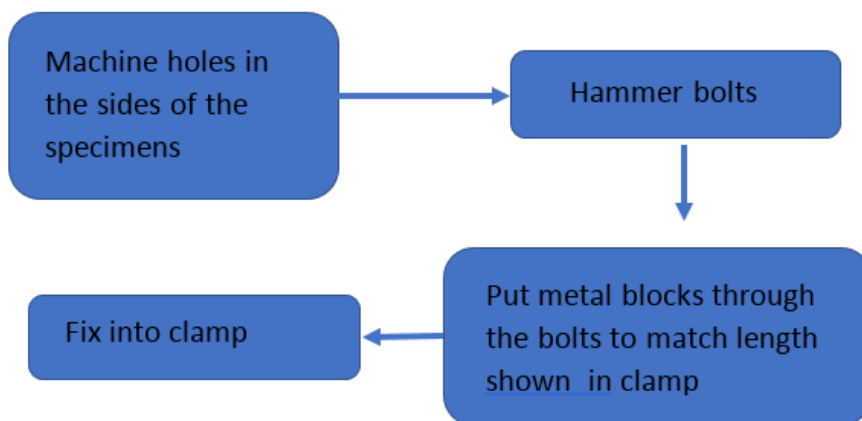


Figure 6.2: Flowchart showing the prerequisite steps required to prepare the specimen before testing.

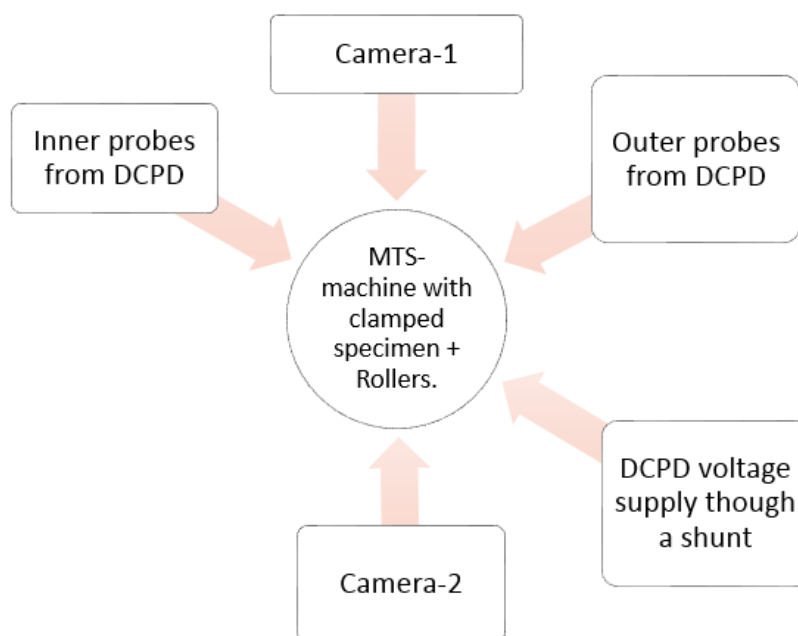


Figure 6.3: Flowchart showing the different components employed in the test setup.

6.2. Matlab algorithm for processing raw MTS data

Step 1 : The first step is to reduce the data per cycle.

```

function [a,n,delP]=reducean(cracklength , cycles , force , skipvariable )
%Input variables in order: peak valley cracklength ,
%peak valley segment(not cycle) number,peak–valley force values ,
%a skip variable to skip data points in case of too many data points

[maxdata,~]=size(cracklength); %to find out the size of the
%input variables
%Initialize all variables to be used
a=zeros(100000,1);
tempa=zeros(100000,1);
tempn=zeros(100000,1);
n=zeros(100000,1);
delP=zeros(10000,1);
tempdelP=zeros(100000,1);
i=1;
j=1;

    while j<maxdata %move along the input variables till last
tempdelP(i)=abs(force(j)–force(j+1)); %calculate delta P
tempn(i)=floor(cycles(j+1)/2); %calualte cycle number
tempa(i)=(cracklength(j)+cracklength(j+1))/2;
%calculate average crack length in that cycle
j=j+2; %increment j by 2 as in the input file two data
%points will be transformed to one
i=i+1;%increment i by 1 as this is the output variable
    end

k=1;
w=1;
[newmax,~]=size(tempdelP);%calculate size of newly formed
%delta P variable
while k<newmax %procedure to skip datapoints
    delP(w)=tempdelP(k); %save temporary variable values to
    %final output variables
    n(w)=tempn(k);
    a(w)=tempa(k);
    k=k+skipvariable; %skip data points here
    w=w+1;
end
delP=delP(delP~=0); %since the variables were initialized
%by zeros, this removes the remaining zeros
n=n(n~=0);
a=a(a~=0);

```

Step 2 : The second step is to reduce the data in such a manner so that there is equal number of data points per increment of crack length. The main reason for doing this is because of the low crack growth in the initial stages, there are higher number of data points that leads to higher scatter in da/dn .

```

function [newa, newn, newdelp]=reducean_part2(a,n,delp,ablock,nr)
%input variables: a:reduced cracklength (ouput from reducean.m)
%n: reduced cycles
%delp:reduced delta P
%ablock: crack increment where reduction procedure is
%carried out
%nr: no of reduced points in each ablock
[maxdata,~]=size(n);
newa=zeros(10000,1);
newn=zeros(10000,1);
newdelp=zeros(10000,1);
aa=zeros(10000,1);
nn=zeros(10000,1);

t=1;%new file traverse variable
i=1;%main file traverse variable
while i<maxdata %Starts main position traverse through the array
    k=i+1;
    for k=i+1:maxdata %starts searching for the next block
        %size hence from i+1 position
        for j=1:k-i+1 %Takes everything from the position of
            %main control i to position of block search k
            %(a total of k-i+1 elements)
            aa(j)=a(j+i-1); %into temporary arrays of aa and nn.
            %The main position is traversed with i and j as i+j-1
            nn(j)=n(j+i-1);

        end
        %quadratic fit procedure starts
        c1=0.5*(nn(1)+nn(k-i+1)); %a constant made of the first
        %and last data points in the 'cycles' array
        c2=0.5*(nn(1)-nn(k-i+1)); %another constant made of the first
        %and last data points in the 'cycles' array
        nn_scaled=(nn-c1)/c2; %a scaled n variable
        sx=0; %sum of linear terms
        sx2=0; %sum of quadratic terms
        sx3=0; % sum of cubic terms
        sx4=0; % sum of quadruple terms
        sy=0; % same as above
        syx=0;
        syx2=0;

```

```

for w=1:k-i+1 %finds sum for the block till now
    sx=sx+nn_scaled(w);
    sx2=sx2+(nn_scaled(w))^2;
    sx3=sx3+(nn_scaled(w))^3;
    sx4=sx4+(nn_scaled(w))^4;
    sy=sy+aa(w);
    syx=syx+aa(w)*nn_scaled(w);
    syx2=syx2+aa(w)*(nn_scaled(w))^2;
end
%least square terms in following lines
term1=(sx2*sx4-sx3^2);
term2=(sx*sx4-sx2*sx3);
term3=(sx*sx3-sx2^2);
denom=7*term1-sx*term2+sx2*term3;
numer2=sy*term1-syx*term2+syx2*term3;
bb(1)=numer2/denom; %first parameter

term4=syx*sx4-syx2*sx3;
term5=sy*sx4-syx2*sx2;
term6=sy*sx3-syx*sx2;
numer3=7*term4-sx*term5+sx2*term6;
bb(2)=numer3/denom; %second parameter

term7=sx2*syx2-sx3*syx;
term8=sx*syx2-sx3*sy;
term9=sx*syx-sx2*sy;
numer4=7*term7-sx*term8+sx2*term9;
bb(3)=numer4/denom; %third parameter
%quadratic fit procedure ends
%quadratic fit with the three parameters and
%scaled n variable
ai_fit=bb(1)+bb(2)*nn_scaled(1)+bb(3)*nn_scaled(1)^2;
%cracklength a according to fit at the begining of the block
af_fit=bb(1)+bb(2)*nn_scaled(k-i+1)+bb(3)*nn_scaled(k-i+1)^2;
%crack length at the end of block
deltaa=af_fit-ai_fit; %crack growth according to fit
if(deltaa<=ablock)%checking if crack growth is under
    %the size mentioned
    continue
%if crack growth is still under size continue with next
%iteration of k (block position, refer to line 10)
else
    break %if crack growth is more then break the iteration
    %and come out of the loop.
end
end %end of block position search

```

```

%at this instance block size has been determined by
%the if statement as it stops at that k where crack growth
%exceeded that block size
blocksize=k-i; % i is still at that position in the main
%traverse and k has moved according to the condition
if blocksize>=nr
    rf=round(blocksize/nr); % for every rf number of
    %data points there will be one data point. nr is the
    %number of data points per block
else
    rf=blocksize;
end
%start of reduction procedure
block_pos=1; %block position set again
b=i; %b is a variable for travelling through
%the block again
while b<k-1 %Travelling through the block. k-1 is
    %the last position of the block in the main file
    suma=0; %sum for average of a
    sumn=0; %sum for average of n
    sumdelp=0;
    no_of_elements=0; %a variable to actual calculate
    %no of elements actually averaged into one element
    for f=0:rf-1 % takes every rf number of elements
        if(block_pos<blocksize) %checks if the local
            %block postion is under the block size
            suma=suma+a(b+f); %then takes into the sum of a.
            %The position of the block elemenets on
            %the main file is i=b+f
            sumn=sumn+n(b+f); %then takes into the sum of n.
            sumdelp=sumdelp+delp(b+f);
            block_pos=block_pos+1; %incrementing block position
            no_of_elements=no_of_elements+1; %caluculates the
            %no of elements actually averaged to one element.
            %In most cases it should be equal to rf
            %but in the end of a block this is not rf.
        else
            break %breaks the loop when block position
            %exceeds blocksize
        end
    end %end of summation
    newa(t)=suma/no_of_elements; %new data point is
    %the average of the rf elements.
    newn(t)=round(sumn/no_of_elements); %same as above
    newdelp(t)=sumdelp/no_of_elements;
    t=t+1; %increment new file position
end

```

```

        b=b+rf; %block position has to skip to the next
        %rf elements
    end %end of block
    i=i+blocksize; %increment main file position to
    %start of next block
end %end of main position
newa=newa(newa~=0); %update newfile to exclude zeros
%as bydefault this file was initialized with zeros.
newn=newn(newn~=0); %same as above.
newdelp=newdelp(newdelp~=0);

```

Step 3 : The third step and the final step is to use the previously reduced data to achieve the final da/dn v/s ΔK data.

```

function [dadn, delK]=dadnmaker(cracklength , n , delP ,W,B)
%input variables: cracklength:
%cracklength after reducean_part2
                %n: cycles after reducean_part2
                %delp: delta P as above
                %W: actual width of the specimen
                %B: thickness of the specimen
%The procedure is taken from ASTM-E647 please refer to it.
%This exact algorithm is present in the standard as well.
[maxdata,~]=size(n);

dadn=zeros(maxdata,1);
delK=zeros(maxdata,1);
bb=zeros(3,1);
aa=zeros(10,1);
nn=zeros(10,1);
i=1;
j=1;
k=0;

for i=1:maxdata-6
    l=0;
    k=k+1;
    k1=k+6;
    for lindex=k:k1
        l=l+1;
        aa(l)=cracklength(lindex);
        nn(l)=n(lindex);
    end
    c1=0.5*(nn(1)+nn(7));
    c2=0.5*(nn(7)-nn(1));
    nn_scaled=(nn-c1)/c2;

```

```

sx=0;
sx2=0;
sx3=0;
sx4=0;
sy=0;
syx=0;
syx2=0;
for w=1:7
    sx=sx+nn_scaled(w);
    sx2=sx2+(nn_scaled(w))^2;
    sx3=sx3+(nn_scaled(w))^3;
    sx4=sx4+(nn_scaled(w))^4;
    sy=sy+aa(w);
    syx=syx+aa(w)*nn_scaled(w);
    syx2=syx2+aa(w)*(nn_scaled(w))^2;
end
term1=(sx2*sx4-sx3^2);
term2=(sx*sx4-sx2*sx3);
term3=(sx*sx3-sx2^2);
denom=7*term1-sx*term2+sx2*term3;
numer2=sy*term1-syx*term2+syx2*term3;
bb(1)=numer2/denom;

term4=syx*sx4-syx2*sx3;
term5=sy*sx4-syx2*sx2;
term6=sy*sx3-syx*sx2;
numer3=7*term4-sx*term5+sx2*term6;
bb(2)=numer3/denom;

term7=sx2*syx2-sx3*syx;
term8=sx*syx2-sx3*sy;
term9=sx*syx-sx2*sy;
numer4=7*term7-sx*term8+sx2*term9;
bb(3)=numer4/denom;
dadn(i)=bb(2)/c2+2*bb(3)*nn_scaled(4)/c2;
aa_fit=bb(1)+bb(2)*nn_scaled(4)+bb(3)*nn_scaled(4)^2;
crack_ratio=aa_fit/W;
f_aW = geometric(crack_ratio);
delK(i)=delP(i)*48*f_aW/(B*W^1.5*sqrt(1000));
end
dadn=dadn(dadn~=0);
delK=delK(delK~=0);

```

6.3. Residual stress measurements (x-ray diffraction)

Since discussions involving AM parts IN718 put a lot of emphasis on the process induced residual stresses, an attempt to evaluate these values in *AP* and *HIPHT* (by Sahu et. al. [12]) and *HT* (in this study) specimens was undertaken. However, the measurement of residual stresses using xrd requires a highly reliable and consistent sample preparation procedure for accurate results. Another point to note here is that even after accurate measurement, the values obtained will be highly location specific and cannot be generalized for the bulk material. This is because the specimens are built layer by layer using SLM leading to a heterogeneous stress build up due to inconsistent reheating of the melted layers. The residual stresses thus generated and their nature are highly dependant on the specimen geometry which makes it difficult to compare with other studies from the literature. The residual stress measurements for UG and G specimens are provided in Table 6.1 and 6.2 respectively. The negative values indicate residual stresses of compressive nature. These tables help in asserting the fact that there is a large variation between the measured values at same positions for same specimens. Studies involving a higher degree of focus on multiple trials and positions of stress measurements can help shed more light on the trends in different specimens and conditions.

Table 6.1: Residual stress measurements at on the XY planes of the ungraded specimens.

Processing Condition	Laser Power / Grains	Specimen	Stress along BD (MPa)		Stress perpendicular to BD (MPa)	
			Measurement #		Measurement #	
			1	2	1	2
AP	950 W / Coarse	BD ⊥ CD	-100 ± 23	Measurement error	-151 ± 30	Measurement error
	950 W / Coarse	BD ∥ CD	-368 ± 98	-775 ± 114	-259 ± 60	-680 ± 74
	250 W / Fine	-	-480 ± 66	-483 ± 74	-377 ± 44	-427 ± 26
HT	950 W / Coarse	BD ⊥ CD	-175 ± 71	-428 ± 98	-378 ± 0	-687 ± 252
	950 W / Coarse	BD ∥ CD	Measurement error	-746 ± 137	-327 ± 168	-793 ± 137
	250 W / Fine	-	-43 ± 29	-311 ± 38	-179 ± 20	-413 ± 29
HIPHT	950 W / Coarse	BD ⊥ CD	-239 ± 72	-	-355 ± 66	-
	950 W / Coarse	BD ∥ CD	-552 ± 170	-	-503 ± 67	-
	250 W / Fine	-	-186 ± 36	-	-371 ± 49	-

Table 6.2: Residual stress measurements on the XY planes of graded specimens.

Processing Condition	Specimen	Laser Power / Grains	Stress along BD (MPa)		Stress perpendicular to BD (MPa)	
			Measurement #		Measurement #	
			1	2	1	2
AP	BD ⊥ CD	950 W / Coarse	-381 ± 68	-	-353 ± 90	-
	BD ⊥ CD	250 W / Fine	-304 ± 11	-	-234 ± 27	-
	BD ∥ CD	950 W / Coarse	-125 ± 28	-	-297 ± 13	-
	BD ∥ CD	250 W / Fine	-193 ± 45	-	-146 ± 38	-
HT	BD ⊥ CD	950 W / Coarse	-783 ± 35	-462 ± 77	-282 ± 3	-409 ± 13
	BD ⊥ CD	250 W / Fine	-528 ± 34	-717 ± 31	-152 ± 32	-370 ± 22
	BD ∥ CD	950 W / Coarse	-438 ± 103	-324 ± 46	-411 ± 46	-445 ± 27
	BD ∥ CD	250 W / Fine	-234 ± 10	-409 ± 56	-381 ± 26	-358 ± 26
HIPHT	BD ⊥ CD	950 W / Coarse	-596 ± 32	-	-418 ± 56	-
	BD ⊥ CD	250 W / Fine	-621 ± 127	-	-397 ± 92	-
	BD ∥ CD	950 W / Coarse	-438	-	-382 ± 195	-
	BD ∥ CD	250 W / Fine	-299	-	-479 ± 24	-

Bibliography

- [1] E. Hosseini and V. A. Popovich. "A review of mechanical properties of additively manufactured Inconel 718". In: *Additive Manufacturing* 30 (2019).
- [2] J. B. Roca et al. "Policy needed for additive manufacturing". In: *Nature Materials* 15.8 (2016), pp. 815–818.
- [3] D. Deng. "Additively Manufactured Inconel 718 : Microstructures and Mechanical Properties". Doctoral Thesis. Linköping University, Sweden, 2018.
- [4] A. Lingenfelter. "Welding of Inconel Alloy 718: A Historical Overview". In: *Superalloy 718 - Metallurgy and Applications* (1989), pp. 673–683.
- [5] A. Mostafa et al. "Structure, texture and phases in 3D printed IN718 alloy subjected to homogenization and HIP treatments". In: *Metals* 7.6 (2017), pp. 1–23.
- [6] C. Kumara. "Microstructure Modelling of Additive Manufacturing of Alloy 718". PhD Thesis. University West, 2018.
- [7] G. H. Cao et al. "Investigations of γ' , γ " and δ precipitates in heat-treated Inconel 718 alloy fabricated by selective laser melting". In: *Materials Characterization* 136. January (2018), pp. 398–406.
- [8] D. Sindhura, M. V. Sravya, and G. V.S. Murthy. "Comprehensive Microstructural Evaluation of Precipitation in Inconel 718". In: *Metallography, Microstructure, and Analysis* 8.2 (2019), pp. 233–240.
- [9] T. Antonsson and H. Fredriksson. "The effect of cooling rate on the solidification of INCONEL 718". In: *Metallurgical and Materials Transactions B* 36.1 (2005), pp. 85–96.
- [10] M.G. Burke and M.K. Miller. "Precipitation in Alloy 718: A combined AEM and APFIM Investigation". In: (2012), pp. 337–350.
- [11] L. L. Parimi et al. "Microstructural and texture development in direct laser fabricated IN718". In: *Materials Characterization* 89 (2014), pp. 102–111.
- [12] S. Sahu. "Fatigue Behaviour of functionally graded Inconel 718 manufactured by selective laser melting". Master's Thesis. Delft University of Technology, 2020. URL: <http://resolver.tudelft.nl/uuid:edf44c06-a295-4f63-9d2c-181a128cc0d8>.
- [13] A. Palawat. "Effect of Post-Processing Treatments on the Microstructure and Creep Behavior of Functionally Graded Inconel 718 Manufactured by Selective Laser Melting". Master's Thesis. Delft University of Technology, 2019.
- [14] R. Kelkar et al. "Alloy 718: Laser Powder Bed Additive Manufacturing for Turbine Applications". In: *Proceedings of the 9th International Symposium on Superalloy 718 & Derivatives: Energy, Aerospace, and Industrial Applications*. Springer International Publishing, 2018, pp. 53–67.

- [15] H. Qi, M. Azer, and A. Ritter. "Studies of Standard Heat Treatment Effects on Microstructure and Mechanical Properties of Laser Net Shape Manufactured". In: *METALLURGICAL AND MATERIALS TRANSACTIONS A* 40A (2009), pp. 2410–2422.
- [16] K. Moussaoui et al. "Effects of Selective Laser Melting additive manufacturing parameters of Inconel 718 on porosity, microstructure and mechanical properties". In: *Materials Science and Engineering A* 735.April (2018), pp. 182–190.
- [17] M. Seif et al. "Effects of Post-processing on Microstructure and Mechanical Properties of SLM-Processed IN-718". In: *Proceedings of the 9th International Symposium on Superalloy 718 & Derivatives: Energy, Aerospace, and Industrial Applications*. 2018, pp. 515–526.
- [18] L. Jiao et al. "Femtosecond Laser Produced Hydrophobic Hierarchical Structures on Additive Manufacturing Parts". In: *Nanomaterials* 8 (Aug. 2018), p. 601.
- [19] K. N. Amato et al. "Microstructures and mechanical behavior of Inconel 718 fabricated by selective laser melting". In: *Acta Materialia* 60.5 (2012), pp. 2229–2239.
- [20] J. Strößner, M. Terock, and U. Glatzel. "Mechanical and Microstructural Investigation of Nickel-Based Superalloy IN718 Manufactured by Selective Laser Melting (SLM)". In: *Advanced Engineering Materials* 17.8 (2015), pp. 1099–1105.
- [21] C. Y. Yap et al. "Review of selective laser melting: Materials and applications". In: *Applied Physics Reviews* 2.4 (2015).
- [22] X. Wang, X. Gong, and K. Chou. "Review on powder-bed laser additive manufacturing of Inconel 718 parts". In: *Proceedings of the Institution of Mechanical Engineers, Part B: Journal of Engineering Manufacture* 231.11 (2017), pp. 1890–1903.
- [23] M. M. Kirka et al. "Effect of anisotropy and texture on the low cycle fatigue behavior of Inconel 718 processed via electron beam melting". In: *International Journal of Fatigue* 105 (2017), pp. 235–243.
- [24] M. E. Aydinöz et al. "On the microstructural and mechanical properties of post-treated additively manufactured Inconel 718 superalloy under quasi-static and cyclic loading". In: *Materials Science & Engineering A* 669 (2016), pp. 246–258.
- [25] W. M. Tucho et al. "Microstructure and hardness studies of Inconel 718 manufactured by selective laser melting before and after solution heat treatment". In: *Materials Science and Engineering A* 689.February (2017), pp. 220–232.
- [26] F. Brenne et al. "Microstructural design of Ni-base alloys for high-temperature applications: impact of heat treatment on microstructure and mechanical properties after selective laser melting". In: *Progress in Additive Manufacturing* 1.3-4 (2016), pp. 141–151.

- [27] W. Tillmann et al. "Hot isostatic pressing of IN718 components manufactured by selective laser melting". In: *Additive Manufacturing* 13 (2017), pp. 93–102.
- [28] T. Trosch et al. "Microstructure and mechanical properties of selective laser melted Inconel 718 compared to forging and casting". In: *Materials Letters* 164 (2016), pp. 428–431.
- [29] D. Zhang et al. "Materials Science & Engineering A Effect of standard heat treatment on the microstructure and mechanical properties of selective laser melting manufactured Inconel". In: *Materials Science & Engineering A* 644 (2015), pp. 32–40.
- [30] V. A. Popovich et al. "Impact of heat treatment on mechanical behaviour of Inconel 718 processed with tailored microstructure by selective laser melting". In: *Materials and Design* 131.May (2017), pp. 12–22.
- [31] V. A. Popovich et al. "Functionally graded Inconel 718 processed by additive manufacturing : Crystallographic texture , anisotropy of microstructure and mechanical properties". In: *Materials and Design* 114 (2017), pp. 441–449.
- [32] V. A. Popovich et al. "Tailoring the Properties in Functionally Graded Alloy Inconel 718 Using Additive Technologies". In: *Metal Science and Heat Treatment* 60.11-12 (2019), pp. 701–709.
- [33] D. H. Smith et al. "Microstructure and mechanical behavior of direct metal laser sintered Inconel alloy 718". In: *Materials Characterization* 113 (2016), pp. 1–9.
- [34] J. Schneider. "Comparison of Microstructural Response to Heat Treatment of Inconel 718 Prepared by Three Different Metal Additive Manufacturing Processes". In: *Joining of Materials* 72.3 (2020), pp. 1085–1091.
- [35] C. Körner et al. "Tailoring the grain structure of IN718 during selective electron beam melting". In: *MATEC Web of Conferences* 14.November 2015 (2014).
- [36] M. Ni et al. "Anisotropic tensile behavior of in situ precipitation strengthened Inconel 718 fabricated by additive manufacturing". In: *Materials Science and Engineering: A* 701 (2017), pp. 344–351.
- [37] R. Singh et al. "A Review on Functionally Gradient Materials (FGMs) and Their Applications". In: *IOP Conference Series: Materials Science and Engineering* 229.1 (2017).
- [38] M. Sato, A. Inoue, and H. Shima. "Bamboo-inspired optimal design for functionally graded hollow cylinders". In: *PLOS ONE* 12 (May 2017), pp. 1–14.
- [39] Po-Yu Chen et al. "Structure and mechanical properties of crab exoskeletons". In: *Acta Biomaterialia* 4.3 (2008), pp. 587–596.
- [40] I. M. El-Galy, B. I. Saleh, and M. H. Ahmed. "Functionally graded materials classifications and development trends from industrial point of view". In: *SN Applied Sciences* 1.11 (2019), pp. 1–23.
- [41] D. Mahmoud and M. Elbestawi. "Lattice Structures and Functionally Graded Materials Applications in Additive Manufacturing of Orthopedic Implants: A Review". In: *Journal of Manufacturing and Materials Processing* 1.13 (2017).

- [42] A. Piglione et al. "Printability and microstructure of the CoCrFeMnNi high-entropy alloy fabricated by laser powder bed fusion". In: *Materials Letters* 224.April (2018), pp. 22–25.
- [43] T. Niendorf et al. "Highly Anisotropic Steel Processed by Selective Laser Melting". In: *METALLURGICAL AND MATERIALS TRANSACTIONS B* 44B (2013), pp. 794–796.
- [44] J. Rösler, M. Bäker, and H. Harders. "Fatigue". In: *Mechanical Behaviour of Engineering Materials: Metals, Ceramics, Polymers, and Composites*. Berlin, Heidelberg: Springer Berlin Heidelberg, 2007, pp. 333–382.
- [45] B. M. Albiston. "Influence of Microstructure on the Propagation of Fatigue Cracks in Inconel 617". Master's Thesis. Boise State University, 2013.
- [46] A. F. Lignelli. *Fatigue Crack Growth : Mechanics, Behavior and Prediction*. New York, UNITED STATES: Nova Science Publishers, Incorporated, 2009.
- [47] P. Paris and F. Erdogan. "A Critical Analysis of Crack Propagation Laws". In: *Journal of Basic Engineering* 85.4 (1963), pp. 528–533.
- [48] R. Wanhill, S. Barter, and L. Molent. *Fatigue Crack Growth Failure and Lifing Analyses for Metallic Aircraft Structures and Components*. SpringerBriefs in Applied Sciences and Technology, 2018.
- [49] J. R. Poulin, V. Brailovski, and P. Terriault. "Long fatigue crack propagation behavior of Inconel 625 processed by laser powder bed fusion: Influence of build orientation and post-processing conditions". In: *International Journal of Fatigue* 116.April (2018), pp. 634–647.
- [50] C. Pei et al. "Assessment of mechanical properties and fatigue performance of a selective laser melted nickel-base superalloy Inconel 718". In: *Materials Science and Engineering A* 759.May (2019), pp. 278–287.
- [51] E. Amsterdam. *Evaluation of the microstructure and mechanical properties of laser additive manufactured gas turbine alloys Ti-6Al-4V and*. Tech. rep. Amsterdam: National Aerospace Laboratory (NLR), 2010, pp. 1–25.
- [52] A. S. Johnson et al. "Microstructure, Fatigue Behavior, and Failure Mechanisms of Direct Laser-Deposited Inconel 718". In: *Joining of Materials* 69.3 (2017), pp. 597–603.
- [53] P. F. Kelley, A. Saigal, and A. Carter. "Fatigue behaviour of direct metal laser sintered Inconel 718". In: *International Journal of Precision Technology* 6.3/4 (2016).
- [54] R. Konečná et al. "Fatigue crack growth behavior of Inconel 718 produced by selective laser melting". In: *Frattura ed Integrità Strutturale* 35 (2016), pp. 31–40.
- [55] H. Wan et al. "Enhancing Fatigue Strength of Selective Laser Melting-Fabricated Inconel 718 by Tailoring Heat Treatment Route". In: *Advanced Engineering Materials* 20.1800307 (2018), pp. 1–6.

- [56] M. Clavel and A. Pineau. "Fatigue behaviour of two nickel-base alloys I: Experimental results on low cycle fatigue, fatigue crack propagation and substructures". In: *Materials Science and Engineering* 55.2 (1982), pp. 157–171.
- [57] X. Hu et al. "On the fatigue crack growth behaviour of selective laser melting fabricated Inconel 625: Effects of build orientation and stress ratio". In: *Fatigue and Fracture of Engineering Materials and Structures* 43.4 (2020), pp. 771–787.
- [58] S. Kim et al. "Room and elevated temperature fatigue crack propagation behavior of Inconel 718 alloy fabricated by laser powder bed fusion". In: *International Journal of Fatigue* 140.March (2020).
- [59] ASTM E399. "Metallic Material Fracture Toughness Testing". In: *American Society for Testing and Materials* (2014).
- [60] ASTM E647–13. "Standard Test Method for Measurement of Fatigue Crack Growth Rates". In: *American Society for Testing and Materials* (2014), pp. 1–50.
- [61] R. Seede, A. Mostafa, and M. Medraj. "Microstructural and Microhardness Evolution from Homogenization and Hot Isostatic Pressing on Selective Laser Melted Inconel 718 : Structure , Texture , and Phases". In: *Journal of Manufacturing and Materials Processing*. 2.30 (2018).
- [62] E. M. Fayed et al. "Influence of homogenization and solution treatments time on the microstructure and hardness of Inconel 718 fabricated by laser powder bed fusion process". In: *Materials* 13.11 (2020).
- [63] U. Krupp. "Crack Propagation: Microstructural Aspects". In: *Fatigue Crack Propagation in Metals and Alloys*. John Wiley Sons, Ltd, 2007. Chap. 6, pp. 135–206.
- [64] R. Jiang et al. "Effects of microstructures on fatigue crack initiation and short crack propagation at room temperature in an advanced disc superalloy". In: *Materials Science & Engineering A* 641 (2015), pp. 148–159.
- [65] C. Blochwitz, S. Jacob, and W. Tirschler. "Grain orientation effects on the growth of short fatigue cracks in austenitic stainless steel". In: *Materials Science and Engineering A* 496.1-2 (2008), pp. 59–66.
- [66] Y. Suk et al. "Identifying strain localization and dislocation processes in fatigued Inconel 718 manufactured from selective laser melting". In: *Materials Science & Engineering A* 724.February (2018), pp. 444–451.
- [67] Y. Zhang, X. An Hu, and Y. Jiang. "Study on the Microstructure and Fatigue Behavior of a Laser-Welded Ni-Based Alloy Manufactured by Selective Laser Melting Method". In: *Journal of Materials Engineering and Performance* 29.5 (2020), pp. 2957–2968.
- [68] H. Andersson and C. Persson. "In-situ SEM study of fatigue crack growth behaviour in IN718". In: *International Journal of Fatigue* 26.3 (2004), pp. 211–219.